Electron Impact Ionization Study of High Z elements

by

Hitesh V. Rahangdale

Enrollment No.: PHYS05201004011

Saha Institute of Nuclear Physics
Kolkata

A thesis submitted to the
Board of Studies in Physical Science Discipline
In partial fulfillment of requirements
For the Degree of

DOCTOR OF PHILOSOPHY

of

HOMI BHABHA NATIONAL INSTITUTE

July, 2016

Homi Bhabha National Institute

Recommendations of the Viva Voce Committee

As members of the Viva Voce Committee, we certify that we have read the dissertation prepared by Hitesh V. Rahangdale entitled "Electron impact ionization study of high Z elements" and recommend that it may be accepted as fulfilling the thesis requirement for the award of Degree of Doctor of Philosophy.

Supratik Mukhopadhyay — **Date :** 15/11/16

Chairman : **Prof. Supratik Mukhopadhyay**, SINP

Satyajit Saha — **Date :** 15/11/16

Guide & Convener : **Prof. Satyajit Saha**, SINP

Amlan Ray — **Date :** 15/11/16

Member : **Prof. Amlan Ray**, VECC

Debashis Mitra — **Date :** 15/11/16

Member : **Prof. Debashis Mitra**, Kalyani University

Sankar De — **Date :** 15/11/16

Member : **Prof. Sankar De**, SINP

Date : 15/11/16

External Examiner: **Prof. Lokesh C. Tribedi**, TIFR

Final approval and acceptance of this thesis is contingent upon the candidate's submission of the final copies of the thesis to HBNI.

I hereby certify that I have read this thesis prepared under my direction and recommend that it may be accepted as fulfilling the thesis requirement.

Date : 15/11/2016
KOLKATA

Satyajit Saha
(Guide)

STATEMENT BY AUTHOR

This dissertation has been submitted in partial fulfillment of requirements for an advanced degree at Homi Bhabha National Institute (HBNI) and is deposited in the Library to be made available to borrowers under rules of the HBNI.

Brief quotations from this dissertation are allowable without special permission, provided that accurate acknowledgment of source is made. Requests for permission for extended quotation from or reproduction of this manuscript in whole or in part may be granted by the Competent Authority of HBNI when in his or her judgment the proposed use of the material is in the interests of scholarship. In all other instances, however, permission must be obtained from the author.

HITESH V. RAHANGDALE

DECLARATION

I, hereby declare that the investigation presented in the thesis has been carried out by me. The work is original and has not been submitted earlier as a whole or in part for a degree / diploma at this or any other Institution / University.

HITESH V. RAHANGDALE

List of Publications arising from the thesis

Journal

1. **"Determination of subshell-resolved L-shell-ionization cross sections of gold induced by 15-40 keV electrons"**
   Rahangdale et. al,
   Phys. Rev. A **89**, 052708(2014).

2. **"Spectroscopic investigations of L-shell ionization in heavy elements by electron impact."**
   Rahangdale et. al,
   J. Quant. Spectrosc. Radiat. Transfer **174**, 79-87 (2016).

Conference

1. **"Subshell resolved inner shell ionization cross-sections of High Z elements by electron impact"**
   Rahangdale et. al,
   J. Phys. Conf. Series **635**, 052001 (2015).

2. **"Subshell Resolved L-shell ionization studies of high- Z elements by electron impact"**
   Rahangdale et. al,
   (PoS 4^{th} CDAMOP AT-19) Current Developments in Atomic, Molecular, Optical Physics, New Delhi(India), March 2015 **(Oral)**.

3. **"Subshell Resolved L-shell ionization studies of Bi and U induced by 16-45 keV electrons"**
   Rahangdale et. al,
   (PoS 4^{th} CDAMOP P-71) Current Developments in Atomic, Molecular, Optical Physics, New Delhi(India), March 2015.

HITESH V. RAHANGDALE

To
My Family

ACKNOWLEDGMENTS

First of all, I thank Saha Institute of Nuclear Physics, for providing me with an opportunity to pursue research and Department of Atomic Energy (DAE), Govt. of INDIA for giving me financial support as a research fellowship.

I sincerely thank my thesis advisor, Prof. Satyajit Saha, for being an advisor with unending patience, insightful thoughts, and encouragements (even for craziest ideas). I thank him for being easily accessible to all his students despite his busy schedule, which has made my research life very smooth. I am grateful that he introduced me to the facets of conducting experimental research and has shown me by his example, how good an experimental physicist could be.

This thesis would not have been possible without the initial guidance of Prof. Debasis Mitra and his expertise in the field of atomic physics. I would like to extend my gratitude to Monali Bhabhi, Debashis Da's wife, for being a very considerate and caring landlord.

I have had the good fortune to have the assistance of many fine colleagues during my time here at SINP. Most important to mention here is my lab buddy Mr. Pradipta K Das. I thank Pradipta da for sharing his experimental expertise and experiences with me. Many thanks to Prof. Chandi Charan Dey, Prof. Maitreyee Saha Sarkar, Prof. Supratik Mukhopadhyay, Prof. Sandip Sarkar, Prof. Sankar De, and Arindam Sikdar for their timely help and illuminating discussions. Thanks also go to Dr Jisnu Basu, Mr. Sudipta Burman, Mr. Partha Karmakar and other members of SINP machine shop for their guidance and assistance in various developmental and fabrication work during the thesis.

Thank you, Amol and Sachin for your faith in me as a researcher. Sourav,

Bankim, Avik and Deb you are such great friends. My experience at SINP would not even come close to being the same without you! Rajani, you helped me to keep a healthy perspective on life's priorities and a cheery outlook, thanks a lot. I also thank my friends from Post-MSc batch of 2010 for discussions on various topics in physics and beyond.

Lastly, nobody has been more important to me in pursuit of this thesis than the members of my family. My parents are the source of my inspirations and everything that I have accomplished is due to their hard work and unconditional blessings. Thanks Ritesh for being a very responsible brother. Finally, I wish to thank my love, Pinku, for bringing me happiness, love, and care. I cannot thank you enough for your support and sacrifice over last three years to make this endeavor a success.

HITESH V. RAHANGDALE

Contents

SYNOPSIS

When an energetic electron passes through a material, it interacts with the material atoms via many interactions viz., elastic or inelastic collision, bremsstrahlung radiation emission etc. If the energy of the electron is more than the atomic binding energy of atoms, ionization due to the emission of inner shell electron can take place. This ionization is followed by the relaxation of the atom which can happen by X-ray or Auger electron emission. Moreover, if the vacancy is created or propagated to L or other higher sub-shell(not outermost sub-shell), atomic relaxation can occur via Coster-Kronig transitions between the sub-shells emitting electrons. These secondary radiations are the basis of many material characterization techniques making the electron impact ionization data as essential input for many applications like electron probe microanalysis (EPMA), electron energy loss spectroscopy (EELS), Auger electron spectroscopy (AES) etc. As it is practically impossible to have the experimental electron impact ionization cross section data at every electron impact energy, many theories and models are developed to obtain these cross sections to be used in such applications. The development of such models are going on since many decades and due to the effort of many research groups, several models based on PWBA theory have been proposed, which predict inner shell ionization cross sections for K-shell ionization very accurately. Among these models, the most used is the Binary Encounter Bethe model[1]. Recently there has been more elaborate studies using distorted wave Born approximation theory(DWBA) which is shown to predict inner shell ionization for L and M subshell with reasonable accuracy[2]. Needless to say that there exists a need to compare the predictions of these models against experimental results, and in the current thesis work, I have tried to do the same by measuring L-subshell resolved ionization cross sections for a few high Z elements. The results are tested against the PWBA based Modified Relativistic Binary Encounter

Bethe (MRBEB) model[3] and also the DWBA based results[4]

Inner shell ionization cross sections can be determined by measuring the intensity of characteristic X-rays emitted due to bombarding of the mono-energetic electron beam on self-supported thin film target of the considered element. It should be noted, however, that not all the vacancy in the inner shell is filled through accompanying X-ray transitions. The process is complemented with Auger electron emission, which is a radiationless process resulting in the emission of electrons from the same atom. The probability that a vacancy created in one of the atomic shells is filled through a radiative transition is called the fluorescence yield. Due to the involvement of factors like fluorescence yield and projectile electron scattering while traveling through the medium, determination of absolute values of the cross section becomes difficult. In the case of L and M shells, adding to these difficulties is the fact that vacancies in a given sub-shell can be produced not only by electron impact but also by non-radiative Coster- Kronig transitions between the sub-shells. As a consequence, the intensity of a given x-ray line depends on the ionization cross sections of all the sub-shells, weighted by the corresponding Coster- Kronig coefficients. Therefore, in order to extract the ionization cross sections from X-ray emission yields, one has to use these relaxation parameters i.e, Coster-Kronig coefficients, Fluorescence yields etc from the literature. These relaxation parameters are generally affected by large uncertainties, which would propagate to the derived ionization cross sections. In this thesis work, dependence of the relevant cross section results on the relaxation parameter is also studied.

The present work involves study of the electron impact ionization for heavy elements. To carry out this study, an experimental setup is developed in which, electron-atom collision experiments can be performed with the thin film targets and X-rays and electrons can be detected. To differentiate the effects of the material properties of thin film and to obtain the efficiency of the detector using bremsstrahlung

radiation, the electron transport simulation of the electron inside the target is done. Also, investigations are done to understand the effects of relaxation parameters in extracting the ionization cross sections from production cross sections.

The electron-atom collision experimental setup was designed and constructed during this thesis work. The setup consists of an electron gun(Energy range $0 - 50$ keV, Max. beam current:$100\,\mu$A), a target holder inserted through the Wilson seal, a Faraday cup and X-ray detector, all arranged in a horizontal central plane of a cylindrical vacuum chamber. The detector was placed at 125^0 angle with respect to the beam direction. The vacuum inside chamber was bought down to $\sim 10^{-7}$ mbar using a turbo pump, backed by a rotary vane pump. The electron beam can be aligned by the magnetic steerer made to steer such beam and placed outside the chamber.

The main problem faced when performing beam-foil experiments by electron impact is to make the self- supporting thin film targets and to measure their thicknesses accurately. The targets for the experiment were made by two different techniques i.e, (i) by electron beam vapor deposition (EBVD) method and (ii) by electro- deposition (ED) method. The targets were either self- supporting (Au) or they were backed by (i)Carbon (Pb and Bi) thin film or (ii) Aluminum (Th and U) foil. The thickness of the targets was monitored while deposition by quartz crystal monitor for deposition by EBVD and by the current through the electro-deposition cell for deposition by ED technique. Finally, the thicknesses of the thin film targets were measured with good precision using a laboratory made alpha energy loss spectroscopy set-up. The alpha energy loss spectrometer consists of three line alpha source, target holder and solid state alpha particle detector arranged in a straight line. When the alpha particle passes through the thin film, it losses fraction of its energy(ΔE). By measuring this energy loss and using the specific energy loss ($\frac{dE}{dx}$) data, the thickness of the thin film is obtained. The value of $\frac{dE}{dx}$, also known as stopping power, is taken

from the program SRIM [5]. Using this setup, the thin film target thicknesses were measured with up to 10% accuracy.

The other important quantities which are needed to obtain the absolute cross section values are the number of incident electrons on the target and the detector efficiency. To know incident electron flux, the target ladder was electronically isolated from the chamber and current was measured on it and on the Faraday cup. The Faraday cup was long, with different opening diameters for different experiments based on where it is placed. The base of Faraday cup was made conical to ensure trapping of secondary electrons in the Faraday cup itself. The collection efficiency was checked by biasing the Faraday cup at +105 V above ground potential at which the chamber was kept. The collection current was at the most 3% higher because of bias voltage. The collection efficiency was also checked by applying a negative potential to a copper ring mounted at the face of the Faraday cup. No significant difference was observed even after biasing the ring by −1000 V. With the target in the beam position, the total beam current is the sum of current measured at the Faraday cup and that at the target ladder. This total beam current was less than the beam current collected by Faraday cup when the target was removed from the beam position. This deficiency in current was because of backscattering of the electrons from the target. One can use the backscattering factor to get the actual number of incident electrons, but this data is not always available for the required thickness, and hence one has to rely on estimated values, which may vary by 10-20 % [6]. To avoid the backscattering factor correction, the total number of electrons during a given time was measured using the charges collected at the Faraday cup with and without the target. This ratio was measured throughout the experiment at regular interval and found that the variation was $\lesssim 1\%$. To get the actual number of electrons in the beam, the total integrated charge during the data collection period was scaled by this ratio.

The characteristic X-rays emitted from the target were detected by cryogen

free solid-state X-ray detectors used as energy dispersive spectrometer. For early experiments, Si-PIN diode detector (Model No. XR-100CR from Amptek Inc, USA) was used but later it was replaced by higher resolution Silicon drift detector(Model No. XR-100SDD from Amptek Inc, USA). To avoid attenuation of X-rays below 10 keV, the detector, built-in preamplifier and the Peltier cooler were mounted inside the vacuum chamber on an Aluminum block. The detector was mounted such that it viewed the target center sitting at 125° angle with respect to the upstream electron beam. The active region of the detector was shielded from the scattered X-rays by a graded collimator of cylindrical shape and having an axial opening hole of 2 mm. With the distance between target center and the detector collimator entrance being 77 mm, the detector subtended a solid angle of $\sim 5.3 \times 10^{-4}$ steradian at the target center. The collimator had four different layers made of elements with decreasing atomic number (Z) from the outer surface to the inner one. The outer shell is made of Lead, followed by shells of Copper, Aluminum and Graphite. The collimator efficiently shielded the active element of the detector as observed from the overall reduction of the spectral background. The front surface of the collimator was covered with a mylar foil (100 μm thick) to cut off high M X-rays flux laying below ~ 5 keV for the elements studied. The mylar film significantly reduced the dead time loss of the data acquisition system and also reduced the low energy X-ray background. From the available data on X-ray attenuation in Mylar [7], the chosen absorber cut $\sim 83.8\%$ of X-rays below 3 keV and $\sim 99.8\%$ of X-rays below 2 keV. The preamplifier output from the X-ray detector was fed to the input of a shaping amplifier (25 μs shaping time). The amplifier output pulse was analyzed by a multichannel analyzer with 8k analog to digital converter (ADC). For SDD detector, the shaping amplifier and the MCA were integrated into a digital signal processing(DSP) unit.

The total efficiency (ϵ) of the detector is an important parameter needed for the experiment. It was determined by three different methods. Characteristic X-ray

lines from a calibrated ^{241}Am source (1 μCi) were used to determine the efficiency. In another method, copper K X-ray yields due to electron beam bombardment on a copper target of pre- determined thickness and purity, was used[4]. Limitation of the above two methods was that the efficiency could be obtained over the low electron energy range, i.e, 8-17 keV. To obtain the efficiency for the higher energy range, the bremsstrahlung radiation from thick Carbon and Aluminum targets was used. The X-ray energy spectra were compared with the spectra obtained from a Monte Carlo simulation. The efficiency as a function of energy was obtained from these results. The details of the simulation procedure are described in the next section.

While traveling through the material, electrons can interact with the atoms via different processes like elastic collision, bremsstrahlung, inelastic collision etc. Though elastic collision conserves the kinetic energy of a projectile particle, it alters the path of the particle. If the particles enter the target medium along the normal, they are likely to get scattered at oblique angles which would result in increase of path lengths traversed inside the medium. In the case of a target backed by Aluminum, there is a finite probability of electrons being backscattered into the target. This increase in the path length increases the probability of inner shell ionization within the target medium. In addition, the projectile electron can shed its energy by emitting bremsstrahlung radiation, thereby causing a reduction in the effective incident beam energy. This generally leads to an apparent reduction of the measured value of inner shell ionization cross section at the incident beam energy. In order to take these cumulative effects into account, the electron and photon transport simulation inside the thin film target is done. The simulation is also used to ensure occurrence of only single ionization event for the chosen thickness of the targets, and also to obtain the efficiency of the detector using the bremsstrahlung spectra of thick carbon and Aluminum targets. Because of the absence of the characteristic peak in the region of interest, C and Al are chosen as the targets to obtain efficiency of the detector.

The simulations are carried out with two general purpose Monte Carlo simulation packages i.e, GEANT4 [8] and PENELOPE [9]. Both GEANT4 and PENELOPE packages are designed such that they can easily incorporate sophisticated interaction models and using Monte Carlo methods, they can conveniently include arbitrary geometry into the calculation. As in any general Monte Carlo code, both GEANT4 and PENELOPE simulate each particle track one by one. Each track is divided into many smaller steps over the entire interaction volume. The length of step (step length) is decided by the interaction models considered for the simulation. More probable the interaction is, the smaller will be the step length and vice versa. When more than one physical processes are involved, smallest step length is used based on most probable interaction. Each simulation track begins with the generation of the projectile particle with initial Energy(E), position($\vec{X}$) and momentum ($\vec{P}$). The particle is then moved forward according to the initial momentum. While moving forward, as soon as the particle comes across the boundary of the interaction medium, it is stopped and its position is modified ($\vec{X'}$). The interaction is then selected according to random number sampling and the variables of the projectile particles are modified accordingly (E',$\vec{X'}$,$\vec{P'}$). The projectile is moved forward in the interaction volume by the unit step length according to the modified parameters. At the end of the step, the similar process of choosing the interaction and modifying the parameters is repeated and the particle is moved forward with the modified parameters. This process of moving the particle forward is continued till the end of interacting media is met or projectile particle is absorbed in the medium. The projectile particle is absorbed in the medium when its kinetic energy becomes less than a certain cut off value.

The need of using two simulation packages is due to the different physics models these two packages provide for a particular interaction. In this thesis work, the simulation is performed to study the inner shell ionization in high Z elements by

electron impact of energy range $0 - 50$ keV. Therefor the main physics process we are interested in is the inelastic collision causing ionization in L-shell. In this energy range, there are mainly two physics lists used by GEANT4 to describe inner shell ionization namely Livermore physics list and PENELOPE physics list. Physics list is the main physics part of GEANT4 simulation which contains an instruction to use physics model for the physical process to be considered in the simulation. To describe inner shell ionization, Livermore physics list uses the Livermore evaluated electron data library(EEDL)[10]. These data libraries contain all the interaction models for electron passing through the material medium. To describe the inner shell ionization, it uses Seltzer's [11] modification to the Moller's [12] binary collision cross section formula. Moller's formula is based on plane wave born approximation theory which was generalized to relativistic form in which electron wave functions are solutions of the Dirac equation and the interaction is represented by an effective Hamiltonian obtained from quantum electrodynamics. The penelope physics list of GEANT4 uses physics models used in the older version of PENELOPE simulation package[13]. In this version, the electron impact ionization of inner shells is simulated using cross sections obtained from an optical- data model of the Generalized oscillator Strength(GOS) [13, 14]. These cross sections are also obtained from an approximate formulation of the plane- wave (first) Born approximation (PWBA).

As the physics models used in the recent PENELOPE version i.e, PENELOPE2011 are not yet included in the penelope physics list of GEANT4, we have also used PENELOPE2011 package [15] for simulation. PENELOPE2011 uses most recent description of the ionization process. In the used version of the PENELOPE, more elaborate theoretical description of ionization cross sections is used in which, ionization cross sections are obtained from the Generalized Oscillator Strength (GOS) model based on relativistic distorted-wave Born approximation (DWBA). DWBA consistently accounts for the effects of both distortion and exchange[16].

The simulation was carried out with the exact conditions as in the actual experiment i.e, a pencil-like electron beam of 2 mm diameter falling on a thin target at normal incidence. The X-ray detector was placed at an angle of 135^0 with respect to the beam direction to record the emitted X-rays. Entry of the projectile electrons into the target, resulting ionization events and emission of X-rays were recorded event by event. From the simulation of a large sample of events, it was verified that the maximum probability of inner shell ionization per projectile electron remains less that unity so that the single collision condition is satisfied for all the target films used in the experiment. While generating simulated X-ray spectra by simulation, the process becomes inefficient and time consuming due to 1) low inner shell ionization and subsequent radiative decay probabilities, and 2) use of thin film media in the experiment. This results in large variance and reduces the predictive power of simulation. To reduce the time spent on computation and to increase the efficiency, it is necessary to use a variance reduction technique. It is implemented by artificially increasing cross section relevant to the process by some weight factor F, but keeping the probability distribution functions for energy loss and angular deflections same as for the real process. Finally, the biasing introduced by the simulation process is corrected for by applying appropriate statistical weights.

Subshell resolved L-shell ionization cross sections are obtained for three high Z elements (Gold, Lead and Thorium) in the energy range 16-45 keV using setup described above. Also, the simulations in GEANT4 and PENELOPE are made for all of them to estimate the effect of elastic scattering. The experimentally obtained production and ionization cross sections are compared with the predictions of DWBA and MRBEB theories. The DWBA results are obtained from the five coefficient analytical formula published by Bote et al.[4] while MRBEB results are provided by Guerra et al. [3]

It is seen that for all the elements investigated in the thesis, the L_3 subshell

ionization cross sections are explained well by the DWBA theory. As L_α and L_l lines arise mainly from the filling of vacancy in the L_3 subshell, the production cross sections for these X-ray lines are also predicted very well by DWBA theory. MRBEB theory is also good at predicting the ionization cross section of L_3 subshell and production cross sections of lines emerging from it, although on an absolute scale, it predicts higher cross sections by about $\sim 10\%$. For L_β and L_γ lines, the DWBA theory results are higher by $\sim 30\%$ and $\sim 50\%$ respectively for all the three elements. The agreement between theory and experiment is slightly better for Au L_β line, especially at lower energies ($16 < E < 25$). When our measurements are compared with the recent measurements of Wu et al. [17, 18] and Moy et al. [19] for L_α and L_β lines of Au and Pb, it is seen that our results are in accordance with their published data within the experimental uncertainty. Unfortunately no recent data exist for L_γ line of Au and Pb, or for any L X-ray line of Th in the studied energy range.

For L_2 and L_1 subshells, it is found that the theoretical results are higher by about 30 to 50 % for all the elements. The discrepancy is more for L_1 subshell than for the L_2 subshell. It is important to note that the obtain ionization cross sections generally depend on the relaxation parameters. From our studies[20], we see that the discrepancy between theory and experiment can be due to the poorly known relaxation parameters, specifically the relaxation parameters related to the L_1 subshell. It is difficult to draw a specific conclusion for the relaxation parameters related to L_2 subshell, due to the fact that the L_2 ionization cross section, obtained using L_γ line production cross section is lower than the theoretical estimates by $\sim 40\%$. But the L_β line production cross section values, which have almost equal contribution from L_2 and L_3 subshells, are explained reasonably well by the DWBA theory, specifically for Lead and other high Z elements [20, 21]. The detail results for each element and finding based on the variation of relaxation parameters done this

work will be presented in the thesis.

The thesis consists of six chapters which are structured as follows.
The first chapter of the thesis presents a general introduction to the subject of inner shell ionization, and establishes the motivation for the present study. Along with this, the first chapter also provides the introduction to various experimental techniques used to obtain the ionization cross sections. Chapter two gives a brief account of the various theoretical models that predicts the inner shell ionization cross sections and outlines two theoretical models in detail with which have been compared with our experimental results. The experimental techniques, which are used in our experiment are discussed in third chapter which include details of target preparation, target thickness measurements, determination of the efficiency of the detector used etc. Along with the experimental techniques, the third chapter also presents the data analysis procedure and various correction process, which are used to obtain the ionization cross sections. In fourth chapter, the simulation of electron impact ionization using GEANT4 and PENELOPE package is illustrated. The details of GEANT4 and PENELOPE simulation packages along with the results obtained for inner shell ionization studies is given in this chapter. Fifth chapter of the thesis carries all the experimental results on the production cross sections and ionization cross sections along with the discussion on the dependence of cross sections on the involved relaxation parameters. The last chapter of the thesis sheds some light on the summary and conclusion of the present work along with the future scope of such studies. Appendix A list various parameters used to obtain the cross sections. Appendix B list all the obtained cross sections from these studies.

The tables, figures, equations and references have been numbered serially and chapterwise. Any omission of a published reference due to oversight is deeply regretted.

List of Figures

List of Tables

CHAPTER 1

Introduction

1.1 Electron Impact Ionization

Electron collision with atoms or molecule is a prevalent process in nature and also plays an important role in many applications [1, 22, 23]. While the fundamental interaction(electromagnetic) between electron and atom is well known, exact knowledge of electron interacting with complex atoms is incomplete and is still the area of active research. Electron collision with an atom is, in general, a complex dynamical phenomenon and the interaction can result in processes like elastic scattering dominating at low electron impact energies or inelastic collision when the projectile energies are above the ionization potential of an atom. When an electron interacts with an atom inelastically, the collision can either result in excitation of the atomic electron to the quasi-bound state, or to the continuum leading to the ionization of an atom.

The electron impact ionization process of atoms is, in general, studied from various aspects, such as (i) shell specific ionization studies, (ii) measurement of total ionization cross sections, or (iii) correlation studies by detection of electrons

after the collision in e-2e type of experiments [24]. Although all the electron impact ionization is, in principle, e-2e type of collisions (i.e, one electron in input channel and two electrons in output channel), the experiments in which two outgoing electrons (i.e, projectile electron and the ejected electron) are detected in coincidence after the collision are popularly known as e-2e studies. These experiments involve the systematic measurements of the triple differential cross sections which are proportional to the probability that the two outer channel electrons will be moving in particular directions with particular energies after the ionization event.

As many of the applications mentioned below require knowledge of total the ionization cross sections [25], experiments are performed to measure the total ionization cross sections. These experiments make use of mass spectroscopic techniques to measure the total ionization cross sections [26, 27] which is proportional to the probability of occurrence of ionization event. In such experiments, the information about detail dynamics of the ionization process (i.e, which or how many electrons are being ejected from the atom) is not retrieved.

In the shell specific ionization studies, the ionization process is studied with the focus on the ionization of atom by ejection of electron belonging to particular shell or subshell. When the shells under investigation are inner shell viz, K, L or M then it is called inner shell ionization studies [1]. These experiments rely on the secondary photons or electrons, emitted due to relaxation of the ionized atoms for retrieving the details of the ionization process [2].

Theoretically, atomic ionization can be expressed in terms of the various cross sections, for example, total cross section, partial cross sections, and differential cross sections corresponding to various degrees of electron spin and correlation effects [25]. A restrictive representation of ionization is provided by the determination of the energy and momentum of all particles involved in the collision process. The triple

differential cross section (TDCS), in the case of single ionization under electron impact, is represented as, (see Ehrhardt et al. [28]):

$$\frac{d^3\sigma}{dEd\Omega_A d\Omega_B} = f(E_\circ, E_A, E_B, \theta_A, \theta_B) \tag{1.1}$$

The double differential cross section (DDCS), differential in the energy of the scattered electron and the direction of one of the outgoing electrons, can be obtained by integrating the TDCS over the direction of one of the outgoing electrons. The integration of TDCS over the direction of both the outgoing electrons yields single differential cross section (SDCS), which is differential in energy (or scattering angle) of the secondary electron. Further integration of the SDCS over energy (or an angle) of the secondary electron yields the total ionization cross section. Experimentally obtained total ionization cross sections for inner shell ionization are compared with the theoretical cross sections, against which, different theoretical models can be benchmarked to be used in various applications. The details of theoretical models which are successful in explaining the inner shell ionization will be presented in the next chapter.

From the practical point of view, electron impact ionization data is of great importance in many applications like electron probe microanalysis (EPMA), electron energy loss spectroscopy (EELS), Auger electron spectroscopy (AES), which are widely used in materials characterization. In fact, the inner shell ionization cross section data are essential in the sensitivity analysis, choice of detector configuration (eg. detection techniques to be used, type of materials and thicknesses to be used as an absorber, etc.), and the detection strategies to be incorporated into such analytical instruments [1]. Electron transport simulations, which are essential in the field of medical science, particularly in electron linac-based medical imaging, diagnosis, and cancer therapy, require a reliable cross section database for error-free patient management [22]. These important applied areas, require continuous quantities of

electron impact cross section data for different targets over a wide range of energy values, and with an acceptable accuracy level.

In the field of X-ray astronomy, the importance of atomic data need not be over-emphasized. There are many features in the X-ray band of the emitted photons that require detailed knowledge of the collisional transition rates and the radiative transition rates of the constituent systems. Since the astronomical sources that emit X-rays (usually the supernova remnants in various galaxies) are far from thermodynamic equilibrium, the instruments or detection systems used in space stations and in spaceborne X-ray telescopes with even the highest resolving power are not capable of fully resolving the X-ray lines due to the above reason. The field of observational astronomy has evolved rapidly so that collisional model-based interpretation of a wide range of data assumes particular significance [23]. In this context, benchmarking these models with laboratory-based measurements, such as the ones attempted in this work, becomes all the more relevant.

In the current thesis, we have studied the inner shell ionization process by electron impact, specifically, subshell resolved L-shell ionization in high Z elements. Subshell resolved ionization cross sections were obtained for Gold, Lead, Bismuth, Thorium and Uranium from the experimentally measured yields of characteristic X-ray lines originated from L shell. To correct for the experimental bias, the electron transport simulation inside the studied elements is also done using Monte Carlo Methods. Experimentally obtained results are compared with various theoretical models predicting these cross sections, such as Modified Relativistic Binary Encounter Bethe (MRBEB) [3] and also the Distorted Wave Born Approximation (DWBA) based results of Bote et al. [16].

In the rest of the chapter, we provide the details of relaxation process, emission of the secondary particle after ionization and the various experimental

procedure/technique to obtain the ionization cross sections from these secondary particles.

1.2 Inner Shell Ionization and Relaxation process

The vacancy created in the inner shell of an atom can decay through various channels bringing the atom back to its ground state. The ionized atom can de-excite by a dipole transition resulting in an emission of photons or alternatively a radiationless transition may take place in which the available energy is transferred to an electron ejecting it out of the atom.

1.2.1 X-ray Emission

The process leading to the photon emission can be represented as,

$$p + A \longrightarrow p + A^{+} + e_{ej.} \longrightarrow p + A^{+} + e_{ej.} + \gamma \tag{1.2}$$

where p is projectile, A is target atom, $e_{ej.}$ is the inner-shell electron knocked off in collision and γ is the photon of energy $h\nu = E_v - E_\circ$, where E_v is the energy of the subshell where vacancy is created and $E_\circ$ is energy of the subshell where the vacancy is transferred resulting in emission of photon. When the ionization of an atom occurs by removal of an orbital electron having binding energy in the range of keV, the emitted photon will be in the X-ray region of the electromagnetic spectrum. The emission spectrum generated through such electromagnetic transitions is a discreet (line) spectrum which forms a simple series. The X-rays which originate due to filling of the vacancy created in K shell are called K_α, K_β, ... lines, which correspond to the transitions L $\rightarrow$ K, M $\rightarrow$ K, ... respectively. Historically, the strongest transitions were named in the order as α, followed by β etc.. Similar to K shell, series of lines named as L_α, L_β etc., arise from transitions caused by filling of vacancies in the L shell.

For the shells higher than K shell, the spin-orbit coupling interaction splits the energy levels depending on the angular momenta associated with those levels. For example in the L shell, the bound electrons with $l = 0$ have the greatest binding energy, followed by electrons with, $l = 1$, $j = \frac{1}{2}$, and then those with $l = 1$, $j = \frac{3}{2}$. The three levels are labeled $L_1(2\ ^2S_{\frac{1}{2}})$, $L_2(2\ ^2P_{\frac{1}{2}})$and $L_3(2\ ^2P_{\frac{3}{2}})$ respectively. Due to this energy difference between sub-shells, the K_α line is further resolved into the doublet K_{α_1} and K_{α_2}, which corresponds to the transitions $L_3 \longrightarrow K$ and $L_2 \longrightarrow K$ respectively. The scheme of filling of vacancies created in K, L and M shells, leading to the emission of various X-rays following dipole transition rule is shown in Figure 1.1.

1.2.2 Auger Electron transition.

The other competing process contributing to the rearrangement of bound electrons in the atom following ionization is the emission of an electron, which is an "autoionization" decay. In the process of autoionization decay, the vacancy is transferred to other outer shells and the released energy is imparted to one of the bound electrons. The process of auto-ionization can be classified into two distinct types, such as Auger transition and Coster-Kronig transition or Super Coster- Kronig transitions. The process of Auger transition can be represented as,

$$p + A \longrightarrow p + A^+ + e_{ej.} \longrightarrow p + A^{++} + e_{ej.} + e_{Au.} \tag{1.3}$$

where the notations have the same meaning as in the case of photon emission and $e_{Au.}$ is an Auger electron emitted with energy $E(e_{Au.}) = E_v - E_o - E_b$. Here, E_v is binding energy of shell where vacancy is created, E_o is the binding energy of the shell where vacancy is transferred and E_b is the binding energy of the other bound electron which is knocked out as an Auger electron.

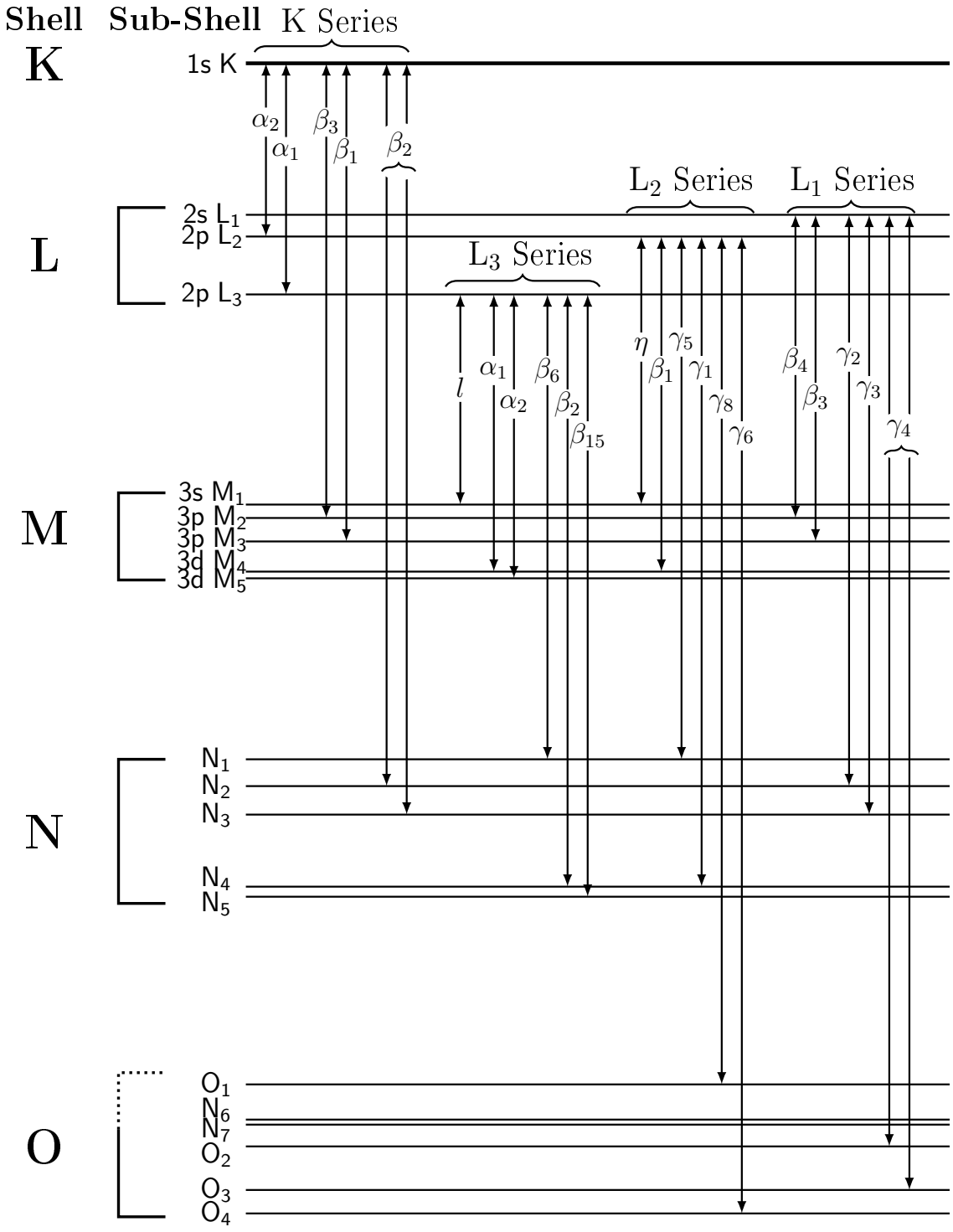

Figure 1.1: Electron transition scheme for X-ray production.

It should be noted that the Auger transition leaves the atom doubly ionized. Auger emission process can either occur as a two-step process as described above or as a single step process as shown in Eqn 1.4. It has been found that the direct double-ionization, as a one-step as indicated in Eqn 1.4, has much lower probability than the two-step transition(see Eqn. 1.3)[25]

$$p + A \longrightarrow p + A^{++} + e_{ej.} + e_{Au.} \tag{1.4}$$

Auger transitions are usually denoted by $X - YZ$ or simply XYZ, where X refers to the initial vacancy shell and YZ represents the final two vacancies. For example, KLL Auger electron means that initially an electron was knocked out of the K-shell causing ionization and subsequently, the vacancy is transferred to the L-shell, followed by emission of an L-shell electron (Auger electron). Similarly, KMM, LMN, Auger transitions are possible, whereby the subshells can be classified in addition by KL_IL_2 or KL_1L_3.

In a radiationless transition, if one of the final vacancies occurs in the same main shell but different sub-shell, then that transition is referred to as Coster-Kronig(CK) transition, for example, L_1L_3M. Coster-Kronig transitions may sometimes be much more probable than the competing Auger or X-ray transitions,(e.g. L_1L_3M vs L_1MM) but the emitted electrons consequently have less energies.

A special case of CK transition, known as Super Coster-Kronig (SCK) transition is also possible when both the final vacancies occur in the same main shell. Because of the energy constraints, these transitions can only occur in atoms with atomic number $Z \geq 40$ [29]. Figure 1.2 shows the various transitions discussed above.

1.2.3 Transition Probabilities and Emission yield

Each vacancy created has a finite lifetime and decay with particular transition probability via specific decay channel. Depending on the nature of transitions, these

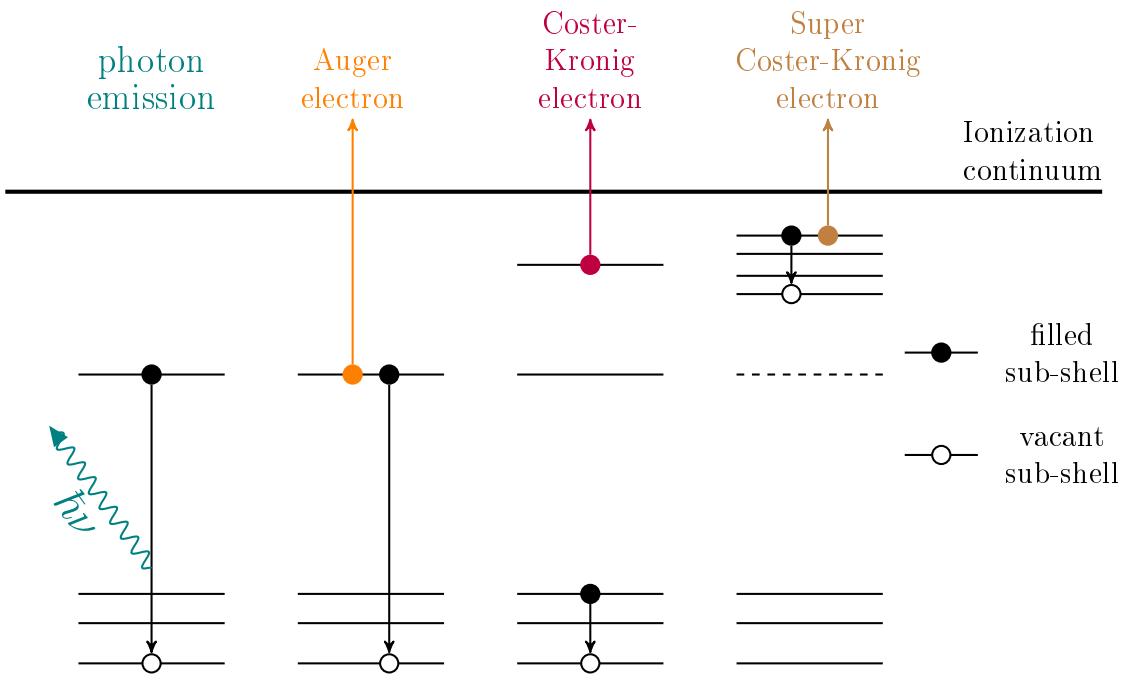

Figure 1.2: Schemes of various transitions caused by vacancy formation in the inner shells.

probabilities are referred to as the radiative and non-radiative yields. While extracting the ionization cross sections from measured X-ray production cross sections, these yields are the essential input, which can be obtained from either earlier published experimental data tables or theoretical calculations. A detailed review on X-ray fluorescence yields, Auger, and Coster-Kronig transition probabilities is published by Bambynek et.al [30].

1.3 Measurement of Inner shell Ionization cross sections(ICS)

The experimental measurement of the inner shell ionization cross section by electron impact has been a subject of continuing investigations for many decades. The review, done by Powell [1], discusses, the methods for measuring the ionization cross sections with the description of difficulties in obtaining these cross sections at

the desired accuracy for applications like EPMA, AES, and EELS. In this section, the overview of all the methods that have been used for the determination of ionization cross sections, with different types of materials is given. As there are numerous measurements of ionization cross sections using various techniques for experiment or of data analysis, only the work done over the last two decades is mentioned here, unless the mentioned methods and techniques were reported earlier, but can be considered as the benchmark for this type of measurement.

Although relative measurements of ionization cross sections were done earlier by Webster et al. [31],the first absolute measurements of ionization cross sections were performed by Clark [32] in 1935 for ionization of Silver by electron impact at 70 keV. After Clark's measurement, Smick and Kirkpatrick [33] had measured K-shell ionization cross sections of Ni by electron impact of 70 keV. After these pioneering measurements, there were few more K-shell ionization cross sections measurements done by various researchers, but it was not until 1964 when Green [34] measured the first L-shell ionization cross sections. In the papers published by Green in 1964 [34], and Green and Cosslett [35] in 1968, they reported ionization cross sections of L_2 and L_3 subshells of Gold. In 1995, Joy [36] compiled the ionization cross sections data for various elements available till December 1994. Close inspection of these values revealed that the results were still sparse for many elements and that significant discrepancies could be found between the results by different authors. These discrepancies were often larger than the claimed experimental uncertainties. The situation for L- and M-shell ionization cross sections was even worse due to the more complicated data analysis that is required. Since then, only a few more measurements have been reported for L and M-shell ionization cross sections.

The emitted characteristic X-rays or the Auger electrons are signatures of the particular shell being ionized either directly in collision process or indirectly via

vacancy transfer; and due to this property, the measurements of X-ray yields and Auger electron yields are the principle methods for obtaining ionization cross sections for almost all the elements. Since only one shell is present in H and He, ionization cross sections for these two elements have also been deduced from H+ and He+ ion yield or secondary electron numbers using crossed-beam methods. Also, a few results are obtained from the EELS spectra. All the above methods have been used to obtain the ionization cross sections of K shell, but L-shell ionization cross sections have been measured only from the X-ray yields or in some cases, from the Auger electron yields.

1.3.1 X-ray Production Cross Sections

The determination of the inner shell ionization cross section σ_X from the X-ray yield N_X can be considered as a two-step process. In the first step, the experimentally measured X-ray yield of the considered X-ray transition is converted into the X-ray production cross section σ_X of that X-ray transition. This conversion depends essentially on the type of target used and varies with the experimental technique. Target is the term used for material being studied, as the material can be either in the gaseous state (gas jet or vapor) which is called gas target or in solid form (thin or thick film target). The target can be either in different physical form i.e, solid or gases or in different chemical form i.e, of some compound or alloy. While evaluating the ionization cross sections from the experimental data it is assumed that the measured cross sections do not depend significantly on the physical or chemical state. For example production cross sections measured for K_α line of Carbon will be same if it is measured either using thin films of graphite or from the CH4 gas provided proper procedure is followed to convert the experimentally obtained X-ray yield to production cross section.

In the second step, the X-ray production cross sections are converted into the

inner shell ionization cross sections. The second step depends on the shell which is being studied. In K shell, as the ionization can only occur due to electron impact, the conversion is straightforward using only fluorescence yields. But for L and other outer shells, it becomes more complicated due to the presence of sub-shells and vacancy transfers via many competing processes. The complexity arises from the fact that vacancies in outer shells can be produced not only by the direct impact but also by Coster-Kronig transitions, super-Coster-Kronig transitions, and radiative and nonradiative transitions to inner shells.

The measurement of X-ray production cross sections are performed in a wide variety of experiments like energy dispersive X-ray fluorescence (EDXRF) experiments in which, the target is excited by X-rays [37], particle/proton induced X-ray emissions (PIXE)[38, 39] etc. For electron impact, measurements of X-ray production cross sections have been performed by bombarding a target containing the elements under investigation with electron beam obtained from a wide variety of instruments that range from linear electron accelerators to electron microscopes. In the early days of such studies, measurements of X-ray yield were carried out using scintillation crystals and gas ionization based proportional counters. Over the years, as technology evolved, earlier detectors were replaced by energy-dispersive solid state detectors like liquid nitrogen cooled Lithium-drifted Silicon (Si(Li)) detectors or planar high-purity Germanium (HPGe) detectors, or by high resolution wavelength-dispersive bent crystal spectrometers.

All the detectors used for X-ray yield measurement, forms the two major types of detection systems, namely, wavelength dispersive spectrometer and energy dispersive spectrometer. The difference between these detection systems arises because of the way the measurement is done. In wavelength dispersive type of measurements first the emitted X-ray is dispersed using a good quality crystal, called the monochromator,

through Bragg reflection and the X-rays of particular energy are counted using the proportional counter [40]. These type of detector system have very high resolving power ($\sim 1-2$eV FWHM at 1keV) but have comparably lower detection efficiencies. Energy dispersive X-ray spectrometer consists of solid-state detectors in which the whole spectrum of emitted X-rays is detected at a time. This type of detector system have comparatively higher efficiency, but less resolving power (typically$\sim$ 150 eV FWHM at 5.9 keV). Both the methods are used actively to obtain the production cross sections. As recent examples of such measurements, Rahangdale et al. [20, 21] and Barros et.al [41] have employed energy dispersive spectrometer for extracting the L-subshell ionization cross sections in Gold, Lead, and Thorium, while wavelength dispersive spectrometer was used by Moy et.al [19, 42] to obtain production cross sections of Pb and Th.

The X-ray yield N_X obtained for a particular transition from any of the method discussed above is converted into production cross section σ_X using the following relation,

$$\sigma_X(E) = \frac{4\pi}{\epsilon\ \Delta\Omega\ N_e\ t\ \mathcal{N}}\ N_X, \tag{1.5}$$

where N_e is the number of incident electrons, t is the thickness of target, $\mathcal{N}$ is the density of atoms in the target(atoms per unit volume) and ϵ is the efficiency of the detector which is ratio of number of X-rays detected to the number of X-rays reaching the detector, and $\Delta\Omega$ is solid angle of the detector opening. The above formula assumes that thickness of target is so small that the projectile electron follows the straight line path, and the emission of X-rays is isotropic, which is true for some X-rays transitions, but special treatment is needed either experimentally or while analyzing the data, when dealing with X-ray transition which has anisotropic distribution [43].

In the equation 1.5 efficiency (ϵ) is the parameter related to the detection system and needs to be calibrated separately for each system. Efficiency measurements in

both the spectrometer systems described above can be done by various methods, and the most commonly used method is based on the calibrated radioactive sources [44]. Other methods make use of Synchrotron radiation [45] or bremsstrahlung radiation [46]. Feasibility study of the latter method and related measurements done in this thesis work will be illustrated in Chapter 4.

Various kinds of targets have been used to obtain the production cross sections, the main distinction being solid and gas targets. Solid targets are generally in the form of bulk films and both thin film and thick film targets are used. The main advantage of using thin film target, especially for electron impact excitation, is the minimization of electron energy loss within the target. This provides better energy definition for the cross section data extracted from the X-ray yield measurements. The disadvantage of thin film target is obviously the level of difficulty in preparation, handling and characterization of the materials due to its fragile nature. While it is naturally easier to prepare and handle thick film targets, the data analysis for extraction of relevant cross section as a function of energy become more complicated. Complications arise due to the effect of multiple scattering and energy loss within the target. Such measurements were recently made by Zhu et al. [47]. In this study, the assumptions were made that electrons move in straight-line trajectories in the target, and that there is no contribution due to ionization by bremsstrahlung and by backscattered electrons (with energies larger than 50 eV) to the measured X-ray yield [48]. Due to these assumptions, the obtained production cross sections are valid for low-Z elements and overvoltages $U = E/E_i < 6$ where E is the projectile electron energy and E_i is binding energy of the shell being ionized by electron impact.

Most of the X-ray yield measurements in the past were done using the thin film solid targets. Thin film targets can be either self-supporting or to avoid the film breakage of very thin targets, they are often backed by a thin or thick substrate of low

Z elements like Carbon, Aluminum or low Z compounds, such as Mylar. When using thin films as targets generally the thickness measurement is the most important source of systematic errors. These errors can reach up to 30% depending on the thickness measurement technique used and the target thickness itself. Various techniques are employed to measure the thicknesses such as Rutherford backscattering spectrometry, X-ray fluorescence, quartz crystal microbalance.., etc. Quartz crystal microbalance is also used as thickness monitor in various target preparation methods. Other problems associated with the use of thin film are wrinkling, non-uniformity, clustering, and islanding. If the thin film with backing is used in the experiment, an additional correction is required to account for the enhancement of X-rays occurring due to the electrons backscattered from the backing film. Many recent measurements are done using the thick substrate backed targets [49–53]. Contribution to ionization yield caused by the backscattered electrons in such backed target experiments can be as high as 15%, especially for low Z substrate like carbon [54]. For such targets, the X-ray production cross sections is given as the difference of direct and indirect contributions,

$$\sigma_X = \sigma_d(E) - \left[\int_{E_i}^{E} dE' \sigma_X(E') \int_{-1}^{1} d(\cos\theta') \frac{d^2\eta_b}{dE' d(\cos\theta')} |\cos\theta'|^{-1}\right] \qquad (1.6)$$

where $\sigma_d(E)$ is the direct X-ray production cross section obtained from the observed yield and obtained using Eqn 1.5, and $\frac{d^2\eta_b}{dE' d(\cos\theta')}$ is the energy distribution of electrons backscattered from substrate. This quantity is generally obtained from the electron transport calculations, such as the bipartition model [54] or from Monte Carlo simulations using general-purpose codes such as EGS4 [55] or PENELOPE [9]. In this process of obtaining production cross sections the iterative method is required as the quantity σ_X also occurs in the right-hand side integral of Eqn 1.6.

The problems associated with the use of thin film targets can be eliminated by use of gas targets. Low-pressure gas targets ($\approx 10^{-3}$ mbar) have been used to obtain

the production cross sections. For gas target Eqn 1.5 is modified as

$$\sigma_i(E) = \frac{4\pi}{\epsilon\ \Delta\Omega\ N_e\ l\ \mathcal{N}}\ N_X, \tag{1.7}$$

where the thickness of thin film target is replaced by l, which is the distance traveled by the electrons inside the gas target. The quantity l can be obtained to the precision of 2% using pressure and temperature measurements [56].

Lastly, the emitted bremsstrahlung can be used to obtain the absolute X-ray production cross sections. In this technique, the yield of characteristic X-rays is normalized by the yield of simultaneously emitted bremsstrahlung radiation. This technique was first introduced by Hippler [57] and recently it was used by Singh and Sankar [58] to obtain production cross sections of argon, and Campos et al. [59] for production cross section of Tungsten, Platinum, and Gold. By using bremsstrahlung radiation for normalization, additional parameters such as the target thickness, detector efficiency, number of incident electrons are not needed; as these quantities cancel out in the normalization process. Furthermore, estimation of cross sections from the experimental results becomes free from measurement uncertainties of some of these parameters. The double differential cross section of bremsstrahlung photon emission is given as,

$$\frac{d^2\sigma_b}{d\Omega dE} = \frac{N_b}{N_e \epsilon t \mathcal{N} \Delta\Omega \Delta E} \tag{1.8}$$

where N_b is the number of bremsstrahlung photons emitted in the energy interval ΔE centered around energy E. If the ratio of the cross section for characteristic X-ray emission Eqn 1.5 and bremsstrahlung emission 1.8 is taken and assuming that the bremsstrahlung is measured near the characteristic X-ray, peak such that the intrinsic efficiency of the detector ϵ is approximately equal for both the energies, the relation between both the cross sections is given as,

$$\sigma_X = 4\pi \frac{N_X}{N_b} \frac{d^2\sigma_b}{d\Omega dE} \Delta E \tag{1.9}$$

The production cross sections measured by this method depends on upon bremsstrahlung cross sections for its reliability. State-of-the-art bremsstrahlung cross sections tabulated by Kissel et al. [60] are believed to be accurate to about 10% and have been used to determine inner shell ionization cross sections [59, 60].

1.3.2 Ionization Cross Section using Auger Yield

Inner shell ionization cross sections are also obtained using Auger electron measurements for gasses, solids, atoms and molecules adsorbed on solid surfaces [61–63]. Here we will limit our discussion to the ionization cross sections obtained using gas targets, solid targets, and target elements adsorbed on solid surfaces [63, 64].

The fluorescence yield for all the inner shells of elements with low atomic numbers($Z \leq 10$) or for inner-shells having low binding energies ($\approx 1keV$) of all the elements, is found to be very small (typically less than 0.01). In such cases, the fluorescence (ω_i) yield is assumed to be equal to zero, which is reasonable assumption because in the experiments there are sources of much larger uncertainties. For such cases, ionization cross sections measurements using Auger electron yield is more appropriate and feasible. Similar to X-ray production cross sections, Auger electron production cross sections σ_A can be obtained from the Auger yield N_{Au} as,

$$\sigma_A = \frac{N_{Au}}{N_e \, \mathcal{N} \, \epsilon_e \, l} \tag{1.10}$$

where N_e is number of incident primary electrons, $\mathcal{N}$ is number density of target elements, l is the path length of the projectile inside the target and ϵ_e is the detection efficiency of electron spectrometer. Instead of using all the quantities described in Eqn 1.10, the normalization of Auger yield to obtain production cross sections is done using the elastic scattering cross section data through the similar process as described for normalization of X-ray yields using bremsstrahlung cross sections.

Assuming isotropic distribution of auger electrons, the relation between Auger

yield and elastically scattered electron yield can be written as,

$$\sigma_A = 4\pi \frac{N_{Au}}{N_{el}} \left(\frac{d\sigma_{el}}{d\Omega} \right) \tag{1.11}$$

where, N_{el} elastically scattered yield of primary beam and $\frac{d\sigma_{el}}{d\Omega}$ is elastic scattering differential cross sections of primary beam.

Inner shell ionization cross sections using Auger yield were first measured by Glupe and Melhorn [61] using the normalization process described above. The measurements were done for C(C in CH_4), N, O and Ne; and the normalization of cross sections was done using the calculated and measured differential cross sections for elastic scattering of electrons by Helium. Later the experimental procedure was modified by Hink, Brunner, and Wolf [65] so that the yield of Auger electrons was normalized to the simultaneously measured yield of the elastically scattered primary electron beam.

1.4 Perspective of Thesis Work

The first absolute ionization cross sections were measured by Clark [32] in 1935. After this first measurements, there have been several measurements over the past 70 years; still, the experimental study of ionization cross sections is far from complete. To quote from the recent compilation on electron impact ionization cross sections done by Joe [36] "the amount of data available is small for K-shells, negligible for the L-shells, and all but non-existent for the M- and higher shells". The work done by earlier researchers was mainly restricted to low-Z elements. Also most of the time only the production cross section data is reported due to its direct usability in the application like EPMA, and ease of measurements. Table 1.1 shows the earlier work done to obtain the L-shell X-ray production cross sections of Gold, Lead, Bismuth, Uranium, and Thorium.

Element	**sub-shell**	**Energy Range (keV)**	Substrate	**Ref.**
Au, Bi	L_X	$3 \times 10^4 - 9 \times 10^4$	Self supported	Middleman et al. [66]
Au, Pb	L_α,L_β,L_γ, L_l, L_X	$300 - 600$	Self supported	Schlenk et al. [67]
Au, Pb, Bi	L_α,L_β,L_γ	$60 - 600$	Self supported	Pàlinkàs et al. [68]
Au	L_α,L_β,L_γ	$12 - 25$	Self supported	Shima et al. [69]
Au	L_α	$12 - 30$	Thick substrate	Campos et al. [59]
Au	L_α,L_β	$14 - 25$	Thick substrate	Wu et al. [17]
Pb, Bi	L_α,L_β,L_γ	1.39×10^3	Self supported	Park et al. [70]
Pb	L_α,L_β	$16 - 40$	Thick substrate	Wu et al. [18]
Pb	L_α,L_β	$13 - 36$	Self supported	Moy et al. [19]
Bi	L_α,L_β,L_γ, L_l	$300 - 600$	Self supported	Ricz et al.[71]
Bi	L_α,L_β	$17 - 40$	Thick substrate	Wu et al.[72]

Table 1.1: List of similar studies on the heavy elements(Gold, Lead, Bismuth etc,) L X-ray production

For the elements studied in this thesis, only few dataset exists for ionization cross sections of Gold while no data is available for Lead and Thorium. Some groups have reported the production cross sections of Lead for L-shell X-rays. Earlier the studies were reported for Gold by Green [34], Green, and Cossellet [35] and Salem and Moreland [73] for the ionization of L_2 and L_3 subshell. Davis et al. [74] reported the L_3 subshell ionization cross sections. Out of these studies, Davis and Green ignored the Coster-Kronig transition probability while obtaining ionization cross sections from the production cross sections. First systematic studies by Palinkas and Schlenk [68] reported $L_\alpha, L_\beta, L_\gamma$ production cross sections and obtained L_1, L_2, L_3 ionization cross sections for Gold, Lead and Bismuth in the energy range 60-600 keV. Shima et al. [69] did experiments near ionization threshold and reported $L_\alpha, L_\beta, L_\gamma$ production cross sections of Gold over energy range 12.26-25 keV and L_3 ionization cross sections over very short energy range of 12.26 to 13.60 keV. In Shima's study of L_3 sub-shell ionization cross sections, the energy range was such that only L_3 was ionized, which eliminated the use of Coster-Kronig transitions probability to obtain the ionization cross sections from production cross sections of L_α line. Schneider et al., [75] had reported L_3 ionization cross section by electron and positron impact near ionization

Element	**sub-shell**	**Energy Range (keV)**	**Substrate Type**	**Ref.**
Au	L_2,L_3	$13.6 - 41.7$	Thick Substrate	Green [34]
Au	L_2,L_3	$14.9 - 41.2$	Thick Substrate	Green et al [35]
Au	L_2,L_3	$13.6 - 41.2$	Thick Substrate	Salem et al [73]
Au	L_3	$20 - 140$	self supported	Davis et al. [74]
Au, Pb, Th, U	L	1.5×10^5	self supported	Ishii et al. [77]
Au, Pb, Bi, U	L	$2.0 \times 10^4 - 6.0 \times 10^4$	self supported	Hoffmann et al. [78]
Au, Pb, Bi	L_1,L_2,L_3	$60 - 600$	self supported	Palinkas et al. [68]
Au	L	$9 \times 10^5 - 2 \times 10^6$	self supported	Genz et al. [76]
Au	L_3	$12.26 - 13.6$	self supported	Shima et al. [69]
Au	L_3	$12 - 75$	self supported	Schneider et al. [75]

Table 1.2: Previous work on L shell ionization cross sections

threshold. Genz et al. [76] obtained the total L-shell ionization cross sections for Au, while Ishii et al. [77] and Hoffmann et al. [78] measured total L-shell ionization cross sections of Gold, Lead, Bismuth, and Uranium. In their measurements, Ishii et al. and Hoffmann et al. assumed the mean L-shell fluorescence yield using which, they obtained ionization cross sections from the sum of production cross sections of all the X-ray lines originating from the L shell.

The Table 1.2 shows the earlier work done to obtain the ionization cross sections with the type of target used and the energy range. From the experimental point of view, this review of the earlier work clearly shows the need for more improved ionization cross sections data near the ionization threshold for high Z elements.

Also from the theoretical point of view, the K-shell ionization cross sections can be explained very well by the theory but not the limited available data of L-shell ionization [2]. Unlike K shell, the L shell has three subshells with different properties. In order to test the validity of the theoretical models in a stringent manner, some groups have chosen the L-subshell as their area of investigation. The wave function of the subshells differs in their character. Because of small energy separation between the subshells and different characters of the subshell wave functions, data on L shell

would be a more stringent testing ground for the theory. With this motivation, we have undertaken the measurement of L-shell production cross sections of Gold, Lead, Bismuth, Uranium and Thorium and have obtained ionization cross sections from the measured production cross sections.

In case of Uranium and Thorium, the experiment is done with the thin films ($\approx 90\mu g/cm^2$) deposited on the comparatively thicker Aluminum foil ($\approx 200\mu g/cm^2$). As described in the Section 1.3.1, the use of backing can result in the enhancement of the X-ray yield due to backscattered electrons. To account for this backscattering factor, Monte Carlo simulation is done using the simulation package PENELOPE [9] and GEANT4 [8] Simulation is also used to ensure occurrence of only single ionization event, for the chosen thickness of all the targets, and to obtain the efficiency of the detector using the bremsstrahlung spectra of thick carbon and Aluminum targets. The details of the simulation with results are presented in Chapter 4.

This thesis is, therefore, based, on the following work

- L-shell X-ray production cross sections of Gold, Lead and Bismuth in the rage $16 - 40$ keV electron impact.
- L-shell X-ray production cross sections of Uranium and Thorium in the rage $20 - 45$ keV electron impact.
- L-shell ionization cross sections of Gold, Lead and Thorium in the rage $16 - 45$ keV electron impact.
- Measurement and simulation of thick foil Bremsstrahlung spectra of C by 25 keV electron impact to obtain detector efficiency.
- Electron transport simulation inside the thin film using PENELOPE and GEANT4.

CHAPTER 2

Theoretical Developments

2.1 Overview

Similar to the experiments for obtaining ionization cross sections, the theory for the ionization of atoms by the impact of charged particles has been a subject of continuous interest since the pioneering work of Thomson in the early 1910 [79]. Since the very beginning, the theoretical development of electron impact ionization can be said to have evolved along two different motivations, which can be roughly classified as, (i) complete and accurate description of electron-atom collision process using quantum mechanics and (ii) development of classical or semi-classical formulas for understanding the ionization mechanism and accurately reproducing the ionization cross sections. The first quantum mechanical description of ionization process was given by Bethe in 1930 [80] which was based on first Born approximation. After this first model of Bethe, there has been further development based on the similar framework as described by him; a good review on this topic is published by Powell [1]. Since the last two decades, there have been further renewed interest in the topic and further development in the form of more elaborate quantum mechanical models such

as close coupling theory, R-matrix theory, DWBA theory etc.

It is well-known fact that the differential cross section for non-relativistic Rutherford scattering between two charged particles is the same, whether it is calculated classically or exactly quantum mechanically, or using the (first) Born approximation. This remarkable circumstance encouraged many researchers to introduce classical methods of calculation into the theory of inelastic atomic collisions with the goal of computational simplifications. Alongside the elaborate quantum mechanical theories, development of classical models was necessary for ease of availability of cross section data. Before the widespread use of modern computers, the tedious calculations of quantum mechanical cross section data were not possible for all the applications, and classical and semiclassical formulas provided the way for quick calculations of such data. Review of Burgess and Percival [81] and of Vriens [82] provide an assessment of these theories.

A complete theoretical modeling of few body dynamics such as electron impact ionization is very challenging and still remains a fundamental unsolved problem in theoretical atomic physics [83]. The few-body problem arises from the fact that the Schrodinger equation is not analytically solvable for more than two mutually interacting particles. To add to this difficulty, the problem arises due to long-range nature of the Coulomb potential which ensures that the two continuum electrons interact with the residual ion and each other until they are well apart. A complete treatment of the ionization process, therefore, requires a full solution of the three-body problem in the asymptotic region. As a result, for three or more particles, a theory must resort to significant modeling efforts using several approximations, such as approximations about target states, incident particle waveforms and the neglecting correlation between the continuum electrons. The validity of such approximations is determined by comparison with experimental data. In the current chapter, we first

discuss the general scattering theory, with the next section on the discussion of various approximations to calculate the electron-impact ionization cross sections. The details of two models with which we have compared our experimental results to draw a conclusion have been presented in brief. These models are DWBA based calculations of Segui et al. [84] and semi-classical results of Guerra et al [3].

2.2 General Scattering Theory

Theoretically, the electron impact ionization of neutral atom is considered as a scattering problem within the quantum mechanical framework. In the simplest case of two-body collision, i.e., projectile scattering due to potential field of target, the Hamiltonian of the projectile motion is given as the sum of two parts,

$$H = K + V$$

where, K is kinetic energy operator, $K = -\frac{1}{2}\Delta^2$ and V is the potential, which represents the interaction between projectile and target. The state of the particle moving with energy E is then described as an eigenvector $|\Psi\rangle$, which are obtained as solution of the Schrodinger equation,

$$(E - H)|\Psi\rangle = 0 \tag{2.1}$$

where E is the energy of the projectile. In the absence of any potential i.e. $V = 0$ the equation (2.1) becomes,

$$(E - K)|p\rangle = 0 \tag{2.2}$$

where, $|p\rangle$ is the free particle state. In terms of the wave-function $\psi(r)$ associated with the eigenvector $|\Psi\rangle$, the Schrodinger equation is given as,

$$\left[-\frac{1}{2}\Delta^2 + V(r)\right]\psi(\boldsymbol{r}) = E\psi(\boldsymbol{r}) \tag{2.3}$$

where $V(r)$ is the scattering potential. The energy of an electron with momentum $\overrightarrow{p} = \hbar\overrightarrow{k}$ is,

$$E = \frac{p^2}{2m} = \frac{\hbar^2 k^2}{2m} \tag{2.4}$$

here, k is wave vector. Using Eqn. (2.4) in Eqn. (2.3) and defining, $U(r) = \frac{2m}{\hbar^2}V(r)$ we may write, Eqn. (2.3) as,

$$\left[\Delta^2 + k^2 - U(\boldsymbol{r})\right]\psi(\boldsymbol{r}) = 0 \tag{2.5}$$

Using scattering theory [85], it can be shown that the desired solution of the Eqn (2.5) should have an asymptotic form given by:

$$\Psi(\boldsymbol{r})_{r\to\infty} \to A\left(e^{i\overrightarrow{k}\cdot\overrightarrow{r}} + f(k,\theta,\phi)\frac{e^{+ikr}}{r}\right) \tag{2.6}$$

Where, A is the normalization constant which is independent of r and the angles θ and ϕ. Equation (2.6) describes that the wave-function for the steady state contains a plane-wave for the incident electron and spherical wave for the outgoing scattered electron. The function $f(k,\theta,\phi)$ is called the scattering amplitude. The relation between scattering amplitude and the differential cross sections is pretty straight forward [86] and is given as,

$$\frac{d\sigma}{d\Omega} = |f(k,\Omega)|^2 \tag{2.7}$$

In case of ionization where two electrons are present in the output channel, the fully differential cross section is calculated which is given as,

$$\frac{d^3\sigma}{dEd\Omega_A d\Omega_B} = \frac{k_A k_B}{k_{in}}|f|^2 \tag{2.8}$$

where labels A and B refer to the two electrons in the output channel.

The whole problem of obtaining the differential cross section then boils down to calculating the scattering amplitude by solving Eqn (2.5). There are various methods which can be employed to obtain the solution of Eqn (2.5).

One of the ways to obtain the wave-function in Eqn. (2.5) is by expressing it in an integral from i.e. Lippmann- Schwinger equation. To obtain the integral form of Eqn (2.5), let us rewrite it as,

$$\left[\Delta^2 + k^2\right] \psi_k(\boldsymbol{r}) = U(r)\psi_k(\boldsymbol{r}) \tag{2.9}$$

The general solution of Eqn. (2.9) is given as,

$$\Psi_k^{\pm}(\boldsymbol{r}) = \Phi_k(\boldsymbol{r}) + \int G_\circ^{\pm}(\boldsymbol{r}, \boldsymbol{r}')U(r)\Psi_k^{\pm}(\boldsymbol{r}')d\boldsymbol{r}' \tag{2.10}$$

The term $\Phi_k(\boldsymbol{r})$ is a solution to the homogeneous equation is

$$\left[\Delta^2 + k^2\right] \Phi_k(\boldsymbol{r}) = 0 \tag{2.11}$$

This wave-function is a plane-wave, which is given by:

$$\Phi_k(\boldsymbol{r}) = (2\pi)^{-\frac{1}{2}} \exp(i\boldsymbol{k} \cdot \boldsymbol{r}) \tag{2.12}$$

The function $G_\circ^{\pm}(\boldsymbol{r}, \boldsymbol{r}')$ in Eqn (2.10) is the Green's function for an incoming(-) or outgoing(+) wave. Equation (2.10) for outgoing wave can be written in the symbolic form as:

$$\Psi_k^{+} = \Phi_K + G_\circ^{+} U \Psi_k^{+} \tag{2.13}$$

The free particle Green's function $G_\circ^{+}$ satisfies the following equation:

$$\left[\Delta^2 + k^2\right] G_\circ^{+}(\boldsymbol{r}, \boldsymbol{r}') = \delta(\boldsymbol{r} - \boldsymbol{r}') \tag{2.14}$$

and its solution is,

$$G_\circ^{+}(\boldsymbol{r}, \boldsymbol{r}') = -\frac{1}{4\pi} \frac{\exp(ik|\boldsymbol{r} - \boldsymbol{r}'|)}{|\boldsymbol{r} - \boldsymbol{r}'|} \tag{2.15}$$

In integral form it can be written as,

$$G_\circ^{+}(\boldsymbol{r}, \boldsymbol{r}') = -\frac{1}{2\pi^3} \lim_{\epsilon \to 0^+} \int \frac{\exp(i\boldsymbol{k'} \cdot (\boldsymbol{r} - \boldsymbol{r'}))}{k'^2 - k^2 - i\epsilon} d\boldsymbol{k}' \tag{2.16}$$

For large r, $G_\circ^{+}$ can be evaluated as,

$$G_\circ^{+}(\boldsymbol{r} - \boldsymbol{r'}) \sim -\frac{1}{4\pi} \frac{\exp(ik\hat{r} \cdot \boldsymbol{r}')}{r} e^{ikr} \Bigg|_{r \to \infty} \tag{2.17}$$

where $\hat{r}$ is a unit vector in the direction of the scattered paricle and $|r - r'|$ is taken as r. The final momentum vector k_f is equal to $k\hat{r}$ and the initial momentum vector is k_i. Substituting Eqn (2.17) in Eqn. (2.10) we get,

$$\Psi^+_{ki}(\boldsymbol{r}) \sim \Phi_{ki}(\boldsymbol{r}) - \frac{\exp(ikr)}{4\pi r} \int \exp(-i\boldsymbol{k}_f.\boldsymbol{r'})\mathrm{U}(\boldsymbol{r'})\Psi^+_{ki}(\boldsymbol{r'})d\boldsymbol{r'}\Big|_{r\to\infty} \tag{2.18}$$

Eqn (2.18) is known as the *Lippmann-Schwinger* equation of potential scattering[87]. Comparing Eqn (2.18) with Eqn (2.6), the scattering amplitude can be given as, in Dirac Notation,

$$f(\theta,\phi) = -2\pi^2 \left\langle \Phi_{k_f} \left| \mathrm{U} \right| \Psi^+_{k_i} \right\rangle \tag{2.19}$$

In the above equation, factor in the right hand side is transition matrix element, i.e.

$$T_{fi} = \left\langle \Phi_{k_f} \left| \mathrm{U} \right| \Psi^+_{k_i} \right\rangle \tag{2.20}$$

As U is the only interacting part of Hamiltonian of the system, in terms of Hamiltonian Eqn (2.20) can be written as,

$$T_{fi} = -\left\langle \Phi_{k_f} \left| \mathcal{H}_{int} \right| \Psi^+_{k_i} \right\rangle \tag{2.21}$$

Finally the differential cross section can be written as,

$$\frac{d\sigma}{d\Omega} = 4\pi^4 \left| \left\langle \Phi_{k_f} \left| \mathcal{H}_{int} \right| \Psi^+_{k_i} \right\rangle \right|^2 \tag{2.22}$$

2.3 Approximation methods

The complete analytical solution of Eqn 2.22 is not possible in general and often one has to resort to the various approximations. Most studied of these methods is the First Born Approximation.

2.3.1 First Born Approximation

While using the First Born approximation to describe the collision process, the incident and scattered particles are considered as plane waves, and it is assumed that they remain undistorted by the interaction. This approximation is also referred as the plane-wave Born approximation(PWBA). In PWBA the projectile electron wave functions and the wave functions of the active target electron are not orthogonal, and hence within PWBA the electron exchange can not be accounted consistently and has to be taken care of separately [88, 89]. Due to its very assumption of low perturbation in the wave functions, PWBA results are valid for the high-velocity projectiles. Still to obtain the accurate cross sections within PWBA, the good quality wave functions of the stationary states of the colliding structures are required(more realistic than the mere hydrogenic wavefunctions). At the energies near ionization threshold of bound electron, PWBA usually overestimates the scattering cross sections. To describe the ionization of atoms by charged particle impact, PWBA was first used by Bethe in 1930 [80]. In his calculations, he neglected the influence of the core electrons on the incident projectile and considered the Coulomb interaction of the projectile with an active electron. Accordingly the unperturbed Hamiltonian is given as the sum of unperturbed atom Hamiltonian $\mathcal{H}_{\text{at.}}$ and free incident electron Hamiltonian $\mathcal{H}_{\text{e}}$ while the perturbation Hamiltonian $\mathcal{H}_{\text{int}}$ includes the electron-electron and electron-nucleus interactions, which causes transition of the atom from its initial ground state to the ionized state. The first Born approximation neglects the Coulomb force between the charged projectile and the target atom and relies on the use of unperturbed atomic wave functions.

2.3.2 Distorted Wave Born Approximation

Although the Born approximation is the first step in a systematic perturbation expansion, the next more realistic approximation after the PWBA can be done by considering the distortion of the incident and scattered waves occurring due to the static field of the target atom. These distorting effects are particularly important for the slow moving projectiles. This modification is called as distorted-wave Born approximation (DWBA). The practical way to achieve this is by replacing the projectile plane waves by Dirac distorted plane waves, which are the exact solutions of the Dirac equation for an electron in the atomic potential. The perturbation Hamiltonian $\mathcal{H}_{\rm int}$ consists of a potential V_{DW} which describes the interaction of the incident electron with the spherically averaged potential of the core electrons [84]. As the projectile moves slowly, an assumption can be made that the projectile "feels" the same potential as that of active target electron. Accordingly, then the wave functions of the projectile and target electrons are orthogonal and thus in DWBA consistent description of exchange effects can be provided. In comparison with the PWBA approaches, the DWBA provides much better agreement with experimental data at low energies if additionally the exchange effect/interaction is included. Various authors have reported DWBA calculations of ionization cross sections for ions [90, 91]. Due to the slower convergence of the partial-wave series, calculations for neutral atoms are much more difficult to perform and only recently Segui et al. [84] and Colgan and Fontes [92] have reported semi-relativistic DWBA calculations for neutral atoms.

2.3.3 Convergent Close Coupling (CCC)

Along with the above-mentioned and various other approximations or empirical formulas, a complete treatment using *ab initio* close coupling methods is performed. Historically this method was developed for studying the excitation processes, but it

is shown that CCC methods can also be used to describe the ionization process [93]. In this method, the incident electron is treated on the same footing as the bound electrons, and accordingly, the wavefunction for projectile-target system is expanded in terms of the complete set of eigenfunctions of the target Hamiltonian[94]. The system is then allowed to evolve in time and solution is sought for the time-dependent scattering problem. Various cross sections for excitations and ionization are obtained from the scattering probabilities. The difficulty, in the case of ionization, occurs due to the presence of an infinite number of states available for the free electrons in the continuum. This is taken care of by treating the continuum via the introduction of some function ϕ_n which is not a target eigenfunction but a function representing an appropriate average of bound and continuum states. These states which are not real are called pseudo-states. Among all methods, CCC is the most accurate one for obtaining the electron impact ionization cross section, but owing to its computational difficulty, only very simple systems are completely studied using CCC approximation [95].

2.4 Distorted Wave Born Approximation based Calculations

As indicated in the introduction section, we have compared our experimental results with two different theoretical calculations. These two theoretical estimations are (i) Modified Relativistic Binary Encounter Bethe(MRBEB) based calculations, which is a fully relativistic semi-classical model and (ii) fully quantum mechanical and semi-relativistic calculation based ionization cross sections used in PENELOPE2011 code [15]. Sub-shell resolved ionization cross sections database used in PENELOPE2011 is based on the calculations of Segui et al. [84] and Bote et al. [16]. Bote et al., [4] have parameterized this database, and each formula contains a number of

parameters which are characteristic of the element, the active electron shell and the projectile particle (as the database is valid for both electron and positron). This database is implemented in the PENELOPE code version 2011, which we have used to compare our experimental results.

These calculations employ fully relativistic Plane Wave Born Approximation (PWBA) and semi-relativistic Distorted Wave Born Approximation (DWBA) to calculate sub-shell resolved ionization cross sections for elements Z=1 to Z=99 in the energy range from ionization threshold up to 1 GeV. For projectile with kinetic energies up to the 16 times the ionization energy of the active shell, the ionization cross sections are obtained with the accuracy of DWBA and beyond this energy, the cross sections are calculated by multiplying the PWBA cross sections by an energy dependent scaling factor which is determined by a single fitted parameter. Although the results are based on both PWBA and DWBA, the ionization cross sections are more accurately calculated using DWBA near ionization threshold (region of interest in the experiment), and therefore we will describe the DWBA part of the formalism in the next section. Henceforth, we will call this model as DWBA theory and any other DWBA model will be properly differentiated.

2.4.1 Assumptions involved in DWBA theory

The interaction between the projectile and the target atom is considered as a weak perturbation, causing the transition of the atom from its ground state to the excited state which is in the energy continuum. Ionizing collision being the main interest in the study, transitions leading to the excitation of bound electrons are not considered. As the perturbation is considered weak, all the calculations are performed using the first-order perturbation theory. The model is based on the assumption that the wave functions of the two free electrons in the final state are uncorrelated i.e. post-

collision interaction between the ejected electron and scattered electron is completely ignored and free electron does not "feel" the electrostatic field of the other. Finally, the interaction occurs only between the projectile and one electron ("active electron") which gets ionized and the interaction is assumed to be purely Coulombic. The transverse interaction is disregarded and the corresponding interaction Hamiltonian $\mathcal{H}_{int}(0,1)$ between projectile (0) and active electron (1) becomes,

$$\mathcal{H}_{int}(0,1) = \mathcal{H}^{L}_{int}(0,1) = -\frac{e^2}{|\boldsymbol{r} - \boldsymbol{r}_0|} \tag{2.23}$$

where r and r_0 are the positions coordinates for the target electron and projectile respectively. Due to the assumption about transverse interaction, the model becomes semi-relativistic despite using the relativistic wave functions in the calculations. Still, it only affects the results for projectile energies much above the ionization threshold, while the results near ionization threshold remain perfectly valid.

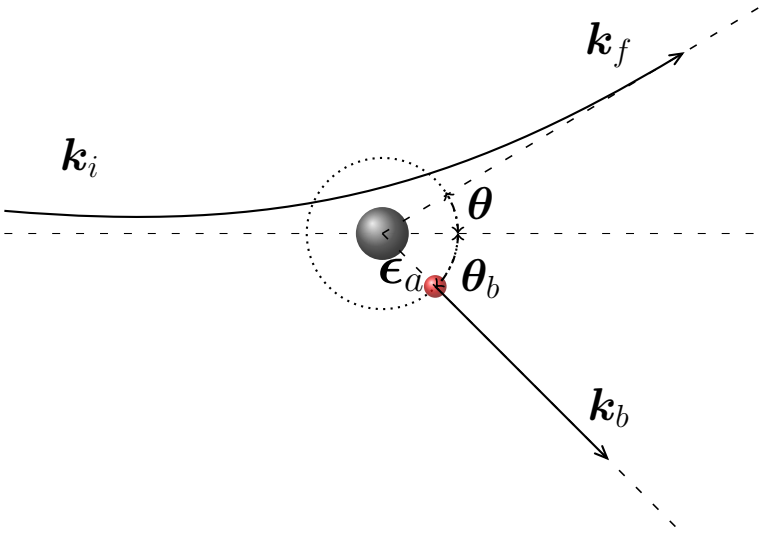

Figure 2.1: Collision Kinematics

The kinematics of the ionization process is shown in Fig (2.1). The projectile

with the initial velocity $\mathbf{v}_i$, linear momentum $\mathbf{p}_i = \hbar\mathbf{k}_i$, and kinetic energy $\boldsymbol{\epsilon}_i$ causes the ionization of atom by removing a bound electron of binding energy $\boldsymbol{\epsilon}_a$. After ionization, the projectile moves with velocity $\boldsymbol{v}_f$, momentum $\boldsymbol{p}_f = \hbar\boldsymbol{k}_f$ and energy $\boldsymbol{\epsilon}_f$. The ejected electron has the final kinetic energy $\boldsymbol{\epsilon}_b$ and momentum $\boldsymbol{p}_b = \hbar\boldsymbol{k}_b$.

2.4.2 Formalism:

In adopted DWBA formalism, the total Hamiltonian of the system is given as [96],

$$\mathcal{H}(0,1,\ldots,N) = \mathcal{H}_T(1,\ldots,N) + \mathcal{H}_P(0) + \mathcal{H}'(0,1,\ldots,N), \tag{2.24}$$

where, $\mathcal{H}_P(0)$ and $\mathcal{H}_T(1,\ldots,N)$ are the unperturbed Dirac Hamiltonians of the free projectile and the target atom containing N electrons respectively. $\mathcal{H}'$ is the perturbing Hamiltonian which includes the interaction of projectile with the electron cloud and nucleus of the target atom. The assumed form of $\mathcal{H}'$ is,

$$\mathcal{H}'(0,1,\ldots,N) = -e\phi_{nuc}(r_\circ) + \sum_{I=1}^{N}\mathcal{H}_{int}(0,I) - V_p(r_\circ) \tag{2.25}$$

where $-e\phi_{nuc}(r_\circ)$ is the term due to interaction of projectile with target nucleus. $V_p(r_\circ)$ is the distorting potential "felt" by the projectile electron and depends only on the co-ordinates of the projectile($r_\circ$). $V_p(r_\circ)$ is chosen such that $\mathcal{H}'$ can be treated as first-order perturbation. $\mathcal{H}'$ now can be considered as a weak perturbation which causes the transitions between eigenstates $\psi(0)\Psi(1,\ldots,N)$ of the "unperturbed" Hamiltonian $\mathcal{H}_T + \mathcal{H}_p + V_p$. The transition matrix elements are then given as,

$$\begin{aligned} T_{fi} &= \langle\psi_f(0)\Psi_b(1,\ldots,N)\,|\mathcal{H}'(0,1,\ldots,N)|\,\psi_i(0)\Psi_a(1,\ldots,N)\rangle \\ &= \langle\psi_f(0)\psi_b(1)\,|\mathcal{H}'(0,1)|\,\psi_i(0)\psi_a(1)\rangle \end{aligned} \tag{2.26}$$

To describe initial and final states of the target atom, a few important assumptions are made. Firstly, the mass of target atom is considered to be much larger than that of the electron so that the atom can be considered to be at rest before the collision.

Secondly, independent electron approximation is used, and accordingly, the states are given by the Slater determinants, built with one-electron orbitals which are the eigenfunctions of Dirac Hamiltonian of an electron moving in central potential $V_T(r)$. To evaluate T-matrix elements, the orbital wavefunctions for bound electrons are used which are solution of the one-electron Dirac equation,

$$\left[c\boldsymbol{\alpha}\cdot\boldsymbol{p}+(\beta-1)m_ec^2+V_T(r)\right]\psi_{n\kappa m}(r)=\boldsymbol{\epsilon}_{n\kappa}\psi_{n\kappa m}(r) \tag{2.27}$$

where, $\boldsymbol{\epsilon}_{n\kappa}$ is the energy eigenvalue of the bound electron exclusive of the rest mass energy. the bound electron wave-functions have the form [84],

$$\psi_{n\kappa m}(\boldsymbol{r})=\frac{1}{r}\begin{pmatrix}P_{nk}(r)\Omega_{\kappa m}(\hat{r})\\ \\ iQ_{nk}(r)\Omega_{-\kappa m}(\hat{r})\end{pmatrix} \tag{2.28}$$

where $P_{n\kappa}(r)$ and $Q_{n\kappa}(r)$ are the radial functions and $\Omega_{\kappa m}$ are the spherical spinors , n is the principal quantum number and κ is the relativistic angular momentum quantum number(see p.132 [97]), which is related to the orbital and total angular momentum quantum numbers, l and $j=l\pm\frac{1}{2}$ as,

$$\kappa=(l-j)(2j+1) \tag{2.29}$$

Free states for projectile and that of ejected electron are described by the distorted plane waves [98], for the corresponding central potential i.e. $V_p(r)$ or $V_T(r)$,

$$\begin{aligned}\psi^{\pm}_{\vec{k}\mu}(\boldsymbol{r})=\frac{1}{k}\sqrt{\frac{\epsilon+2m_ec^2}{\pi(\epsilon+m_ec^2)}}\sum_{\kappa,m}i^l\exp(\pm i\delta_{\epsilon\kappa})\\ \times\left\{\left[\Omega_{\kappa m(\hat{\boldsymbol{k}})}\right]^{\dagger}\chi_\mu\right\}\psi_{\epsilon\kappa m}(\boldsymbol{r})\end{aligned} \tag{2.30}$$

where $\mathbf{k}$ and ϵ are the wave number and the kinetic energy of the particle respectively, χ_μ are the Pauli spinors, and $\psi_{\epsilon\kappa m}(r)$ are spherical waves of the type as described in Eqn (2.28).

The target interaction potential V_T used in the Equation 2.27, is spherically averaged, Dirac-Fock-Slater (DFS) field, $V^{(DFS)}(r)$, which is completely determined

by the atomic electron density $\rho(r)$. The asymptotic behavior of the potential(i.e. $-(Z-N+1)e^2/r$ as $r \to \infty$) is correctly reproduced by following the ad hoc procedure suggested by Latter [99, 100].

$$\begin{aligned} V^{(DFS)}(r) &= -e\psi_{nuc}(r) - e\psi_{el}(r) + V_{ex}^{(Slater)}(r) \qquad \text{if} \quad r < r_{Latter}, \\ &= -(Z-N+1)e^2/r \qquad\qquad\qquad\qquad \text{if} \quad r > r_{Latter} \end{aligned} \tag{2.31}$$

where r_{Latter} is the outer root of the equation,

$$-e\psi_{nuc}(r) - e\psi_{el}(r) + V_{ex}^{(Slater)}(r) = -(Z-N+1)e^2/r \tag{2.32}$$

$-e\psi_{nuc}(r) = Ze/r$ is the electrostatic potential of the nucleus, and

$$\phi_{el}(r) = -\frac{e}{r}\int_0^r \rho(r')4\pi r'^2 dr' - e\int_r^\infty \rho(r')4\pi r' dr' \tag{2.33}$$

is the electrostatic potential of the atomic electron cloud. And

$$V_{ex}^{(Slater)}(r) = -e^2(3/\pi)^{1/3}\left[\rho(r)\right]^{1/3} \tag{2.34}$$

is the Slater's local approximation to the exchange interaction.

The differential cross section (DCS), differential in terms of energy loss W, for the excitation of the active electron from the orbital ψ_a to a free orbital ψ_b with positive energy ϵ_b is given by [85],

$$\frac{d\sigma_{ion}}{dW} = \frac{2\pi^4}{\hbar\nu_i}k_b k_f \frac{\boldsymbol{\epsilon}_f + m_e c^2}{c^2\hbar^2}\frac{\boldsymbol{\epsilon}_b + m_e c^2}{c^2\hbar^2}\int\int |T_{fi}|^2 \, d\hat{\boldsymbol{k}}_b d\hat{\boldsymbol{k}}_f. \tag{2.35}$$

The effect of electron exchange is consistently taken care by assuming that the projectile electron and the active electron both "feel" the same potential, i.e. in the case of electron $V_p = V_T = V^{(DFS)}(r)$. With this assumption, the projectile spherical waves-functions then become orthogonal to the orbitals of the target active electron. Accordingly, the effect of exchange is calculated by antisymmetrizing the initial and final states in the transition matrix elements. The transition matrix elements (2.26)

are replaced by

$$\begin{aligned} T_{fi}^{ex} = &\left\langle \psi^{(-)}_{k_f m_{Sf}}(0)\psi_{\epsilon_b\kappa_b m_b}(1)\left|\mathcal{H}_{int}(0,1)\right|\psi^{(+)}_{k_i m_{Si}}(0)\psi_{n_a\kappa_a m_a}(1)\right\rangle \\ &-\left\langle \psi^{(-)}_{k_f m_{Sf}}(1)\psi_{\epsilon_b\kappa_b m_b}(0)\left|\mathcal{H}_{int}(0,1)\right|\psi^{(+)}_{k_i m_{Si}}(1)\psi_{n_a\kappa_a m_a}(0)\right\rangle \end{aligned} \tag{2.36}$$

The final form the the differential cross sections after using the exchange T matrix and other terms is,

$$\begin{aligned} \frac{d\sigma}{dW} = &\frac{2e^4}{\hbar\nu_i}\frac{(\boldsymbol{\epsilon}_f+2m_ec^2)(\boldsymbol{\epsilon}_b+2m_ec^2)}{c^4\hbar^4k_i^2k_fk_b}\frac{\boldsymbol{\epsilon}_i+2m_ec^2}{\boldsymbol{\epsilon}_i+m_ec^2} \\ &\times\sum_{\kappa_i}\sum_{\kappa_f}\sum_{\kappa_b}\left[\sum_L\frac{1}{[L]}\left(X^{\epsilon_i\kappa_i,n_a\kappa_a}_{\epsilon_f\kappa_f,\epsilon_b\kappa_b,L}\right)^2+\sum_{L'}\frac{1}{[L']}\left(X^{\epsilon_i\kappa_i,n_a\kappa_a}_{\epsilon_b\kappa_b,\epsilon_f\kappa_f,L'}\right)^2\right. \\ &\left.-2\sum_L\sum_{L'}(-1)^{L+L'+1}\begin{Bmatrix} j_a & j_b & L \\ j_i & j_f & L'\end{Bmatrix}\times X^{\epsilon_i\kappa_i,n_a\kappa_a}_{\epsilon_f\kappa_f,\epsilon_b\kappa_b,L}X^{\epsilon_i\kappa_i,n_a\kappa_a}_{\epsilon_b\kappa_b,\epsilon_f\kappa_f,L'}\right] \end{aligned} \tag{2.37}$$

where, $X^{\epsilon_i\kappa_i,n_a\kappa_a}_{\epsilon_f\kappa_f,\epsilon_b\kappa_b,L}$ is given as,

$$\begin{aligned} X^{\epsilon_i\kappa_i,n_a\kappa_a}_{\epsilon_f\kappa_f,\epsilon_b\kappa_b,L} = &\nu(L,l_f,l_k)\nu(L,l_b,l_a)\sqrt{[j_a,j_b,j_i,j_f]} \\ &\times R^{\epsilon_i\kappa_i,n_a\kappa_a}_{\epsilon_f\kappa_f,\epsilon_b\kappa_b,L}\begin{pmatrix} L & j_i & j_f \\ 0 & \frac{1}{2} & -\frac{1}{2}\end{pmatrix}\begin{pmatrix} L & j_a & j_b \\ 0 & \frac{1}{2} & -\frac{1}{2}\end{pmatrix} \end{aligned} \tag{2.38}$$

Here, notations, $(:::)$ and $\{:::\}$ denote Wigner's $3j$ and $6j$ symbols respectively, $[p,q,...]$ is the product $(2p+1)\times(2q+1)...$, $\nu(l_1,l_2,l_3)=1$ when $l_1+l_2+l_3$ is even and equal to 0 otherwise. L is the index running from 0 to ∞ which originates in the expansion of the Coulomb potential($\equiv\frac{1}{|\boldsymbol{r}_0-\boldsymbol{r}_1|}$) in terms of spherical Racah tensors [101]. The term $R^{\epsilon_i\kappa_i,n_a\kappa_a}_{\epsilon_f\kappa_f,\epsilon_b\kappa_b,L}$ is the Slater integral [84]. The term $X^{\epsilon_i\kappa_i,n_a\kappa_a}_{\epsilon_b\kappa_b,\epsilon_f\kappa_f,L'}$ in Eqn (2.37) coming due to exchange is similar to Eqn (2.38) and can be obtained by interchanging the indicies ($b\leftrightarrow f$ and $L\leftrightarrow L'$).

The first and second terms in the large parentheses correspond to direct and exchange transitions, respectively. The third term results from the interference between the direct and exchange scattered waves. The total ionization cross section for particular sub-shell is then obtained by integrating the DCS over the allowed

energy transfer range i.e. from ionization threshold $|\epsilon_a|$ to the $W_{max} = (\epsilon_i + |\epsilon_a|)/2$. In the absence of exchange term, i.e. for positron the limit becomes $W_{max} = \epsilon_i$ and also the T matrix does not contain exchange term.

The ionization cross sections using above theory have been shown, to be in excellent agreement with the previous experimental data, especially for K-shell ionization [2]. Also in the case of L-shell ionization, DWBA based results are shown to reproduce the L x-ray production cross sections reasonably well [102]. Based on above formulas and PWBA calculations, a database of ionization cross sections of each subshell of K, L and M shells is generated using computer codes written in FORTRAN. This database, which we have used to compare our experimental data with, is within 1% uncertainty of the exact values of the DWBA cross sections obtained from above theory [16].

2.5 Predictor Formulas

The first classical theoretical study of electron impact ionization was presented by Thomson [79], in which he used nonrelativistic classical mechanics to calculate the differential cross section in terms of energy loss(W) of the projectile. In his calculations, Thomson assumed that the target electron is at rest and the projectile electron with non-relativistic kinetic energy $T = \frac{1}{2}m_e v^2$ approaches the target. The Thomson DCS is expressed as,

$$\frac{d\sigma^{Th}}{dW} = \frac{4\pi a_\circ^2 N R^2}{T}\frac{1}{W^2} \tag{2.39}$$

where, $a_\circ$ is the Bohr radius($a_\circ = 5.29 \times 10^{-11} m$), R is the Rydberg energy($R = 13.6$eV) and $N = 2j+1$ is the total number of electrons in the particular orbital with angular momentum j. Thomson DCS is identical to the well-known Rutherford DCS for the scattering of two electrons in the center-of-mass frame. In fact, Eqn (2.39)

can be obtained by performing the transformation from center-of-mass frame to the laboratory frame, where an electron is at rest. In the collision with the bound electron, ionization can occur only if the kinetic energy of the projectile is more than the binding energy (B) of the target electron. Therefore Thomson DCS is zero if $T < B$. The total ionization cross sections for ionization of a particular shell with binding energy B is obtained by integrating the Eqn (2.39) from B to the incident energy T and final formula is given as,

$$\sigma_{Th} = \frac{4\pi a_\circ^2 N R^2}{T} \frac{1}{B} \left(1 - \frac{1}{I_\circ}\right) \tag{2.40}$$

here, $I_\circ \equiv T/B$.

As described earlier, Rutherford scattering cross sections are the same whether it is calculated using quantum or classical theory. Exploiting this universal validity of Rutherford DCS, Mott modified the Thomson DCS formula so as to incorporate the electron exchange effect occurring due to indistinguishability of electrons in the output channel [103]. The Mott DCS is given as,

$$\frac{d\sigma^{Mott}}{dW} = \frac{4\pi a_\circ^2 N R^2}{T} \left[\frac{1}{W^2} + \frac{1}{(T-W)^2} - \frac{\Phi}{W(T-W)}\right] \tag{2.41}$$

where, Φ is the function of T and B whose value lies in an interval [0,1] and is given as,

$$\Phi = \cos\left[\sqrt{\left(\frac{R}{T+B}\right)} \ln\left(\frac{T}{B}\right)\right] \tag{2.42}$$

In the expression (2.41) of Mott's DCS, the first term is for the direct collision with energy loss W, the second term is due to exchange where the energy loss of projectile is $T-W$, and the last term accounts for the interference term. Mott's DCS is symmetric under the exchange of terms W and $T-W$, reflecting the indistinguishability of the electrons in outer channel. The relativistic version of Mott's DCS was obtained by

Møller [12] which is given as,

$$\frac{d\sigma^{Møller}}{dW} = \frac{4\pi a_\circ^2 NR^2}{T}\left\{\frac{1}{W^2} + \frac{1}{(T-W)^2} - \frac{1-b_\circ}{W(T-W)} + \frac{b_\circ}{T^2}\right\} \tag{2.43}$$

where,

$$b_\circ = \left(\frac{T}{T + m_e c^2}\right) \tag{2.44}$$

It should be noted that in all three DCS i.e. of Thomson, Mott, and Møller it is assumed that the target electron is at rest and the projectile with kinetic energy T is moving towards the target electron.

Although one can regard the Mott's DCS itself as a formula which describes a binary collision, i.e. a billiard ball like collision between two free electrons, but in literature, it is more common to call the theory binary-encounter theory if some momentum is associated with the target electron while calculating the DCS. Assuming that the target has average kinetic energy $U \equiv \boldsymbol{p}_{avg.}^2/2m$, the classical binary encounter DCS, can be written as,

$$\begin{aligned}\frac{d\sigma^{CBE}}{dW} &= \frac{4\pi a_\circ^2 NR^2}{T}\left(\frac{1}{W^2} + \frac{4U}{3W^3}\right) \qquad \text{for } W \le T-U \\ &= \frac{4\pi a_\circ^2 NR^2}{T}\left(\frac{1}{W^2} + \frac{4(T-W)}{3W^3}\right)\left(\frac{T-W}{U}\right)^{\frac{1}{2}} \qquad \text{for } W \ge T-U\end{aligned} \tag{2.45}$$

In attempt to improve the Thomson's theory and get the ionization cross sections having energy dependence closer to that predicted by Quantum model of Bethe, binary encounter model was proposed by Gryzinski [104–106] in which he assumed that the atomic electron moves with an isotropic velocity distribution,

$$f(v) = (\bar{v}/v)^3 \exp -(v/\bar{v}) \tag{2.46}$$

where symbols have their usual meaning.

Using, this velocity distribution, Gryzinski obtained the following expression for

the total ionization cross sections for particular subshell.

$$\sigma_i^{Gr} = \frac{4\pi a_\circ^2 N R^2}{T}\frac{1}{B}\frac{1}{I_o}\left(\frac{I_o-1}{I_o+1}\right)^{3/2} \times \left[1+\frac{2}{3}\left(1-\frac{1}{2I_o}\right)\ln(2.7+\sqrt{I_o-1})\right] \tag{2.47}$$

where, $I_\circ \equiv T/B$.

Although Eqn (2.46) is not a realistic distribution but merely an *ad hoc* arrangement to get better ionization cross sections, Eqn (2.47) provide improvement over the Thomson's formula and has been used as a convenient semi-empirical formula to obtain fast estimates of the ionization cross sections [1, 2, 59].

Following the work of Gryzinsky, Vriens proposed that the target electron should be assigned the momentum distribution which represents its orbital motion [82, 107]. The momentum distribution is generally derived from the bound electron wave function. Accordingly the average kinetic energy is obtained as,

$$U \equiv \frac{\langle \mathbf{p^2} \rangle}{2m} \tag{2.48}$$

where $\boldsymbol{p}$ is the momentum operator in a given sub-shell. The quantum mechanical solution of above equation can be obtained analytically and the symmetric form of the DCS proposed by Vriens [82] can be presented as,

$$\frac{d\sigma^{BE}}{dW} = \frac{4\pi a_\circ^2 N R^2}{T+U+B}\left\{\frac{1}{E^2} - \frac{\Phi}{E(T-W)} + \frac{1}{(T-W)^2} + \frac{4U}{3}\left[\frac{1}{E^3}+\frac{1}{(T-W)^3}\right]\right\} \tag{2.49}$$

where $E = T + W$ and Φ is as defined in Eqn 2.42.

Although the binary-encounter theory proposed by Vriens [82], augments the Mott formula by assigning a velocity or momentum distribution to the target electrons, it still lacks the dipole contribution. Due to this oversimplification, it leads to the incorrect cross sections at high incident energies, where dipole interactions are

dominant [108]. In an attempt to combine dipole interactions with Binary-encounter formula, Kim and Rudd proposed a model called Binary-encounter Dipole model [108]. In BED model, the non-relativistic energy loss DCS is expressed as a combination of the DCS obtained from binary collision formalism and from the dipole approximation. The BED model was constrained to reproduce the high energy asymptotic limit given by Bethe theory. Using Equation 2.49 and setting the value of Φ equal to 1, the obtained formula for the DCS of BED is,

$$\begin{aligned}\frac{d\sigma^{BED}}{dW} = \frac{S}{B(t+u+1)}\Bigg\{&\frac{(N_i/N)-2}{t+1}\left(\frac{1}{(w+1)}+\frac{1}{(t-w)}\right)\\&+[2-(N_i/N)]\left(\frac{1}{(w+1)^2}+\frac{1}{(t-w)^2}\right)+\frac{\ln t}{N(w+1)}\frac{df(w)}{dw}\Bigg\}\end{aligned} \tag{2.50}$$

where,

$$\begin{aligned} t &= T/B,\\ w &= W/B,\\ u &= U/B,\\ S &= 4\pi a_\circ^2 N(R/B)^2 \qquad \text{and}\\ N_i &\equiv \int_0^\infty \frac{df(w)}{dw}dw. \end{aligned} \tag{2.51}$$

The BED model does not depend on any empirical or fitted parameters, but it requires accurate knowledge of experimental or theoretical data for various quantities. To obtain ionization cross sections from BED model, values of binding energy (B), average kinetic energy of orbital electron(U), number of electrons in the orbital (N) and the differential oscillator strengths ($df(w)/dw$) are needed for each sub-shell of the target atom. Out of needed quantities, B and N are readily available from various data tables[109], while U can be calculated from electronics structure codes such as those developed by Desclaux and Indelicato [110, 111]. Differential oscillator strengths are generally harder to obtain for all the elements, although total and partial values of $df(w)/dw$ is available for many atoms in the literature.

Although the BED model is substantially simpler to use than most *ab initio* theories for electron-impact ionization, it is often difficult to get the differential oscillator strengths, particularly for each subshells. For such cases, Kim and Rudd simplified the BED formula, and accordingly they replaced differential oscillator strengths $df(w)/dw$ in Eqn 2.50 with the simple function. This modified model is termed as binary-encounter-Bethe (BEB) model and the corresponding total ionization cross sections for a given sub-shell is given as [108],

$$\sigma_{BEB} = \frac{S}{t+u+1}\left\{\frac{1}{2}\left(1-\frac{1}{t^2}\right)\ln t + \left[\left(1-\frac{1}{t}\right) - \frac{\ln t}{t+1}\right]\right\} \tag{2.52}$$

Kim and Rudd also formulated the relativistic version for both BED and BEB models [108, 112]. BEB model of Kim and Rudd provides cross sections that are very reliable from the ionization threshold to several keV, specifically for the low Z elements. [113–116]

2.5.1 Modified Relativistic Binary Encounter Bethe Model

The term $1/(T+U+B)$ arriving in the final expression of BEB DCS, is the *ad hoc* term, added following the so-called "impulse approximation". The original qualitative justification for it was that the "effective" incident energy seen by the incoming electron is $T+U$ of the target electron. This term, which is called as scaling factor or focusing factor, reflects the scaling method used to scale first-order PWBA electron-impact excitation and ionization cross sections [117]. The resultant effect due to this scaling term is the reduction in the calculated cross sections and is readily accepted because most collision theories overestimate the cross sections especially near the ionization threshold. It is essential to point out here that much of the success of the BEB model for neutral low Z elements can be attributed to this scaling term.

Following the work of Kim [117], Guerra et al. [3] suggested different scaling

method for the BEB/RBEB models. The modified model is simply named as modified binary encounter Bethe model(MBEB) or modified relativistic binary encounter Bethe model(MRBEB) when relativistic theory RBEB is used. In their model, Guerra et al. adopted $1/T+X$ as the scaling factor, where X is the modified term replacing $T+U$, namely X type scaling [117]. Taking into account that the factor X is related to the shielding of nuclear charge by bound electrons of the target atom, and the binding energy of K-shell electrons in neutral atoms scales as $0.4240Z^{2.1822}$ [118], Guerra et al., assumed the quadratic form for X and X is set equal to the hydrogenic energy levels expression as first approximation. To account for the energy change of the incident electron while penetrating through the electron cloud, X is further modified accordingly, and the form consisting of a linear combination of corresponding sub-shell hydrogen like energy levels was adopted. In atomic units $X_{nlj}(Z)$ is given as,

$$X_{nlj}(Z) = a\frac{Z^2_{\text{eff},nlj}}{2n^2} + b\frac{Z^2_{\text{eff},n'l'j'}}{2n'^2} \tag{2.53}$$

where a and b are constants and $n'l'j'$ stands for the next subshell after the subshell nlj. With this scaling factor the final ionization cross sections of particular sub-shell using the modified BEB theory is given as,

$$\sigma_{MBEB} = \frac{S}{t+\chi_{nlj}}\left\{\frac{1}{2}\left(1-\frac{1}{t^2}\right)\ln t + \left[\left(1-\frac{1}{t}\right) - \frac{\ln t}{t+1}\right]\right\} \tag{2.54}$$

where,$\chi_{nlj} = (X_{nlj}/B)2R$ and the relativistic counterpart is given as,

$$\begin{aligned}\sigma_{\text{MRBEB},n\ell jLS} \;=\; & \frac{4\pi a_0^2\alpha^4 N_{n\ell j}}{\left(\beta_t^2+\chi_{n\ell j}\beta_b^2\right)2b'}\left\{\frac{1}{2}\left[\ln\left(\frac{\beta_t^2}{1-\beta_t^2}\right) - \beta_t^2 - \ln\left(2b'\right)\right]\times\right. \\ & \times\left(1-\frac{1}{t^2}\right) + 1 - \frac{1}{t} - \frac{\ln t}{t+1}\frac{1+2t'}{\left(1+t'/2\right)^2} + \\ & \left. + \frac{b'^2}{\left(1+t'/2\right)^2}\frac{t-1}{2}\right\},\end{aligned} \tag{2.55}$$

where

$$\begin{aligned} \beta_t^2 &= 1 - \frac{1}{(1+t')^2} & t' &= T/mc^2, \\ \beta_b^2 &= 1 - \frac{1}{(1+b')^2} & b' &= B/mc^2, \\ t &= T/B & \chi_{n\ell j} &= (X_{n\ell j}/B)2R. \end{aligned} \tag{2.56}$$

It can be seen that contrary to the BEB/RBEB models, MBEB/MRBEB models need only one parameter to calculate the ionization cross sections, i.e. binding energy of inner shell electron (B), while the BEB/RBEB needs two input parameters, B, and U. For the binding energies of inner-shell electrons, one can use experimental values [119] or theoretical binding energies from Dirac-Fock wave functions that are reliable to 1% or better. This model of MRBEB produces reliable cross sections between the threshold and the ionization peak without using any shell-dependent parameters specially for K shell ionization [3, 120].

CHAPTER 3

Experimental Details

3.1 Brief Overiew

To measure the electron impact ionization cross sections of high Z elements, an electron beam of fixed and known energy and current is directed through a thin solid target under high vacuum. The incident electron beam interacts with the atoms in target and causes excitation or ionization. As discussed in Chapter 1, these atoms relax to the ground state by emission of either Auger electrons or X-rays and under the ideal condition when no multiple ionization occurs, the relation between X-ray yield and X-ray production cross section is given by Eqn.3.1

$$\sigma_i(E) = \frac{N_X \cdot A}{\epsilon(E') \cdot t \cdot N_e \cdot N_A \cdot k(E)} \tag{3.1}$$

where, $\sigma_i(E)$ is the production cross section (cm^2) of L_i line at electron energy E, N_X is the total X-rays yield for the particular line, A is the atomic mass of the target, $\epsilon(E')$ is the effective efficiency of detector at photon energy E', t is the mass thickness of target(g/cm^2), N_e is the number of electrons, and N_A is the Avogadro number, $k(E)$ is the correction factor in case of Aluminum backed targets, details of which are provided in Chapter 4.

The rest of this chapter describes the experimental arrangement, details of measurement and data analysis procedure followed to obtain various quantities needed in Eqn 3.1 to get the production cross sections.

3.2 Experimental Setup

In this thesis work, an experimental setup to study the electron impact ionization, in the energy range of $0 - 50$ keV is constructed. The experimental setup is basically the energy dispersive X-ray spectrometer. The schematic of the experimental arrangement and the actual experimental setup is shown in Figures 3.1a and 3.1b respectively.

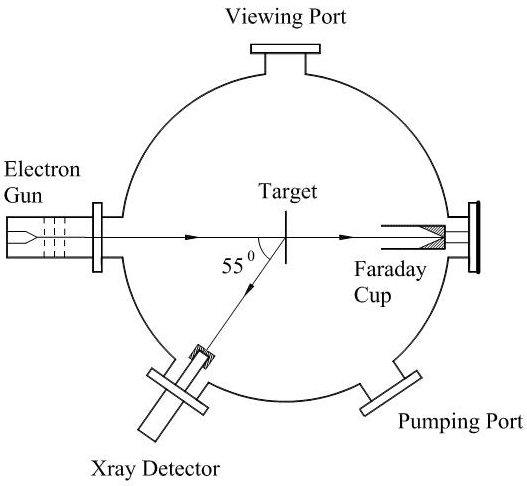

(a) Schematic of Experimental Chamber

(b) Photograph of Experimental setup while alignment

Figure 3.1: Experimental Setup

The setup consists of an experimental housing chamber, an electron gun, X-ray detectors and measurement electronics. The experimental housing is a cylindrical vacuum chamber made of stainless steel (SS-304), wherein the complete experimental setup is assembled. The chamber has the cylindrical shell with inner diameter 450 mm, height 510 mm and thickness 5mm, which is sandwiched between two thick SS

plates of diameter 525 mm and thickness 25 mm. Top and bottom plates are vacuum sealed using high purity Aluminum wire to achieve high vacuum. On the cylindrical wall of vacuum chamber, there are four DN-100CF ports in coplanar configuration to assemble various apparatus and one big DN-200 CF port for the evacuation of chamber. The DN-200 CF evacuation port is vacuum welded to the chamber wall through a right angle bend, made of SS-304 cylindrical pipe of 206 mm outer diameter. A turbomolecular pump is connected to this port through a DN-200CF bellow sealed gate valve. There are 3 DN-40CF ports on the top and bottom plates, two of them are on the center of each plane and the third is at the distance of 50 cm from center of bottom plate.

Out of four DN- 100CF ports two are positioned 180° apart. The electron gun is placed on one of these ports and Faraday cup on the port opposite to it. X-ray detector is placed on the third port which is at specifically chosen angle of 55° with respect to the electron gun port. The fourth DN-100CF port is used as a viewing window while positioning the target at the beam position and ensuring the shape and size of the electron beam. The electron gun, mountable through a DN-100 CF port, is directly fixed to the electron gun port on the chamber with a manually operated DN-100 CF gate valve mounted in between. Gate valve is used to keep the electron gun in vacuum when chamber is brought to air. X-ray detector and Faraday cup are attached to the blank 100CF flanges using proper mounting, which are then attached to the chamber. X-ray detector is mounted on an Aluminum plate, for the efficient heat dissipation through thermal conduction as shown in Figure 3.2a. The center of the detector crystal was aligned with the center of the flange using a lathe machine. Electrical connection to the detector for biasing voltage and power supply is provided by the 9-pin D type electrical feed-through, while signal is taken out with co-axial LEMO feed-through. The Faraday cup is mounted on the mica sheet which is supported by four Aluminum studs as shown in Figure 3.2b. Mica sheet is

used to electrically isolate the Faraday cup from the flange on which it is mounted. Electrical connection to the Faraday cup is provided by one of the four co-axial LEMO feed-through mounted on the Faraday cup flange.

The electron gun and Faraday cup are aligned using a laser beam such that the axis defined by the two elements, passes through the chamber center. The center of chamber is obtained by intersection of laser beam passing through the center of diametrically opposite DN-100 CF ports and a thin thread through center of the DN 40CF ports, mounted at the center of the top and the bottom cover flanges of the chamber. By reflecting the laser beam using a very thin mirror attached to the thread at center of chamber, it is ensured that the detector crystal is also in the central plane of the chamber. The targets are placed at the center of the chamber using target ladder, attached to the SS rod. The SS rod passes through the Wilson seal attached at the top port. Wilson seal is the mechanical feed- through, which provides a mechanism to move the target in and out of the beam path. The Wilson seal provides room for 100 mm vertical travel, enabling 5 target ladder positions of $12 - 15$ mm diameter each to be placed at the center.

3.2.1 Vacuum System

While performing the experiment with electrons as projectile, it is necessary to house the apparatus in a high vacuum. To minimize the effect of background gases, it is essential that the chamber pressure must be low enough, so that the mean free path of the projectile electrons is greater than the length scale of the chamber. To fulfill these requirements, the experimental chamber is evacuated and brought down to the very high vacuum of the order of 10^{-7} mbar using the turbo molecular pump (Adixen Inc, Capacity-900L/s). The turbo pump is backed by a rotary vane pump (Edwards Vacuum Inc. capacity-9L/s), which is also used as a roughing pump though

(a) X-ray Detector (b) Faraday Cup(with wide opening)

Figure 3.2: Photograph of various instruments used in the experimental set up.

separate line. To absorb the oil vapors, a molecular sieve is kept at the input port of mechanical pump. Vacuum inside the chamber was measured using the Perani cum cold cathode gauge (Adixen Inc.) mounted on the DN 40CF port at the bottom plate of vacuum chamber.

3.3 Electron Beam Details

3.3.1 Electron Beam Generation

To generate the steady electron beam of fixed energy, commercially obtained electron gun was used (Kimball Physics Inc.) in the setup. The schematic of electron gun is as shown in Fig 3.3. Electron gun cathode is made of Tantalum and is in the shape of disk. Tantalum emitter is directly heated by an isolated voltage source referenced to the energy supply which is a negative high voltage supply (0 to 60 kV) and is referenced to ground. The cathode is heated by applying voltage of 1.3 to 1.5 V

which makes current of 1.1 A to 1.3 A to flow through the cathode. After the cathode, there is first grid element in the gun which is referenced to the high voltage supply and is used to pulse the electron beam. In the current study, no pulsing was needed. After the grid electrode, there is first anode, which is used to extract the electron beam and is biased with positive voltage of upto 1 kV with respect to the cathode. After the 1^{st} anode, there is one more electrode called Wehnelt or variable grid element. The 1^{st} anode and the variable grid are used to extract the maximum current, and also to focus the emerging electron beam. Finally after the Wehnelt grid/cylinder, there is the grounded anode and the final energy of the electrons emitted from the gun, is the difference of potential between high voltage applied to the Ta cathode and the grounded anode. After the main electron gun assembly, there is focusing lens assembly to vary the beam size. The electron beam is stirred by quadrapole magnetic stirrers built in-house. The magnetic stirrers are placed outside the vacuum chamber, at the beam exit port of the electron gun. The beam can be deflected by about $1-2$ cm, horizontally and vertically at the target position, by applying the current of up to 500 mA.

The electron gun is capable of delivering $0-50$ keV electron beam of up to $100\,\mu$A current. Using the built in magnetic lens, the electron beam from the gun can be focused, to the spot size of $0.5-10$ mm on the target position at the maximum distance of 600 mm from the beam exit port of electron gun. The electron beam is focused at the center of chamber, by viewing the beam spot with the help of a phosphor screen. The electron beam current on target ladder is reduced to zero at the same time by placing blank frame at the target position. The electron beam has energy spread of < 1 eV, which arises due to heating of the cathode.

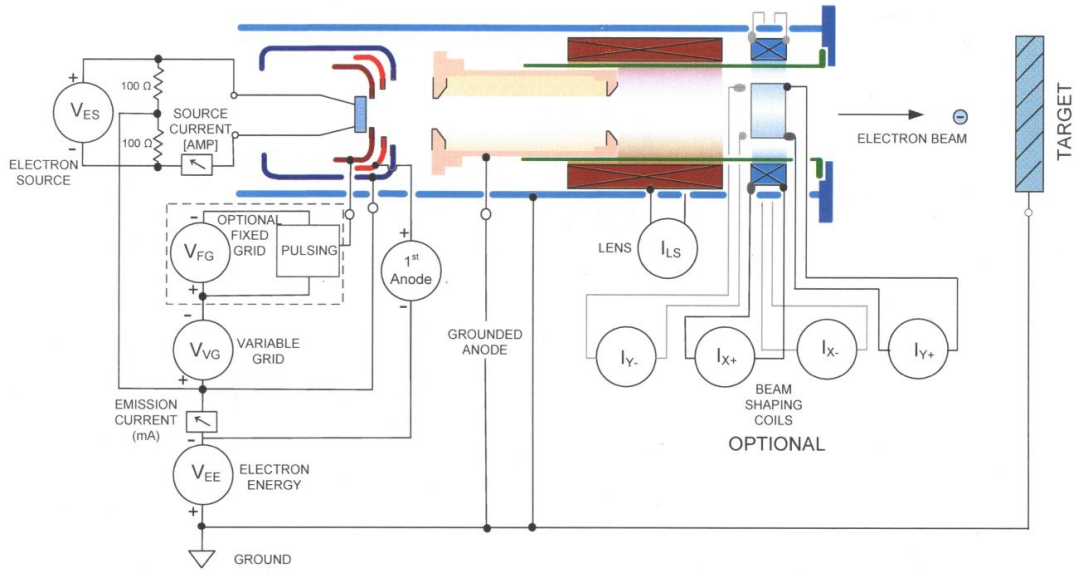

Figure 3.3: Schematic diagram of the 50 keV electron gun system.

3.3.2 Beam Current Measurement.

In the electron impact experiments performed to obtain the absolute cross sections, it is necessary to measure the electron current impinged on targets with high accuracy. This requirement is fulfilled by (i) efficient collection of projectile electrons after passing through target and (ii) accurately measuring it using sensitive electro-meter. As the incident currents are generally of the order of nano or pico Ampere, highly sensitive electro-meter is needed to measure the electron flux.

To know the total beam flux, the electron current was measured both at target ladder and the Faraday cup (FC) placed after the target. To facilitate the beam current measurement, target ladder was isolated from the chamber and was biased to +105 V. Since the targets used in our experiments are not very thin (a few tens of nanometers thickness), the electron beam gets diffused while passing through the target. This results in a divergent outgoing beam. Due to this reason, either the

Faraday cup has to be made with wide opening or it must be brought very close to the target. The problem of making a Faraday cup with wide angular opening is that along with collecting the in-beam electrons that interact with the target materials, it may collect the stray electrons that have bypassed the target and reached the FC. To avoid this difficulty, the Faraday cup is made with smaller opening of 20mm diameter and brought closer to the interaction region. The length of Faraday cup is 150mm which ensures that none of the electrons escape the Faraday cup after hitting the FC surface [121]. To reduce the direct reflection of electrons from the Faraday cup surface the rear end of Faraday cup is made conical so that the least number of electrons escape from it. Due to wide solid angle of emergence of outgoing electron beam, the Faraday cup is placed at distance of 50 mm from the target position. However even after bringing the Faraday cup close to the targets ($5-10$mm), the total beam current, which is the sum of current measured at the Faraday cup and that at the target ladder, was not equal to the beam current collected by Faraday cup when the target was out of the beam. This deficiency in the observed beam current is due to the fact that the electrons gets backscattered from the solid targets, thereby reducing the measured beam current. This deficiency can be corrected using the backscattering factor, which is defined as the ratio of the number of electrons scattered at angles $\geq 90^{\circ}$ to that scattered from the target at all angles. Using backscattering factor, one can get the actual number of incident electrons, but this data is not always available for the required thickness, and hence one has to rely on estimated values, which may vary by $10-20\%$ [6]. To avoid the backscattering factor correction, the total number of electrons collected by FC during a given time was measured with and without the target placed in its position. The correction factor r_c defined as,

$$r_c = \frac{Total\ charge\ collected\ by\ FC\ with\ target}{Total\ charge\ collected\ by\ FC\ without\ target} \tag{3.2}$$

was obtained and used to correct the measured charge in the experiment. To get the actual number of electrons in the beam (N_e in Eqn. 3.1), the total integrated charge

during the data collection period was divided by the factor r_c. The ratio(r_c) is found to be constant over the time frame of experiment (i.e, $10 - 15$ hours) and also it is independent of the incident beam current. Figure 3.4 shows the factor r_c for Gold and Lead targets at several incident beam energies.

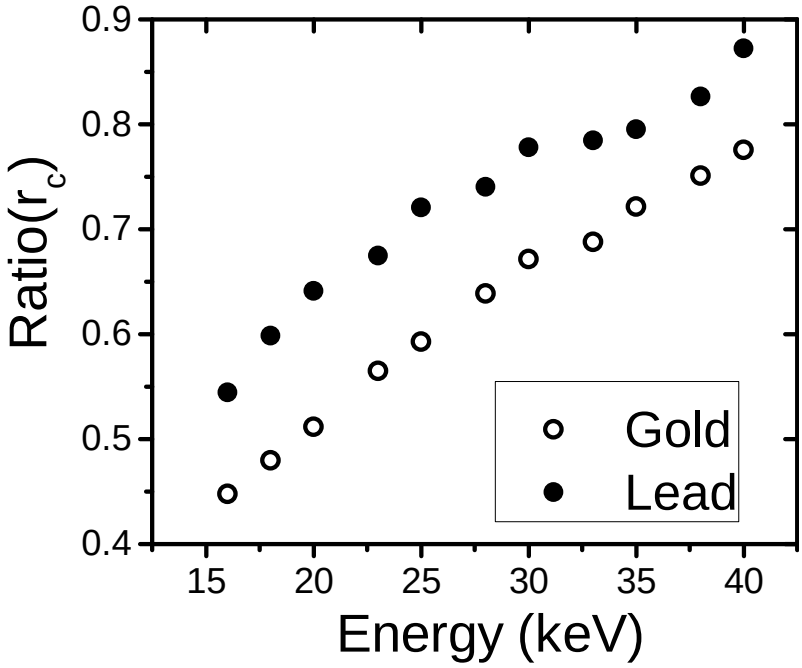

Figure 3.4: Ratio (r_c) of measured beam current at the Faraday cup with and without target in its position[Thicknesses: Au-156 $\mu g/cm^2$, Pb-82 $\mu g/cm^2$].

3.4 Targets

The target thickness is yet another important parameter in the electron impact ionization experiments. In fact, it is one of the two factors which decide the overall uncertainty of the obtained experimental results. As the elements used in this work are mainly solid, the targets used are in the form of thin film. The thin film targets are attached on Aluminum frames which are mounted on the target ladder by small screws. Aluminum is chosen as a material to be used for the frame because, if beam halo hits the frame, the X-rays emitted from it should be non-overlapping with most of the characteristic L X-ray lines to be studied. Target ladder has 5 mounting

positions, and the desired target can be placed at the central plane with target center coinciding on the electron beam axis by adjusting the position of the ladder. Out of these 5 mounting positions on the ladder, two positions are occupied by (1) a thin silver doped zinc sulfide coated phosphor screen and (2) a blank target frame leaving three positions available to mount the targets to be studied.

3.4.1 Target Preparation

While preparing thin film target, considerations have to be given while choosing the target thickness. The targets, being very fragile and thin, special care is needed for preparation and handling of the targets. The targets are expected to be thin so as to achieve single collision condition and minimize multiple scattering on the target, but they should also be thick enough to give moderate count rates. In general, single collision condition is satisfied if $n\sigma < 1$ where, n is the number of target atoms per cm^2 and σ is the cross section.

For our experiments, the targets are made by mainly two different preparation methods i.e. (i) Electron Beam Vapor Deposition and (ii) Electro-Deposition. Using both the methods, uniform thin films of required thicknesses can be obtained.

Electron Beam Vapor Deposition (EBVD)

In EBVD, electron beam of 4.76 keV energy and current of 200 mA is hit on the target material kept in a ceramic crucible under high vacuum ($\sim 10^{-6}$ mbar). Due to high current of energetic electrons, intense local heat is generated which melts the material. This heated material then evaporates into the surrounding volume enclosed by the chamber, and eventually gets deposited on the glass slides kept inside the vacuum chamber.

The glass slides are first prepared in vacuum by depositing a thin film of water

soluble salt (known as parting agent) on the glass substrate. The main material is then deposited by electron beam evaporation. A quartz crystal based thickness monitor is placed near the glass slides inside the deposition chamber to monitor the growth of thin film on the substrate. Deposition is stopped once the desired thickness is reached. The slides are then allowed to cool down to room temperature before the system is brought to air. Once the deposition process is complete, the glass slide is dipped gently in the water allowing salt to dissolve slowly. When the entire layer of salt is dissolved in the water, the target film is released from the slide and floats on the water. The film is then lifted on the Al frames. Some of the targets have the carbon backing. For the targets having carbon backing first C targets are made as per method described above, then the Al frame with C targets are put in the EBVD chamber and the main target is then deposited as usual. Using this method targets of Au, Bi, Pb and Cu were made.

Electro-Deposition

Targets of Uranium and Thorium were prepared by electro-deposition (ED) method. Electrolytic solution of Thorium/Uranium nitrate in 2-propanol solvent is prepared for making these targets. ED is then done on 200 $\mu g/cm^2$ thick Aluminum foil(99.99 % purity) used as cathode. The target formed on the foil is in the form of oxide i.e. ThO_2 for Th. The thickness of target is monitored by measuring the electrode current and the duration of electro-deposition.

3.4.2 Thickness Measurement.

Although thickness of the targets were monitored and crudely measured during their preparation, it is important to know the thickness as accurately and precisely as possible for the absolute cross section measurements. Although the best method to measure target thickness is to use Rutherford Backscattering (RBS) technique, it

was not possible to transport such fragile targets to the accelerator facility and back without breaking them. An alternative method, though less accurate than RBS, using Alpha Energy loss spectroscopy is used. The technique is described in the following sub-section.

Alpha Energy loss spectroscopy.

A separate setup was designed for target thickness measurement, as shown in Figures 3.5 and 3.6 . The setup consist of a vacuum chamber in which, a mixed three line alpha source(^{239}Pu, ^{241}Am, ^{244}Cm), the target and a silicon surface barrier detector are placed along a straight line. The pressure of the order of 10^{-2} mbar or better is maintained inside chamber to avoid energy loss of alpha particles. Target mounting arrangement is the same as that of main experimental chamber i.e. targets were mounted on target ladder which was attached to the Wilson seal arrangement to move the target in or out of alpha particle path. Target ladder has three mounting position out of which, one is kept blank to calibrate the detector, while the other two positions are kept free for mounting targets. The surface barrier detector has active surface area of 300 mm^2 and needs bias of $+30 - 40$V to operate in fully depleted condition. Due to absence of sealing window in front of detector, surface barrier detector is very sensitive to light, hence care has to be taken in order to keep the detector in a light-tight enclosure when the bias is applied to it.

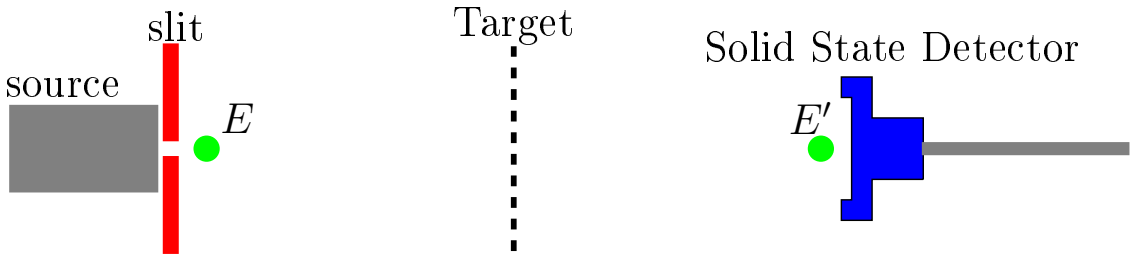

Figure 3.5: Thickness Measurement Study

In the process of measuring thickness by alpha energy loss, the alpha energy

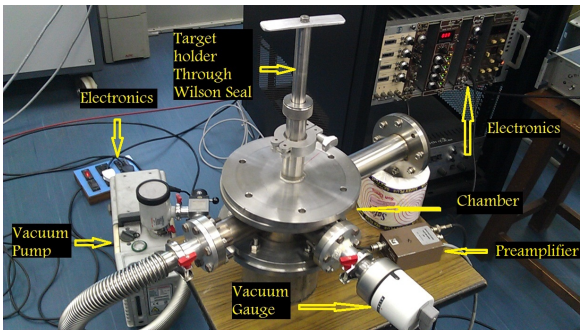

Figure 3.6: Alpha energy loss

spectra of the source mentioned, is recorded twice, i.e. with and without target in the alpha particle path, as shown in Figure 3.7a. Both the spectra are recorded in the single run(i.e. without changing the bias voltage and moving targets in and out of beam path), which is essential for keeping the energy calibration same in both the spectra.

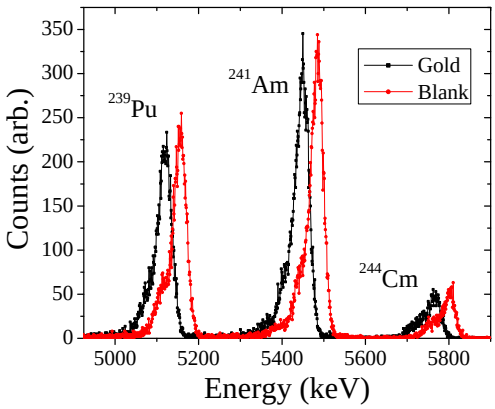

(a) Alpha particle energy spectra, obtained from 3-line Alpha source, with and without the Gold target in beam path

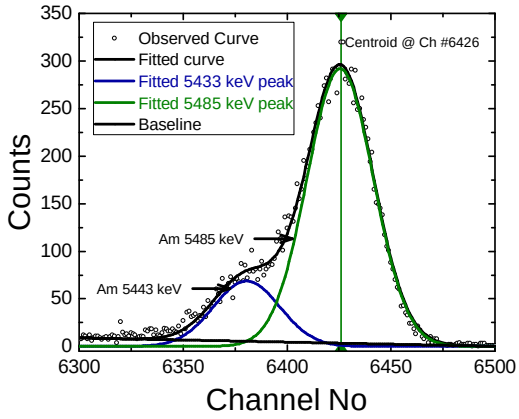

(b) De-convoluted plot of ^{241}Am line for energy calibration.

Figure 3.7: Thickness Measurements in Au.

As the targets are very thin, α-particles do not loose its total energy and stop inside the target material, but cross the target with the fractional loss in its kinetic energy. This energy loss ΔE is proportional to the target thickness and in turn, it is

used to obtained the thickness(Δt), by using relation

$$\Delta t = \frac{\Delta E}{dE/dt} \tag{3.3}$$

where, dE/dt is the energy loss per unit length of alpha particle in given material, generally referred to as, stopping power. The value of stopping power are obtained from the program SRIM [5].

To obtain the energy loss(ΔE), first the energy calibration of the detector is done using the main peaks of the three line alpha source with no target in alpha particle path. As each peak contains two or more major transitions, each peak is fitted with two separate Gaussian. In the process of fitting, amplitudes of Gaussians were fixed according to suggested branching ratios in literature, while common width(FWHM) of all the peaks and positions were free parameter for fitting. The Figure 3.7b shows the fitted spectrum of ^{241}Am.

The transition energies and branching ratios are obtained from NuDAT database of National Nuclear Data Center [122–124]. The Table 3.1, shows the branching ratios which are used in obtaining the position of each transition.

Element	Energy	Branching Ratio
^{239}Pu	5156	70.77
	5144	17.11
	5105	11.94
^{241}Am	5485	84.50
	5443	13.10
^{244}Cm	5804	76.9
	5762	23.1

Table 3.1: Energy and branching ratio of 3-line alpha source

The centroid position of each fitted peak in blank spectrum is then used to calibrate both the spectra and obtain ΔE which is then used to obtain the thickness

of targets. In case of targets backed by another foil, first the thickness of backing is measured by the same process described above, and then the thickness of main target is measured. The Table 3.2, lists thicknesses of all the targets used in this study.

Target	Thickness($\mu g/cm^2$)
Cu	42.0(2.1)
Au	156.0(7.5)
Pb	82.0(4.2)
Bi	140.5(6.4)
Th	78.1(3.8)
U	78.1(3.8)
Al	200(11.8)

Table 3.2: Thicknesses of Targets

3.5 X-Ray Detection.

X-ray detection is done using two types of detectors i.e. Si-PIN diode and Silicon Drift Detector (SDD) detector (both from Amptek. Inc). The usable energy range of detection for both of these detectors is from 1 keV to 60 keV. The resolution and efficiency of the detectors are obtain for the energy range of interest i.e, $5 - 25$ keV. In both the detectors, the detector system consists of a Peltier cooled active element (Si-PIN or SD) and high gain low noise preamplifier. The detector crystal is sealed in the unit with thin Be window. The various parameters of both the detector are as follows,

The detector head (unit consisting detector crystal) is covered with the graded collimator, which is made up of layers of different materials. The collimator has four different layers made of elements with decreasing atomic number (Z) from the outer surface to the inner one. Outer shell is made of Lead, followed by shells of Copper, Aluminum and Graphite. The collimator efficiently shields the active element of the

Parameter	PiN diode Detector	SDD Detector
Be window	25 μm	13 μm
Crystal Area	13 mm^2	25 mm^2
Crystal Thickness	300 μm	500 μm
Dead layer	0.15 μm	0.15 μm
Bias Voltage	+100 V	-130 V
Operating Temparature	215 K	210–230 K

Table 3.3: Details of both the detectors

detector as observed from the overall reduction of the spectral background. The front surface of the collimator is covered with a mylar foil (100μm thick) to cut off X-rays below $\sim$ 5 keV. Apart from reducing the low energy X-ray background, it significantly reduces the dead time loss of the data acquisition system. From the available data on X-ray attenuation in Mylar [125], the chosen absorber cuts $\sim$ 83.8% of X-rays below 3 keV and $\sim$ 99.8% of X-rays below 2 keV. The distance between target center and the detector collimator entrance is 77 mm. Thus, the detector subtends a solid angle of $\sim 5.3 \times 10^{-4}$ steradian at the target center.

3.5.1 Detector Placement

The detector is placed at 55° angle with respect to the incident beam, for special considerations, arising due to the emission of characteristic X-rays. When a vacancy is created in an atom by removal of electron having total angular momentum $j \geq \frac{3}{2}$ by an impact of charged particle, the ionized atom becomes aligned with respect to the beam axis[43]. This atomic alignment is due to the different number of vacancies in different magnetic sub-states $|m|$. This alignment is reflected through the anisotropic angular distribution of characteristic X-rays and Auger electrons emitted from the aligned ions[39, 43, 126]. For dipole-type X-rays resulting from the decay of an aligned vacancy created by collimated unpolarized charged particles, the angular distribution

of intensity relative to incident beam axis is given as

$$I(\theta) = \frac{I_\circ}{4\pi}(1 + \alpha\kappa A_{20} P_2(\cos\theta)) \tag{3.4}$$

where $I_\circ$ is total intensity of X-ray line, α is a constant depending on total angular momentum of initial and final vacancy state, κ is Coster-Kronig correction factor, θ is angle between incident beam and detector, $P_2(\cos\theta)$ is second order Legendre polynomial in $\cos\theta$ and A_{20} is the alignment parameter for given subshell.

According to the Eqn 3.4, to obtain total intensity of X-ray lines such as, L_{α_1}(originating from $L_3(2p_{3/2})$ subshell), we need to know all the parameters mentioned in Eqn3.4. To avoid the use of these parameters and thus avoiding the dependence of current measurement on other's experiment or theoretical results, one can exploit the fact that the factor $P_2(\cos\theta) = \frac{1}{2}[3\cos^2\theta - 1]$ goes to zero at $\theta = 55°$ making intensity measurement independent of alignment parameter. Thus we have put our detector at 55° angle, where the total X-ray count for any X-ray line is given as the counts detected by the X-ray detector scaled by efficiency factor.

3.5.2 Resolution Measurement

The resolution measurement was essential for obtaining the efficiency of the detector using bremsstrahlung spectra, also resolution data was helpful while fitting and deconvolution of the overlapped X-ray lines such as L_γ peak.

Resolution of the detector was obtained at different energy values using characteristic K X-ray lines of various elements. To get the K X-rays, thick foil of pure elements were used as target and was excited by single energy X-ray source. The source used was ^{241}Am enclosed in SS container so that only 59 keV gamma ray from the electric dipole transition in ^{237}Np are emitted from it. The data was taken at the reflection geometry so as to avoid the main flux of X-ray source to enter the

detector. The K X-ray spectrum is then fitted with single Gaussian peak to obtain the FWHM. The resolution curve obtain for SDD detector is as shown in Figure 3.8, which also lists all the elements used to obtain the resolution data. The resolution curve is fitted with equation $\Delta E/E = 0.05 \times E^{-0.48}$

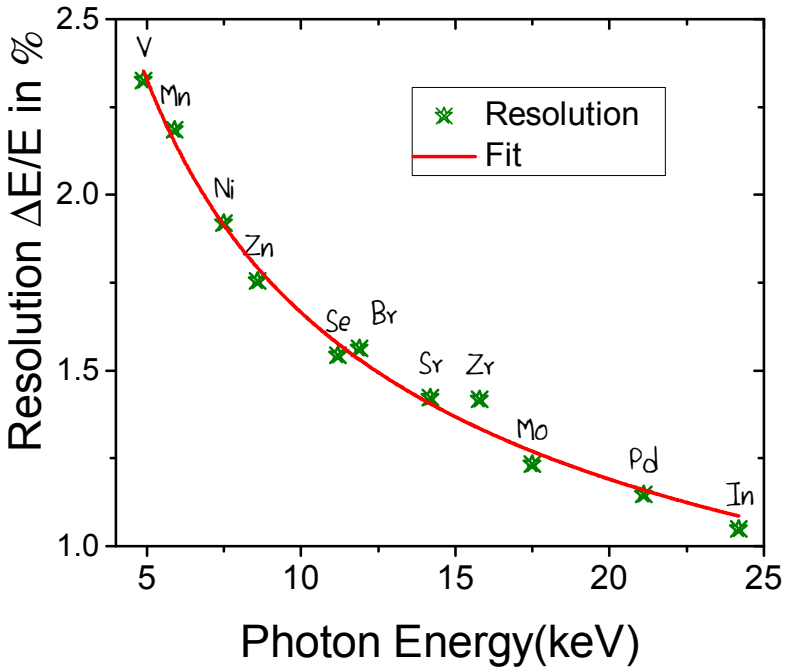

Figure 3.8: Detector resolution $\Delta E/E$ in % at various energie. ΔE is FWHM at energy E.

3.5.3 Efficiency Measurement

To obtain the actual number of X-rays produced from the measured photon intensity it is essential to know the detector efficiency i.e., the ratio of number of photons detected to the actual number of X-rays produced. The efficiency of detector has two parts viz., geometric efficiency and intrinsic efficiency and is expressed as,

$$\epsilon(E) = \epsilon_{int}(E)\frac{\Omega}{4\pi} \tag{3.5}$$

where Ω is solid angle subtended by active area of detector at the target(i.e., detector area exposed after collimator is mounted) and $\epsilon_{int}(E)$ is intrinsic efficiency, at incident X-ray energy E. Intrinsic efficiency is specific to the detector and depends on

attenuation capabilities of various detector elements like Be Window, dead layer, crystal thickness etc. Theoretically the intrinsic efficiency can be written as,

$$\epsilon_{int} = \exp(\sum_i -\mu_i t_i)(1 - \exp(-\mu_d t_d)) \tag{3.6}$$

where, t_i is the thickness of various layers in front of detector crystal and μ_i is the absorption coefficients for respective layers. t_d and μ_d are the thickness and absorption coefficients of detector crystal. The theoretical curve is computed using NIST attenuation values [125] and nominal device specifications given in Table 3.3.

The factor $\Omega/4\pi$ in Eqn 3.5 is called the geometric efficiency, and efficiency including both the geometric and intrinsic part is known as total efficiency. Although it seems very easy to obtain the geometrical efficiency from purely geometrical considerations, it's calculation is not straightforward and trivial, mainly because the source is not always the point source and has different shape and sizes (elliptical or circular). So instead of obtaining geometric and intrinsic efficiency separately by calculations, the measurement of total efficiency in the actual experimental conditions is more accurate. To obtain the total efficiency of the detector from experiment, three different processes were used in which, various sources of X-rays were used, (i) Characteristic X-ray lines from ^{241}Am source, (ii) Characteristic K X-ray lines of copper target, and (iii) bremsstrahlung spectrum of thick foils.

It is very standard process to use calibrated radioactive sources to obtain the efficiency of X-ray detectors. Accordingly, we have used characteristic x-ray lines from ^{241}Am source of 1 μCi strength to obtain the intrinsic efficiency of our detectors. The source was placed at short distance (15mm) in front of detector and counts were recorded under the Neptunium L X-ray peaks which were converted to the intrinsic efficiency using relative intensities of non-overlapping lines in Am spectrum. Relative intensities of x-rays were taken from Lepy et. al [127]. The same process, if repeated with source at target position in experimental chamber and detector placed at its

respective position gives the total efficiency, but as the source is feeble, this method was not feasible. So to obtain the total efficiency, copper K X-ray yields due to electron beam bombardment at known energy on a copper target of pre-determined thickness and purity were used. Using Formula 3.1, and the K shell ionization data for copper [4] the efficiency at 8 and 8.9 keV was obtained. Using above two methods, along with the theoretical efficiency curve, the total efficiency of the detector in the energy range of $8-25$ keV was obtained. The total efficiency obtained for PIN diode detector is shown in Fig. 3.9. The efficiency data were fitted with a second order polynomial function: $\epsilon(E) = 1.58\times10^{-5} + 1.31\times10^{-6}E - 8.63\times10^{-8}E^2$. The overall fitting error, optimized by χ^2-minimization, was found to be $\sim 10\%$.

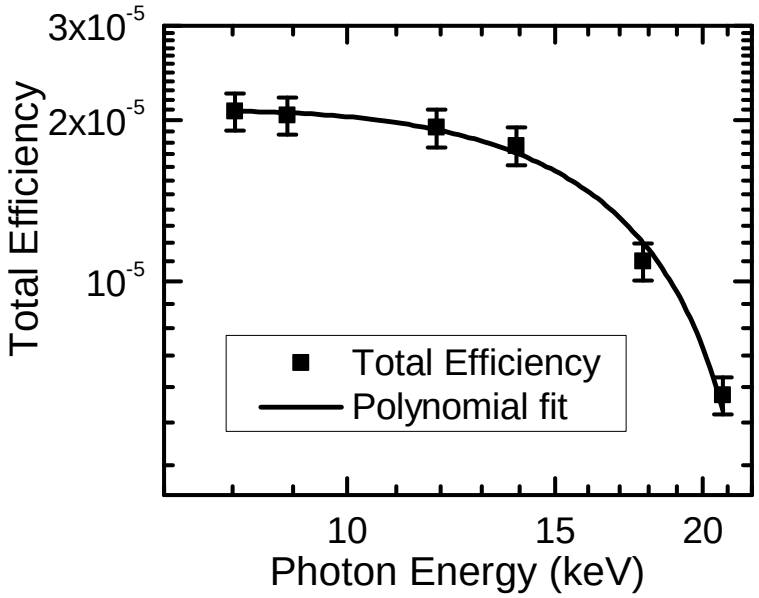

Figure 3.9: Efficiency of the PIN diode X-ray detector used in the experiment.

In an alternate approach, the efficiency of X-ray detector was obtained using the bremsstrahlung spectra of Carbon foils and other thick targets. In this method, experimental bremsstrahlung spectra was compared with the simulated spectrum, and the efficiency was obtained. Using this method, the efficiency can be obtained continuously from very low energy of 500 eV to upto any desired upper energy. In our case we obtained efficiency in the energy interval $0.5-25$ keV. The details of the

simulation procedure and efficiency obtained using this procedure is presented in the result section of Chapter 4.

3.6 Data Acquisition

The detector signal obtained from all the detectors was processed using three different data acquisition electronic systems. In case of surface barrier detector NIM based analog signal processing system was used, while for Si-PIN diode detector Amptek Inc. made analog system was used. As the signal generated from detector is very weak, it needs to be amplified without transmitting it over larger distance. After the preamplifier the signal is fed to the shaping amplifier where the signal is further amplified and properly shaped to be fed into digitizer. The output of shaping amplifier is given to the Analog to digital converter, where the signal gets digitized and lastly fed to the MCA for binning.

The SDD and PIN diode detector has the charge couple preamplifier built in with the detector unit, while in case of surface barrier detector a separate charged couple preamplifier was used. The acquisition system for surface barrier and PIN diode detector is shown in figure 3.10 as block diagram with model number of each instrument or module.

For SDD detector, Digital Signal Processing (DSP) based electronics was used. In case of SDD detector, all the data processing elements are built in a single module which is directly connected to the computer. In DSP based system, the preamplifier signal itself is digitized before any further pulse processing. The digitized signal is then further processed and is converted into the spectrum.

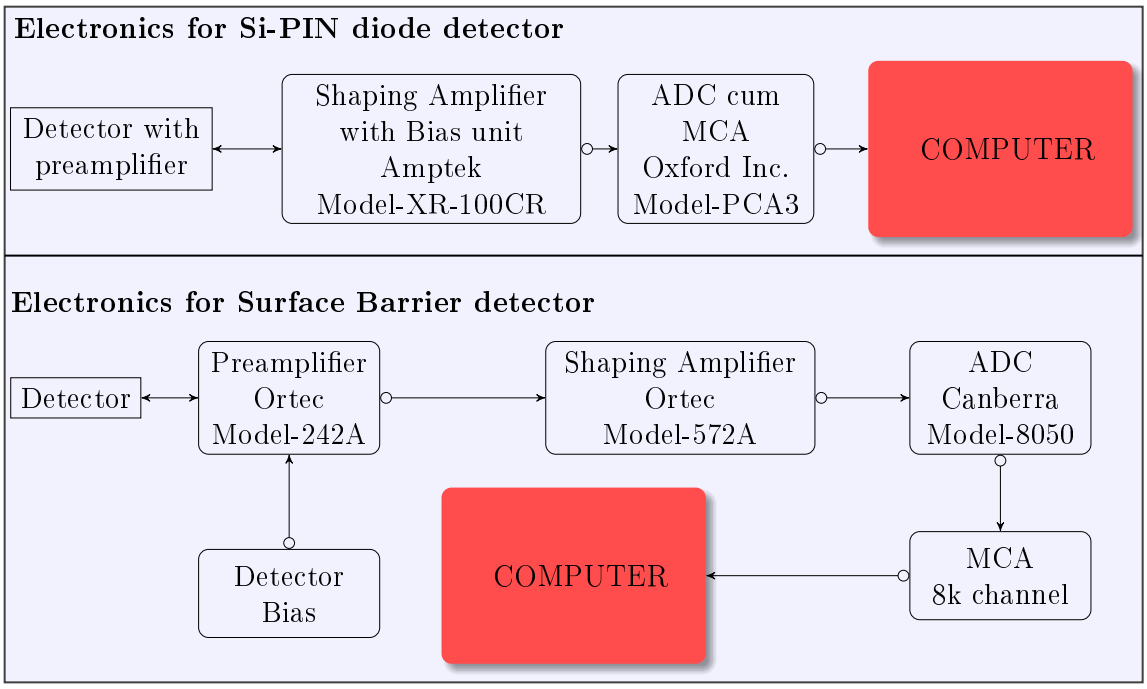

Figure 3.10: Block Diagram of Detector Electronics

3.7 Data Analysis

In the remaining part of this chapter, we will describe the method employed to extract the ionization cross section from experimentally recorded X-ray spectra. Figure 1.1 shows the allowed transitions from K and L shell. All the transitions are of dipole type and they obey the well-known selection rules eg. $\Delta l = \pm 1$ and $\Delta j = 0$ or ± 1 where l and j are the orbital and total angular momentum quantum number respectively of the atomic levels involved in the transition. From figure 1.1, we notice that the K X-ray spectra will be simple, there being only one level i.e. $1s_{\frac{1}{2}}$ where the vacancy is formed during the collision. The K X-ray spectra comprise of two groups of lines viz, K_α and K_β. The K_α group is a doublet and involve a transition from $2p_{\frac{3}{2}}$ and $2p_{\frac{1}{2}}$ levels to the $1s_{\frac{1}{2}}$ level. The K_β group is a multiplet ($K_{\beta 1}$, $K_{\beta 2}$, $K_{\beta 3}$ etc.) and involve transition from $3p_{\frac{3}{2}}$, $3p_{\frac{1}{2}}$, $4p_{\frac{1}{2},\frac{3}{2}}$ etc. to the $1s_{\frac{1}{2}}$ level. We have obtained the K X-ray spectra of Cu to obtain the efficiency. For Cu, the energy separation between two K_α lines is 20 eV and for various K_β lines, it is even lesser. As the energy

resolution of X-ray detectors used in our experiment is of the order of 150 eV at the K_α line of Cu, these various components are not resolved and we see only two lines i.e. K_α and K_β in the experimental spectrum. As all the transitions originate from the same primary vacancy in the $K(1s_{\frac{1}{2}})$ shell, it is fairly straightforward to obtain the ionization cross sections from production cross sections of various K X-ray lines and vice-versa.

In the case of L shell, however, the situation is more complicated. There are three subshells involved viz, $L_1(2s_{\frac{1}{2}})$, $L_2(2p_{\frac{1}{2}})$, and $L_3(2p_{\frac{3}{2}})$, and the primary vacancy can be formed in any of these subshells. Besides, the Coster-Kronig transitions may shift the vacancies from one subshell to another. Due to the limited resolution of semiconductor X-ray detectors, various transitions to these three L subshells are bunched as X-ray peaks which are a bit wide spread but cannot be resolved. The L X-ray spectra observed using Si-PIN diode or SDD detector consist of four groups of lines: The L_l line, which is a singlet, arising from the transition $3s_{\frac{1}{2}}$ to $2p_{\frac{3}{2}}$; the L_α group is a doublet and comes from the transitions $3d_{\frac{5}{2},\frac{3}{2}}$ to $2p_{\frac{3}{2}}$; the L_β group which is a multiplet comprises of transitions to all the three subshells eg. $3d_{\frac{3}{2}}$ to $2p_{\frac{1}{2}}$ ($L_{\beta 1}$), $4d_{\frac{5}{2}}$ to $2p_{\frac{3}{2}}$ ($L_{\beta 2}$), $3d_{\frac{3}{2}}$ to $2s_{\frac{1}{2}}$ ($L_{\beta 3}$) and various others; and the L_γ group which is also a multiplet but involves transitions to only $L_1(2s_{\frac{1}{2}})$ and $L_2(2p_{\frac{1}{2}})$ subshells eg. $4d_{\frac{3}{2}}$ to $2p_{\frac{1}{2}}$ ($L_{\gamma 1}$), $4p_{\frac{1}{2}}$ to $3s_{\frac{1}{2}}$ ($L_{\gamma 2}$) etc. It is thus clear that to obtain the three subshell ionization cross sections separately, it will be necessary to resolve at least some of the components of these multiplets. The desirable situation would be to observe at least one transition from each subshell as a separate peak in a spectrum. Similar to the K X-rays, this, however is not possible, as the resolution in the energy range of L X-rays for studied elements is in the range of $200 - 300$ eV while the separation between most transitions in a bunch of lines i.e. L_α, L_β etc. is below 100 eV. However in case of L_γ line, the separation for a few lines is higher, which we have used to our advantage and separated the X-ray lines arising from L_1 and L_2 subshells.

3.8 X-ray Production Cross Sections

3.8.1 Experimental

The X-ray spectra obtained for all the elements studied in this thesis have similar features viz. in all the spectra, the transitions are grouped in L_l, L_α, L_β and L_γ peaks except for Th and U. In the case of Th and U, $L_{\beta 1}$ and $L_{\beta 2}$ peaks are resolved. The sample X-ray spectra of Lead and Thorium, resulting from electron bombardment at 35 keV, are shown in the Figs. 3.11 and 3.12 respectively.

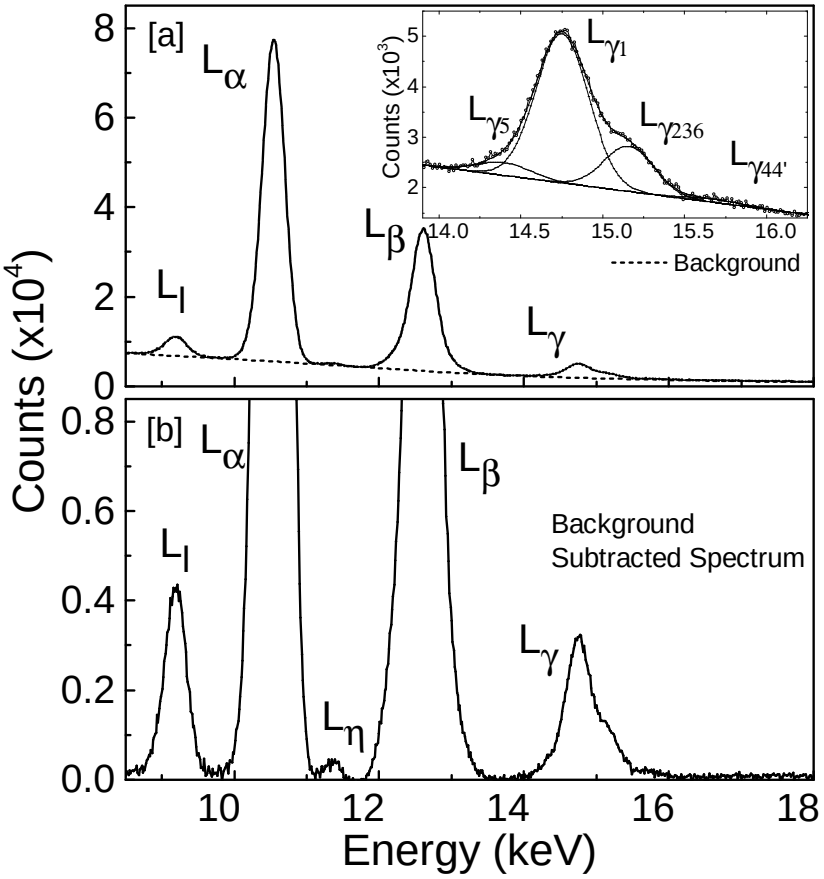

Figure 3.11: Spectrum of Lead due to 35 keV electron impact. [a] Raw Spectrum with fitted L_γ are shown in the inset. [b] Same spectrum after background subtraction.

It is essential to obtain the X-ray yield (N_X) for each peak in order to determine

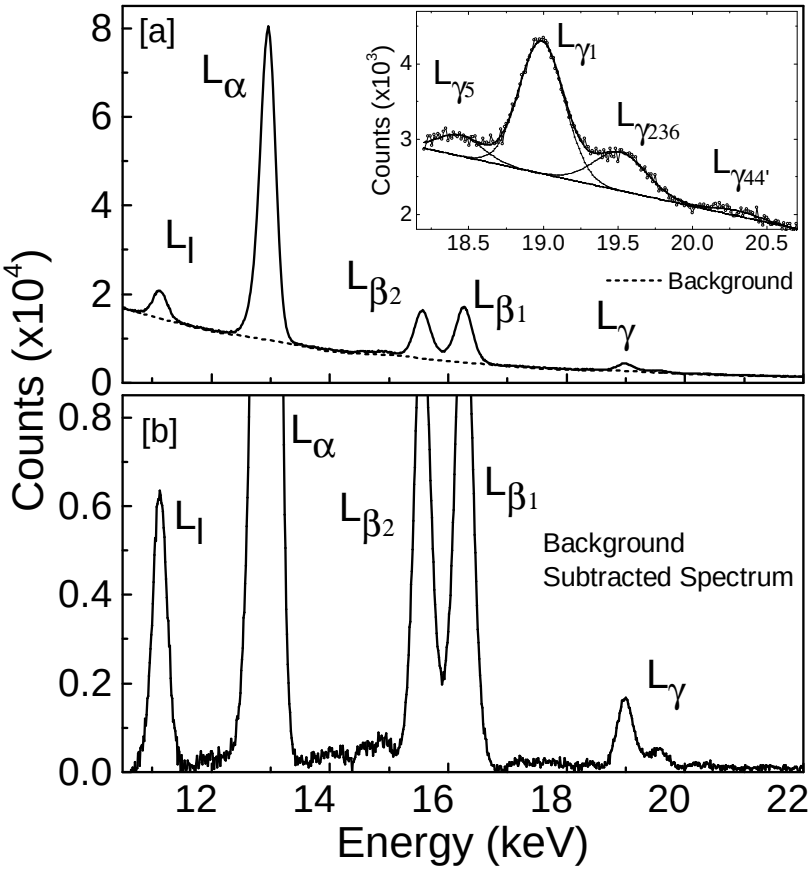

Figure 3.12: Spectrum of Thorium due to 35 keV electron impact. [a] Raw Spectrum with fitted L_γ are shown in the inset. [b] Same spectrum after background subtraction.

the production cross sections. Individual L_x peaks in the observed spectra were fitted with Gaussian profile over the bremsstrahlung background, as shown in the Figures 3.11 and 3.12 in order to calculate the X-ray yield. The fitting was done using a least square fitting program. L_α peak was fitted with a single Gaussian function for all the targets. $L_{\beta 1}$ and $L_{\beta 2}$ peaks in Th and U were fitted with two Gaussian profiles. The L_β peaks were not resolved for the remaining elements viz. Au, Pb, and Bi and therefore, single Gaussian with higher FWHM value was fitted. Two peak fit by using two Gaussians at the precise $L_{\beta 1}$ and $L_{\beta 2}$ energies were also tried out but the summed L_β yield did not differ by more than $\sim 5\%$ from the single peak fit as mentioned above. L_γ peaks in Au, Pb and Th were resolved into three constituent lines viz., L_{γ_5}, L_{γ_1},

and $L_{\gamma_{236}}$. These constituent peaks were fitted with separate Gaussian functions. Fitted L_γ spectra are shown in the insets of Figures 3.11[a] and 3.12[a]. Due to experimental limitations, Bi and U data could not be obtained with higher statistics, hence for these two elements, the L_γ peak could not be resolved. The net counts obtained from the experimental spectra were corrected for various systematic errors. The corrected net counts were then converted into the production cross sections using Eqn 3.1.

Corrections for Systematic Effects

Background Subtraction

The first effect to take care of, is the background bremsstrahlung radiation, as the peaks of interest are on top of bremsstrahlung background. Although the bremsstrahlung radiation is not linear over the entire X-ray spectrum, due to the small interval of energy spanned by each peak, bremsstrahlung background over the same energy range was considered as linear. The correction for background was applied while the fitting of the peaks itself and the net count for a particular line was obtained by subtracting total count under interpolated linear baseline from the integral count under the peak as shown in inset of Figures 3.11[a] and 3.12[a].

Self Absorption Correction

The characteristic X-rays, produced by electron impact, travel through the target film before emerging out of it and eventually reaching the detector. During this travel there is a small but finite probability that the X-rays may get absorbed in the target material itself and therefore the observed counts will be lower than the actual number of emitted X-rays. Hence, the net count was corrected for the self-absorption in the target. Self-absorption correction was done using Eqn 3.7 and assuming that

Element		Au			Pb			Bi	
Eff. Path		0.07			0.06			0.13	
Line	E (keV)	μ	$f(\%)$	E (keV)	μ	$f(\%)$	E (keV)	μ	$f(\%)$
L_α	10.00	4.49	1.56	10.50	7.74	0.81	10.80	9.45	1.32
L_β	11.40	6.34	1.10	12.60	12.60	0.50	13.00	15.20	0.82
L_γ	13.40	3.89	1.79	14.80	7.91	0.79	15.20	9.34	1.34
		Th			U				
		0.06			0.04				
Line	E (keV)	μ	$f(\%)$	E (keV)	μ	$f(\%)$			
L_α	13.00	10.03	0.58	13.50	6.07	0.59			
L_β	15.70	16.60	0.35	16.40	10.31	0.35			
L_γ	19.00	11.72	0.49	20.10	7.41	0.48			

Table 3.4: The self-absorption correction factor ($f = (N' - N_\circ)/N_\circ$) expressed in % for each X-ray line due to self absorption in target film. Here μ is the attenuation length in microns obtained from [7].

X-rays were created midway inside the target and reached the detector.

$$N' = \frac{N_\circ}{\exp(-x/\mu)} \tag{3.7}$$

where, N' is corrected counts, $N_\circ$ is observed counts and μ is the attenuation length for X-rays. The self-absorption correction factors (f), as obtained from the known attenuation lengths from Ref. [7], are shown in Table 3.4.

Secondary Contribution of Bremsstrahlung Photons

The bremsstrahlung X-rays generated inside the target can, in turn, ionize the target atoms, thereby producing unwanted characteristic X-rays. It is, therefore, important to subtract the additional X-ray yield from the observed X-ray yield for each line. It turns out that, for all the elements at all the energies, there is almost no enhancement in the characteristic X-ray peak due to bremsstrahlung. This was confirmed by calculating the number of vacancies created by the total bremsstrahlung photons of energy higher than the electron binding energy of the corresponding shell.

The required photo-ionization cross sections were taken from XCOM [128]. For example, in the case of Bi (the thickest target in our experiments), at 35 keV electron impact energy, about 9×10^5 bremsstrahlung photons are produced, having energy greater than the shell binding energy, which can ionize the $L3$ subshell. As the photo-ionization cross section for L_3 subshell at the energies above its ionization threshold is of the order of 10^2 barns/atom, it is easy to see that the vacancy created by these photons will be less than 2×10^2, the contribution of which to the characteristic peak is negligible.

Pile-up Effect

In the X-ray detector system consisting of the X-ray detector, followed by charge sensitive preamplifier and the shaping amplifier, pulse pile-up happens when two consecutive pulses arrive in quick succession within an interval less than the pulse resolution time for the system. When the photon flux into the X-ray detector is large, the detector system cannot distinguish between two consecutive pulses. It simply records the two pulses as a single event of pulse amplitude more than that of the true pulse. This is the pile-up effect which gives rise to spurious peak at higher energy. The error in the measured X-ray yield due to pile up effect can be corrected by using the throughput curve of the detection system.

In our X-ray detector system, when operated at the highest shaping time (for best resolution) the input count rate can be as high as 1000 cps without any pile-up effect (i.e., throughput is unity corresponding to input count rate = output count rate of the detector system). During the experiment, we have kept the count rate below 300 cps all the time so that no correction for pile-up effect or MCA dead time was required.

Backing Correction

In the case of the targets backed by Al foil, i.e. Thorium, and Uranium, the X-ray counts were further corrected for effects due to the presence of backing. The procedure followed in accounting for the effect of backing is provided in detail in the next chapter.

3.8.2 Theoretical estimates of Production cross sections

Due to experimental limitations, ionization cross sections could not be obtained for Bismuth and Uranium, in this thesis work. For these two elements, only production cross sections were available from our experiment. Therefore, it was necessary to obtain the theoretical estimates of the production cross sections for comparison with our experimental results.

All the theoretical models described in Chapter 2, gives ionization cross sections as output, and production cross sections are not readily available from these models. It was pointed out in the Chapter 1 that production cross sections can be calculated from theoretical models, provided the physical parameters involved in the calculations are known. These parameters, known as the atomic relaxation parameters are obtained from various experiment and are available in tabular form as atomic database [129, 130]. The production cross sections of L_l, L_α, L_β and L_γ transitions are related to ionization cross sections of L_1, L_2 and L_3 subshell via following formulas,

$$\sigma_{L_l} = [\sigma_{L_1}(f_{12}f_{23} + f_{13}) + \sigma_{L_2}f_{23} + \sigma_{L_3}]\omega_3 S_{l,3} \tag{3.8a}$$

$$\sigma_{L_\alpha} = [\sigma_{L_1}(f_{12}f_{23} + f_{13}) + \sigma_{L_2}f_{23} + \sigma_{L_3}]\omega_3 S_{\alpha,3} \tag{3.8b}$$

$$\begin{aligned}\sigma_{L_\beta} &= \sigma_{L_1}[\omega_1 S_{\beta,1} + \omega_2 f_{12} S_{\beta,2} + \omega_3(f_{13} + f_{12}f_{23})S_{\beta,3}] \\ &\quad + \sigma_{L_2}(\omega_2 S_{\beta,2} + \omega_3 f_{23} S_{\beta,3}) + \sigma_{L_3}\omega_3 S_{\beta,3}\end{aligned} \tag{3.8c}$$

$$\sigma_{L_\gamma} = \sigma_{L_1}[\omega_1 S_{\gamma,1} + \omega_2 f_{12} S_{\gamma,2}] + \sigma_{L_2}(\omega_2 S_{\gamma,2}). \tag{3.8d}$$

Here, $S_{i,I}$ is the fraction of radiative transition to the I^{th} subshell associated with the L_i peak, f_{ij}'s are the Coster-Kronig transition probabilities between subshells L_i and L_j, and ω_i's are the fluorescence yields corresponding to subshells L_i.

3.9 Ionization Cross Sections:

It has been mentioned before that for obtaining the three subshell ionization cross sections separately, it is necessary to de-convolute the observed L_γ peaks into its component lines. Out of five elements studied in this thesis, it was possible for Au, Pb, and Th only to resolve L_γ complex into its constituent transitions. As L_γ complex contains the transition from both $L_1(2s_{\frac{1}{2}})$ and $L_2(2p_{\frac{1}{2}})$ subshells, production cross sections of its resolved constituents, along with production cross sections of L_α or L_l peak containing transition from L_3 subshell can be used to obtain the ionization cross sections for all the three subshells. The relation between production cross sections of separate L_γ lines with ionization cross sections of L_1 and L_2 subshells is given as,

$$\sigma_{L_{\gamma_{2+3}}} = \sigma_{L_1}\omega_1 S_{\gamma_{2+3,1}} \tag{3.9a}$$

$$\sigma_{L_{\gamma_{4+4'}}} = \sigma_{L_1}\omega_1 S_{\gamma_{4+4',1}} \tag{3.9b}$$

$$\sigma_{L_{\gamma_{1+5}}} = [\sigma_{L_1} f_{12} + \sigma_{L_2}]\omega_2 S_{\gamma_{1+5,2}} \tag{3.9c}$$

Using Equations 3.8a, 3.8b, 3.8c, 3.8d and Equations 3.9a, 3.9b, 3.9c, which relate the ionization cross sections to different production cross sections, there can be 35 different combinations of 3 different measured production cross sections which could, in principle, be used to extract the ionization cross sections. But not all the combination gives the correct results, in fact, some combinations such as $(L_\alpha, L_\beta, L_\gamma)$ results in the negative values for ionization cross sections. The detail description of some of the methods have been given in Ref. [131–133]. Lapicki have suggested that, the best combination for obtaining the subshell resolved ionization cross sections is using $(L_\alpha\ L_{\gamma 15}\ L_{\gamma 23})$ [134]. Therefore, the experimentally obtained production cross

sections can be converted to the ionization cross sections using the following equations:

$$\sigma_{L_1} = \frac{\sigma_{L_{\gamma_{2+3}}}}{\omega_1 S_{\gamma_{2+3},1}}, \tag{3.10a}$$

$$\sigma_{L_2} = \frac{\sigma_{L_{\gamma_{1+5}}}}{\omega_2 S_{\gamma_{1+5},2}} - \sigma_{L_1} f_{12}, \tag{3.10b}$$

$$\sigma_{L_3} = \frac{\sigma_{L_\alpha}}{\omega_3 S_{\alpha,3}} - \sigma_{L_1}(f_{12}f_{23} + f_{13}) - \sigma_{L_2} f_{23}. \tag{3.10c}$$

It is evident from Eq. 3.10a that the $L_{\gamma_{2+3}}$ production cross section is needed to obtain the L_1 sub-shell ionization cross section. However, due to limited energy resolution of the X-ray detectors, the L_γ peak is resolved into L_{γ_5}, L_{γ_1}, and $L_{\gamma_{236}}$ peaks; and at higher energies in a few cases, $L_{\gamma_{4,4'}}$ could also be separated out. Therefore, $L_{\gamma 2+3}$ yield is not directly available from the experiment, but its contribution is embedded in $L_{\gamma 236}$ peak. To obtain the $L_{\gamma_{2+3}}$ yield, the contribution from L_{γ_6} peak must be subtracted from the experimentally obtained $L_{\gamma_{236}}$ peak. The contribution of L_{γ_6}, in turn, can be obtained from the ratio: $\Gamma_{\gamma_6}/\Gamma_{\gamma_1}$ and the L_{γ_1} yield of the fitted spectrum. Γ_{γ_6} and Γ_{γ_1} are the radiative transition probabilities for the vacancy transfer, leading to γ_6 and γ_1 peaks respectively.

The ratio $\Gamma_{\gamma_6}/\Gamma_{\gamma_1}$ is obtained either from experiment or from the data tables. An independent value of this ratio can be obtained from the experimental spectra following the prescription provided by Datz et al. [135]. In this procedure, one makes use of significant energy variation of the intensities of various L_γ components eg. γ_1, $\gamma_{2,3,6,8}$ and $\gamma_{4+4'}$. As the Datz procedure require yield of $L_{\gamma 44'}$ peak which could only be resolved at some energies, we have used $\Gamma_{\gamma_6}/\Gamma_{\gamma_1}$ ratio from theoretically available values [136–138].

3.10 Relaxation Parameters

The atomic relaxation parameters ($\omega,\ f_{ij},\ \Gamma_i,\ S_{i,I}$) needed for above calculations are taken from the data tables already available in literature. The relaxation parameters which we have used are (i) the recent tabulation of fluorescence yield by Campbell [129] and (ii) Radiative yield from Campbell and Wong [130].

The tabulated data of Campbell [129] for fluorescence yield is based on the both experimental values and theoretical estimates. For theoretical calculations, Campbell has used non-radiative emission rates calculated by Chen et al. [139] together with the Dirac-Hartree-Slater (DHS) radiative rates of Scofield [136]. The radiative yields of Campbell and Wang [130] are the interpolation of the radiation yields originally calculated by Scofield using Dirac-Fock two potential model [137]. In his work, Scofield [137] has reported radiative yields for 21 elements in the atomic range Z=18 to 94, which Campbell and Wong have interpolated for all the elements in the same atomic range.

It should be noted that the used relaxation parameters can have huge uncertainty for example, for the elements studied in this thesis, there is an uncertainty of $\sim 20\%$ in ω_1 and $\sim 50\%$ in f_{12} [129]. Also for radiative yields, there is a limited agreement between experiment and theory particularly for L_1 subshell as noted by Miranda [140]. To study the effect of relaxation parameters on the obtained ionization cross sections in our experiments, we have used another set of relaxation parameters. This set consists of fluorescence yield by Krause et. al. [141] and radiative yields from Scofield [136]. Compared to the tabulation of Campbell, the compilations of Krause are purely based on the experimental measurements and are mainly the interpolation of the available experimental data. In his work, Krause compiled the sets of values that were mutually consistent and compatible with the available body of information

(before 1974) on yields and related quantities. The radiative yields of Scofield are based on the Dirac-Hartree-Slater single potential model [136]. It is important to note here that relaxation parameters of Krause et al.. [141] and Scofield [136] were quite widely used before the work of Campbell [129] and Campbell and Wong [130]. All the relaxation parameters used in this work are tabulated in Appendix A.

Investigation on the accuracy and reliability of the atomic relaxation parameters in predicting the inner shell ionization cross sections is one of the major motivation for this thesis work. In this regard, we have obtained the ionization cross sections for Gold using two sets of relaxation parameter discussed above. The difference due to the use of two different sets of relaxation parameters is discussed in detail in Chapter 5. Also, due to resolution of L_β line in its constituent parts i.e. L_{β_1} group and L_{β_2}, we have obtained ionization cross sections for Thorium by two different methods, with an emphasis on the dependence of ionization cross sections on relaxation parameters. The results obtained are discussed in Chapter 5 on experimental results.

CHAPTER 4

Simulation

4.1 Introduction

While traveling through the target material, projectile electrons can interact with the target atoms via many physical processes like elastic collision, bremsstrahlung emission, inelastic collision etc, Out of these interactions, processes like bremsstrahlung emission can reduce the projectile energy thereby directly affecting the measured ionization cross sections in the experiment. Also, there are processes like elastic collision which, although does not change the energy of the projectile particles, but alters the traveled path of the projectile affecting the measured ionization cross sections. The effect of the elastic collision is more prominent in the case of the targets backed by Aluminum foils. In such targets, there is a finite and non-trivial probability that after traversing the target material once, the projectile electron can enter the target again, after getting elastically scattered from the thick backing. This extra path length of the projectile can increase the measured ionization cross sections. To eliminate the cumulative effect of these interactions on the measured ionization cross sections, the electron and photon

transport simulation of the projectile electron is performed for the targets which are backed by comparatively thicker Aluminum. Along with this, the simulation is used to verify that no multiple ionization event is occurring for the used thickness of the targets. Also, the efficiency of the SDD detector is obtained by simulating the electron transport in thick target and using the generated bremsstrahlung spectra. Because of the absence of the characteristic peak in the region of interest C and Al are the best choice to used as the target to obtain an efficiency of the detector. The simulations are carried out with Monte Carlo techniques using two general purpose simulation packages i.e, GEANT4 [8] and PENELOPE[9]. GEANT4 and PENELOPE packages are designed such that they can easily incorporate sophisticated interaction models and using Monte Carlo methods they can conveniently include arbitrary geometry into the calculation. Both GEANT4 and PENELOPE are the actively developed project since last 10 years have evolved in various versions over time. We have used PENELOPE2011 [15] version of PENELOPE and GEANT4.9 of GEANT4 [142], which were the latest available packages when the work started.

The current chapter outlines the structure and working of G4 and PENELOPE in the context of ionization studies. The different interaction models used by both the packages are discussed and the relevant results are presented.

4.2 Monte Carlo simulation

When a high-energy particle enters an interacting medium, due to repeated interactions it originates a cascade of secondary particles. This cascade is generally referred as a shower in radiation transport simulations. The evolution of this shower containing electrons and photons is of random nature and is favorable to solve with Monte Carlo techniques. The results obtained using the detailed simulation, i.e. all the interactions experienced by a particle are simulated in chronological succession,

are exact to the rigorous solution of the transport equation except for the inherent statistical uncertainties.

Both GEANT4 and PENELOPE simulate each particle track one by one and every track is divided into a number of smaller steps over the entire interaction volume. The number of step length depends on the number of collisions. If the number of steps (collision) is of the order of few hundreds then the detail simulation is computationally feasible and is preferred. But if the number of steps is higher, and the simulation demands huge computational resources then the recourse is sought from the multiple scattering theories, which allow the simulation of the global effect of a large number of events in a track segment of a given length.

GEANT4 and PENELOPE uses a combination of the composition and rejection Monte Carlo methods. Only the basic particle transport formalism which is common to both the simulation packages is outlined below. Every track in the simulations starts with the creation of the primary particle, whose basic parameters such as, type of particle, starting position and initial momentum is fixed by the user. At any point of time in the simulation, the "state" of the particle is characterized by the position vector r and the momentum vector k. The state of the particle is updated when it moves forward in the medium (r is modified) or if any collision takes place (k is modified). The track of the particle is divided into many smaller steps. The step length is dependent on the mean free path of the interaction considered in the simulation. In terms of cross section for a process the mean free path can be given as,

$$\lambda(E) = \left(\sum_i [n_i \cdot \sigma(Z_i, E)] \right)^{-1} \tag{4.1}$$

where, $\sigma(Z_i, E)$ is the total cross section per atom of the process, $\sum_i$ runs over all the elements composing the interaction material and n_i is the number of atoms per volume of the i^{th} element. If more than one type of interaction, say interaction A and

B with cross section σ_A and σ_B is to be simulated then, the total cross section is

$$\sigma_T = \sigma_A + \sigma_B \tag{4.2}$$

and the total mean free path is

$$\lambda_T^{-1} = \lambda_A^{-1} + \lambda_B^{-1} \tag{4.3}$$

Let us assume that the particle is an electron which start from the initial position r_p with the initial momentum k_p as shown in Figure 4.1. The particle is then moved forward till the interaction volume is met and it is stopped at the boundary of the interaction volume. The position of the particle is then modified to say, r_p^1 keeping the momentum same as k_p. At this stage, the step length is sampled according

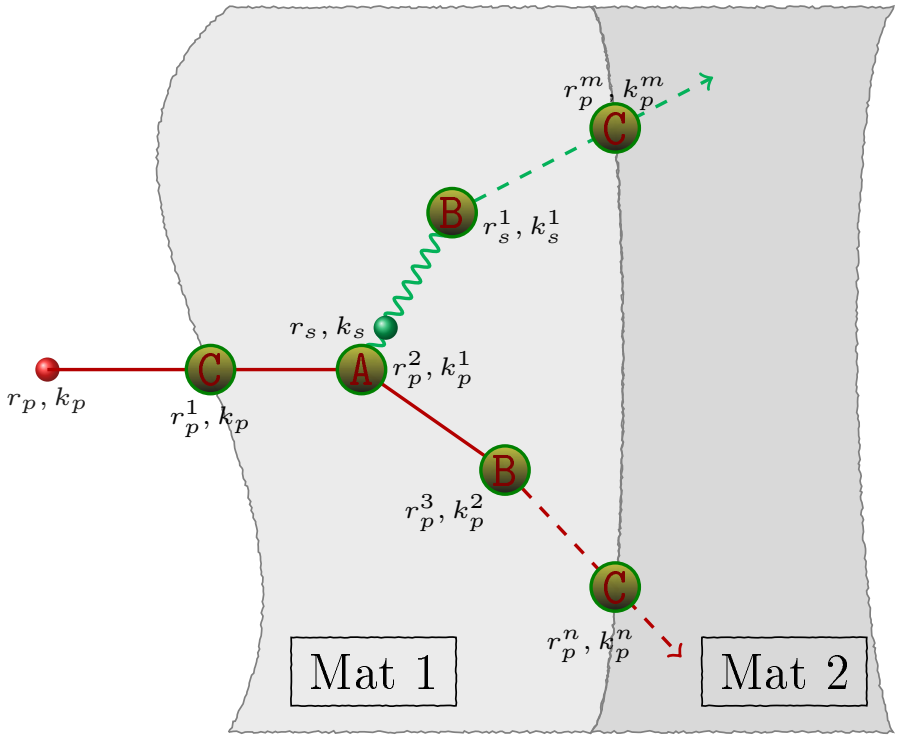

Figure 4.1: Electron path in the target. Red ball and line indicate the primary electron and its path respectively, while green ball and path indicate secondary particle and its path. The image is drawn for the illustration purpose only. A and B represent the interaction and C is the boundary crossing

to some predefined probability distribution function, for example in the case of the exponential probability distribution of the step length s, $p(s) = \lambda_T^{-1} \exp(-s/\lambda_T)$ using

inverse transform the path length s can be given as,

$$s = -\lambda_T \ln \zeta \tag{4.4}$$

where ζ is the random number distributed in an open interval $(0, 1)$. Accordingly the particle is moved forward by distance s in the direction of momentum k_p and is stopped with the new position r_p^2. At this stage the collision "takes place" i.e. first, the interaction to occur is selected by the inverse transform of the random number using the probabilities $p_A = \sigma_A/\sigma_T$ and $p_B = \sigma_B/\sigma_T$ then the momentum of the particle is modified depending on the cross section of the chosen interaction. The change in the momentum is done via various Monte Carlo techniques and is highly problem dependent [15, 143]. At this stage, the state of the particle is modified to, (r_p^2, k_p^1). Suppose that the chosen process is A and it can produce the secondary particle (e.g. bremsstrahlung or inelastic collision), then the secondary particle is generated depending on the cross sections for the process. The new particle generated is for the time being stored in the stack with its initial state as r_s and k_s. After the interaction process is finished, the first particle is again moved forward with the newly sampled step length and the procedure related to collision interaction is repeated. This process of moving the particle forward is continued until the boundary of the interacting media is met, or the energy of the primary particle becomes smaller than the predefined value called absorption energy(E_{abs}). If the energy of the particle becomes smaller than E_{abs} (defined by the user), the particle is said to be absorbed in the medium and its track is terminated there. When the particle is reached at the boundary of the 1^{st} interacting media then it is stopped at that point with state (r_p^n, k_p^n). At this point, the particle is moved forward with the momentum k_p^n, to the boundary of 2^{nd} interacting medium(if it exists in the path) from where the particle's steps continue as described for the first media. This procedure of moving the particle is followed until the particle has no more interacting material in its path. Once the track of primary particle is finished, then the secondary particles, if generated by the

primary particles are simulated, in the same fashion as the primary particle, except the starting position for the secondary particle being the position of its origination.

4.2.1 Physics Models in GEANT4 and PENELOPE

The difference between GEANT4 and PENELOPE mainly comes from the technical nature of defining the geometry, use of different computer language etc. Also, GEANT4 is more versatile, is being actively developed by many people around the globe and has much more capabilities than the PENELOPE, such as the ability to incorporate many different models for the same physical process. In fact, earlier versions of PENELOPE physics models are already included in the GEANT4 as penelope physics. The need of using two simulation packages is due to the different physics models these two packages provide for an inelastic collision interaction. In this thesis work the simulation is performed to study the modification of ionization cross sections because of electrons backscattered from the Aluminum backing, and to obtain the bremsstrahlung yield for efficiency measurement. As the change in ionization cross sections mainly occurs due to elastic scattering and inelastic collisions, the details of cross section values used for these processes is provided in the next section.

GEANT4 Physics List

The GEANT4 package is written in the C++ programming language and due to object-oriented nature of C++, GEANT4 is highly modular. The module dedicated to providing the simulation with the required cross section values is called as physics list. Physics list is the main physics part of GEANT4 simulation which contains instructions to use physics model for the physical process to be considered in the simulation. In the energy range of our interest, there are mainly two physics list provided in GEANT4 specifically designed to describe the inner shell ionization, namely Penelope physics list and Livermore physics list. The details of the physical

process described and energy range of applicability of these models is given in Table 4.1.

Physics list	Range	Processes
Liveremore	250 eV - 100 GeV	Ionization, Bremsstrahlung
Penelope	250 eV - 1 GeV	Ionization, Bremsstrahlung

Table 4.1: GEANT4 Low energy physics list details.

To describe various electron interaction processes, Livermore physics list uses the cross section data from Livermore evaluated data library [144–146]. These data libraries are extensive and contain all the interaction models for electron passing through the material medium.

In EEDL database, the inner shell ionization cross sections are based on the Seltzer's work [11]. Seltzer divides the ionization collisions into two components; close collisions and distant collisions. The close collisions contribution is obtained from the modification to Moller's binary collision cross section formula [12]. As mentioned in the theory part, Moller's formula is based on plane wave born approximation theory which was generalized to relativistic form in which electron wave functions are solutions of the Dirac equation and the interaction is represented by an effective Hamiltonian. It should be noted that Moller's cross section takes care of the electron exchange effect. The distant collision part is given by Seltzer's modification of Welzsacker-William's method(see Ref [147]), where the cross section is described in terms of a virtual photon field interacting with the atomic electrons. The Penelope physics list of GEANT4 uses physics models used in the older version of PENELOPE package(penelope2001). In this version, the electron impact ionization of inner shells is simulated using cross sections obtained from an optical-data model of the Generalized oscillator Strength [13, 14]. These cross sections are also obtained from an approximate formulation of the plane-wave (first) Born approximation (PWBA).

The bremsstrahlung cross data is based on the extensive tables produced by Seltzer and Berger [148, 149]. These tables give the scaled differential cross sections (differential in energy) for all the elements (Z=1-92) in the electron energy range from 1 keV to 100 GeV. The tabulated scaled DCS are given for the emission in the field of atomic electrons (electron-electron bremsstrahlung) and in screened field of the nucleus (electron- nucleus bremsstrahlung), along with this their sum, the total scaled DCS is also provided in the tables. The scaled DCS for electron- electron bremsstrahlung was obtained from the theoretical results of Haug [150] which are combined with a screening correction that involves Hartree-Fock incoherent scattering functions. The electron-nucleus bremsstrahlung DCS was calculated by combining analytical high-energy theories with the results from partial-wave calculations by Pratt et. al. [151]. It should be noted that the Seltzer and Berger's scaled DCS tables constitute the most reliable theoretical representation of bremsstrahlung energy spectra available. And the quoted uncertainty for the energy range of our interest is from 5 to 10%. In both the physics list i.e. penelope and livermore, the total bremsstrahlung cross sections at incident electron energy is taken from the EEDL database [145]. Using this data the probability of generation of photon and angle of emission is calculated differently as described in GEANT4 manual [152].

The data table provides the data for few energy points in the overall energy range(about 10 energy points between 10 eV and 100 GeV, for bremsstrahlung data). For the intermediate energies the cross section data is obtained by log-log interpolation scheme given by formula,

$$\log(\sigma(E)) = \frac{\log(\sigma_1)\log(E_2/E) + \log(\sigma_2)\log(E/E_1)}{\log(E_2/E_1)} \tag{4.5}$$

where, E is the energy at which cross section is calculated, E_1 and E_2 are the closest lower and upper energies respectively for which the cross sections σ_1 and σ_2 is available.

The elastic scattering cross section data used is similar to the other physics list used in GEANT4. These cross sections are obtained from modified version of, the single scattering model of Wentzel [153]. In this model, the elastic scattering of particles with charge ze by atomic nucleus with atomic number Z is described by simplified scattering potential,

$$V = \frac{zZe^2}{r} \exp(-r/R) \tag{4.6}$$

here the exponential factor represents the screening, and the parameter R is screening radius [154]. The cross sections data are obtained from the analytical expression based on PWBA based solution for above potential [152].

PENELOPE Physics

As the physics models used in the recent PENELOPE version i.e, (PENELOPE2011) are not yet included in the penelope physics list of GEANT4, we have used PENELOPE2011 package which uses the most recent description of the ionization process. In the used version of the PENELOPE, more elaborate theoretical description of ionization cross sections is used in which ionization cross sections are obtained from the GOS model based on relativistic distorted-wave Born approximation (DWBA). Detail description of used DWBA model is already provided in Chapter 2. The bremsstrahlung cross sections used in PENELOPE are the same as that used in penelope physics list of GEANT4. For elastic collisions of electrons the numerical partial- wave cross sections for free neutral atoms are used. These cross sections are calculated with the program ELSEPA(ELastic Scattering of Electrons and Positrons by Atoms) written by Salvat et al. (2005). This program performs accurate relativistic (Dirac) partial-wave calculations of elastic scattering of electrons and positrons by free atoms and allows consideration of different scattering-potential models.

4.2.2 Simulation of Characteristic X-rays

PENELOPE and GEANT4 simulate the fluorescence process in the similar fashion. The emission of characteristic X-rays and Auger electrons that result from the vacancies produced in K, L, M and N shells by electron impact is simulated and the procedure is given as follows,

1. If the subshell in which vacancy is produced is not included in the data then the energy equal to the binding energy of subshell is deposited locally.

2. If the subshell is included in the data, then an outer subshell is randomly selected, according to the relative transition probabilities for all possible outer subshells.

3. If the energy corresponding to the transition is more than the predefined cutoff energy, then the photon of energy equal to the transition energy provided by EADL database is created and is emitted in a random direction.

4. The procedure from the first step is repeated for the subshell where the vacancy is migrated.

The predefined cutoff energy is set by the user or has some default value(50eV for GEANT4). The procedure described above generates the cascade of vacancy transfer and is repeated until the vacancy is migrated to the outer shell. Sub-shells with the ionization energy less than the cutoff energy or beyond the N7 subshell is considered as the outer shells. The vacancy in the outer shell is then decayed by depositing the energy equal to the binding energy of that subshell locally. The important thing to note here is that neither GEANT4 or PENELOPE take into account the angular distribution of characteristic x-ray emission, the emitted photons are uniform in the 4π solid angle.

Along with the fluorescence process, the Auger emission process is simulated simultaneously on the same ground using the similar procedure as described for fluorescence. The required transition probabilities are obtained from the LLNL Evaluated atomic data libraries [146]. In the EADL database, the transition probabilities are available for elements from Z= 6 to 100, for the subshells K, L, M, N and some O sub-shells. For the subshells O, P, Q, the transition probabilities are negligible and smaller than the precision with which they are known.

4.3 Simulation Details

The simulation was done using both the packages with exact conditions as in the actual experiment i.e, a pencil-like electron beam of 2 mm diameter was impinged on thin targets at normal incidence, and the emitted x-rays were detected with a detector placed at an angle of 135^0 with respect to the beam direction. The projectiles were created randomly within the $2mm$ diameter circle and allowed to impinge on the targets along the straight line path with the fixed energy. As the emitted X-rays (both characteristic and Bremsstrahlung) are symmetric in ϕ axis, the X-ray detector in the simulation is made annular with and opening angle of 3° as seen from the interaction center. The schematic of the simulation process is shown in Figure 4.2. The characteristic X-rays are considered as emitted isotropically, so, in principle, the detector can be put in 4π angle when doing simulation for X-ray enhancement. But the results obtained will be slightly lower due to absorption of X-rays in the target itself. Entry of the projectile electrons into the target, and the resulting ionization events and emission of X-rays were recorded event by event.

While generating X-ray spectra by simulation, the process becomes inefficient and excessively time-consuming due to (i) low inner shell ionization and subsequent radiative decay probabilities, and (ii) use of thin film media in the experiment. Due

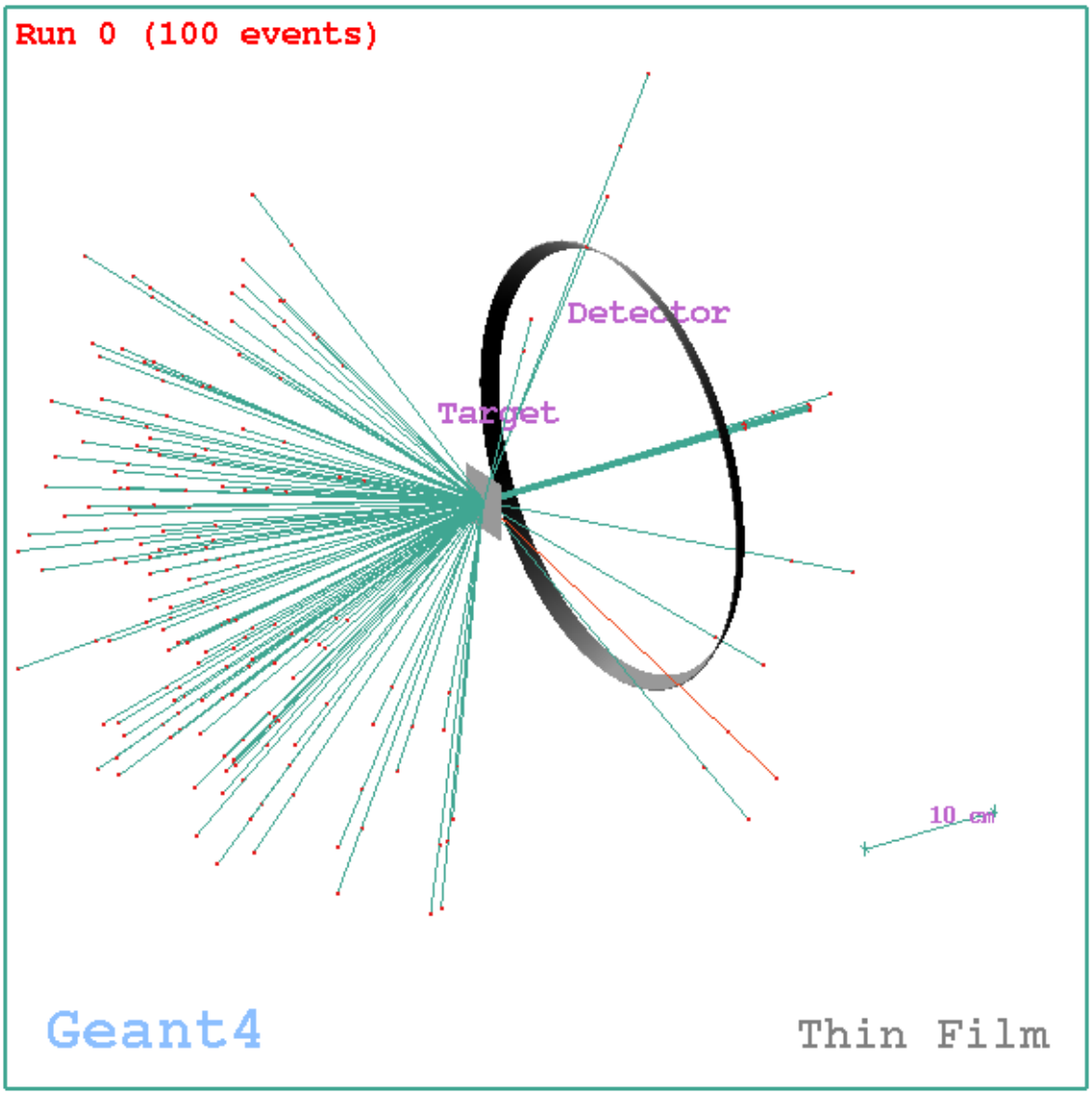

Figure 4.2: Simulation of 100 electron tracks in GEANT4. The red lines show the path of electrons while the green lines show the path of secondary photons.

to these small probabilities the number of emitted X-rays with the feasible number of incident projectiles are small, specifically, for low-intensity lines such as L_l or L_γ. This results in large variance and reduces the predictive power of simulation. To reduce the time spent on computation and to increase the efficiency of simulation, it is necessary to use some variance reduction technique. Both the packages provide various variance reduction techniques [15, 152]. The technique which we have used is the one in which, the cross sections corresponding to a process of interest (in our case

inelastic collision and bremsstrahlung) is increased artificially by some weight factor F, but keeping the probability distribution functions for energy loss and angular deflections same as for the real process. The simulations are now carried out with this enhanced cross sections for the projectiles, and finally to account for the biasing introduced by the simulation process, appropriate statistical weights are applied to all the generated secondary particles.

The simulation is performed at the various thickness ranging from $t_e/10$ to t_e*10 and energies covering the experimental energy range. Here t_e is the thickness of the target used in the experiment. To obtain the average quantities such as number of inelastic collision per projectile, or energy loss of projectile in the target, simulation is performed with 10^5 events, while to simulate the x-ray yield enhancement due to presence of Al backing, or bremsstrahlung from the Carbon sheet, $10^8 - 10^9$ events are simulated.

4.4 Results.

As described earlier, the simulation is run for verifying single ionization condition for the used targets in the experiments, to obtain the correction due to the presence of the Aluminum backing in few targets and to obtain the efficiency of SDD detector. For this purpose, We have mainly used the results obtained with the PENELOPE code, as this package is particularly applicable to our energy range of interest, whereas, the results from GEANT4 provided the complementary study. In this section, various results obtained from the simulation, and the comparison between the three models used is presented.

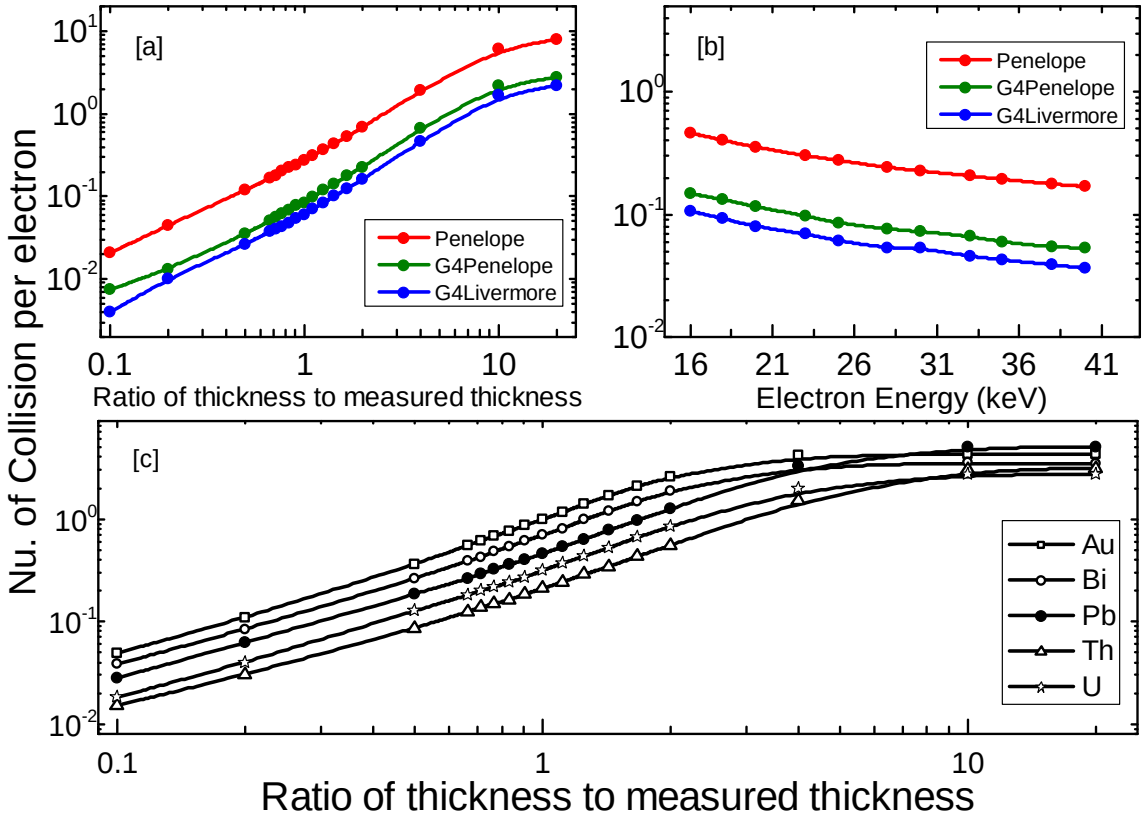

Figure 4.3: (a) Average number of collisions per projectile plotted as the function of thickness in Pb for 25 keV electrons. (b) Average number of collisions plotted as the function of projectile energy for 80 $\mu g/cm^2$ lead target. (c) Average number of collisions plotted for all the targets at lowest experimental incident electron energy (i.e. 16 keV for Au, Pb and Bi and 20 keV for Th and U). Here Penelope means PENELOPE2011 package, G4Penelope refers to results obtained with GEANT4 using penelope physics list and G4Livermore indicates results obtained with GEANT4 using livermore physics list.

4.4.1 Average Number of ionization events

For experimentally obtained cross sections to be valid, it is necessary that the projectiles do not loose their energy before undergoing the desired collision (i.e. L-shell ionization). But as the target is solid medium, it is impossible to avoid the collision leading to M or other shell ionization, and thereby reducing, the projectile energy. From the simulation, it is checked that on an average how many times a projectile of particular incident energy undergoes such collision. The results showing the average number of inelastic collision events occurring per projectile is presented

in Figure 4.3. Figure 4.3[a] shows the average number of inelastic collision events per projectile electrons, obtained using three different models i.e. Livermore and Penelope models from GEANT4 and PENELOPE2011. The results are plotted for projectile electrons of 25 keV energy passing through Lead. It can be seen that results obtained with PENELOPE are quite higher than that of GEANT4, which happens because in GEANT4 the inner-shell ionization process is simulated considering only K, L and M shell electrons while in PENELOPE, N and O shells are also included while considering inner shell ionization. The cross section for N and O shell ionization is $10 - 100$ times more than the total of K, L and M-shell ionization cross sections which leads to such a large difference between the PENELOPE and GEANT4 results. In Figure 4.3[b] the energy dependence of average number of inelastic collision is plotted for Lead with same target thickness as in the experiment i.e. 80 $\mu g/cm^2$. As expected, the probability of collision decreases with increase in the energy(due to a decrease in ionization cross sections and elastic collision cross sections), so the maximum probability of ionization occurs at the lowest projectile energy. Figure 4.3[c] shows the thickness variation of average number of collision for all the elements studied obtained from PENELOPE. Simulation results are obtained at the lowest projectile energy, thus, this plot shows the maximum probability of collision for each element. It can be seen from Figure 4.3[c] that the maximum probability of inner shell ionization per projectile remains less than one for all the elements, so single collision condition is satisfied for all the target films used in the experiment.

4.4.2 Energy Loss of projectile in Target

As shown in the last section, while moving through the material, projectile electron undergoes inelastic collision, owing to which, it loses its kinetic energy. In the Figure 4.4 the estimated average energy loss of projectile is plotted as a function of energy and thickness. The x-axis shows the average percent energy loss of projectile

i.e. $E_{loss}/E_{\circ} \times 100$, where E_{loss} is energy deposited in target material and $E_{\circ}$ is projectile's initial energy. Figure 4.4[a] and 4.4[b] shows the energy loss obtained using all the three models for Lead (in Figure 4.4[a] results are shown for projectile of 25 keV energy). In both the figures, it can be seen that the energy loss simulated by PENELOPE packages is almost equal to or less than the energy loss simulated by GEANT4, despite having a significant difference in the number of collisions per projectile. It happens because, the energy lost in N shell or O shell ionization is much smaller than the energy lost in K, L or M-shell ionization. Figure 4.4[c] shows the energy loss as a function of energy for each target, obtained from PENELOPE. It can be seen that, for almost all the energy point at which experiment is performed, the energy loss of projectile is less than 10%. As over this energy interval, the change in cross section is small (especially at energies up to $20 - 25\%$ above the ionization threshold), there is no need for taking this effect into account, while obtaining the production cross sections or ionization cross sections from the X-ray yield.

4.4.3 Effect of the backing.

To account for the effect of electron back-scattering in the Thorium and Uranium targets, a simulation was done with and without Aluminum backing. It is found that up to $\sim$ 4% of the electrons which ionized the Thorium or Uranium atoms and subsequently generated L X-rays were back-scattered from the Aluminum backing film. The back- scatter fraction, however, was found to depend on electron energy (E). After obtaining the estimated X-ray yield with good statistics from Monte Carlo simulation, the corresponding enhancement factor $k(E)$ was obtained as:

$$k(E) = \frac{\text{Counts under } L_x \text{ peak for Al backed target}}{\text{Counts under } L_x \text{ peak for unbacked target}}, \tag{4.7}$$

where x is α, β or γ. The Energy dependence of enhancement factor is shown in Figure 4.5. It can be seen from the figure 4.5, that the enhancement in x-

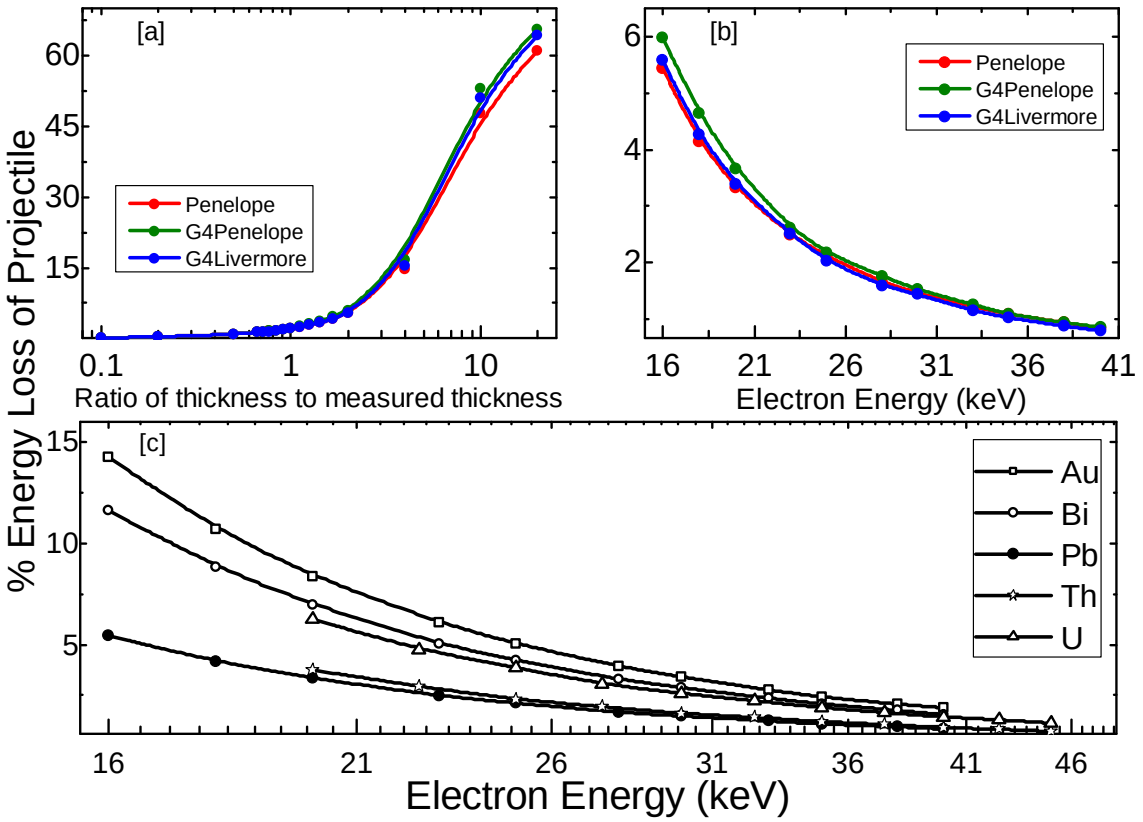

Figure 4.4: (a) Averaged percentage energy loss per projectile plotted as the function of thickness for 25 keV electron in Lead. (b) Averaged percentage energy loss per projectile plotted as the function of projectile energy for 80 $\mu g/cm^2$ lead target. (c) Averaged percentage energy loss per projectile plotted for all the targets of thicknesses as used in experiments (see Table 3.2). Here Penelope means PENELOPE2011 package, G4Penelope refers to results obtained with GEANT4 using penelope physics list and G4Livermore indicates results obtained with GEANT4 using livermore physics list.

ray yield is different for x-rays of different energies i.e. different for L_α, L_β and L_γ lines. The enhancement factor curve has the bell shaped nature,which is combined effect of elastic scattering(in Al) and inelastic collision(in Th/U). In the energy range of interest i.e. $20 - 45$ keV the elastic scattering cross section of an electron in Aluminum decreases with energy while the ionization cross sections in Thorium/Uranium increases. The increase in ionization cross sections of each shell in Th/U is comparatively rapid up to the energy 1.5 times the ionization threshold after which, the increase in cross sections becomes relatively smoother. Because of this nature of energy dependence of the ionization cross sections, it should be noted

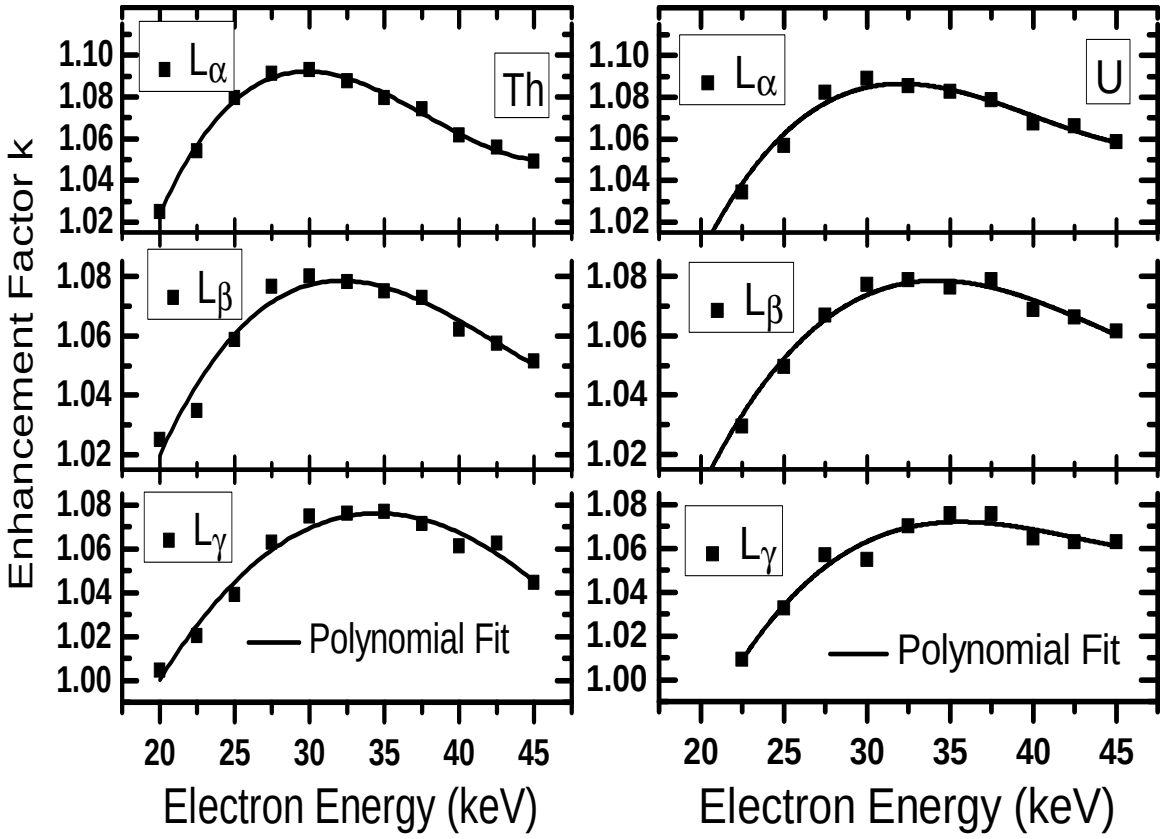

(a) Thorium (b) Uranium

Figure 4.5: Enhancement of X-ray yield due to presence of backing film

that the enhancement factor curve peaks at lower energy for L_α line because these x-rays comes from the L_3 subshell which have comparably lower ionization threshold than L_1 or L_2 subshell while the enhancement factor curve for L_γ x-rays peaks at relatively higher energy because L_γ x-rays are originated from the vacancy created in the L_2 and L_1 subshells.

4.4.4 Measurement of Efficiency.

Efficiency of the SDD detector for X-rays as function of energy within the range $\sim 2 - 25$ keV was obtained by detection of the bremsstrahlung radiation caused by deceleration of electrons inside a thick carbon sheet. The bremsstrahlung spectrum expected from the process was obtained from the Monte Carlo simulation. Simulation

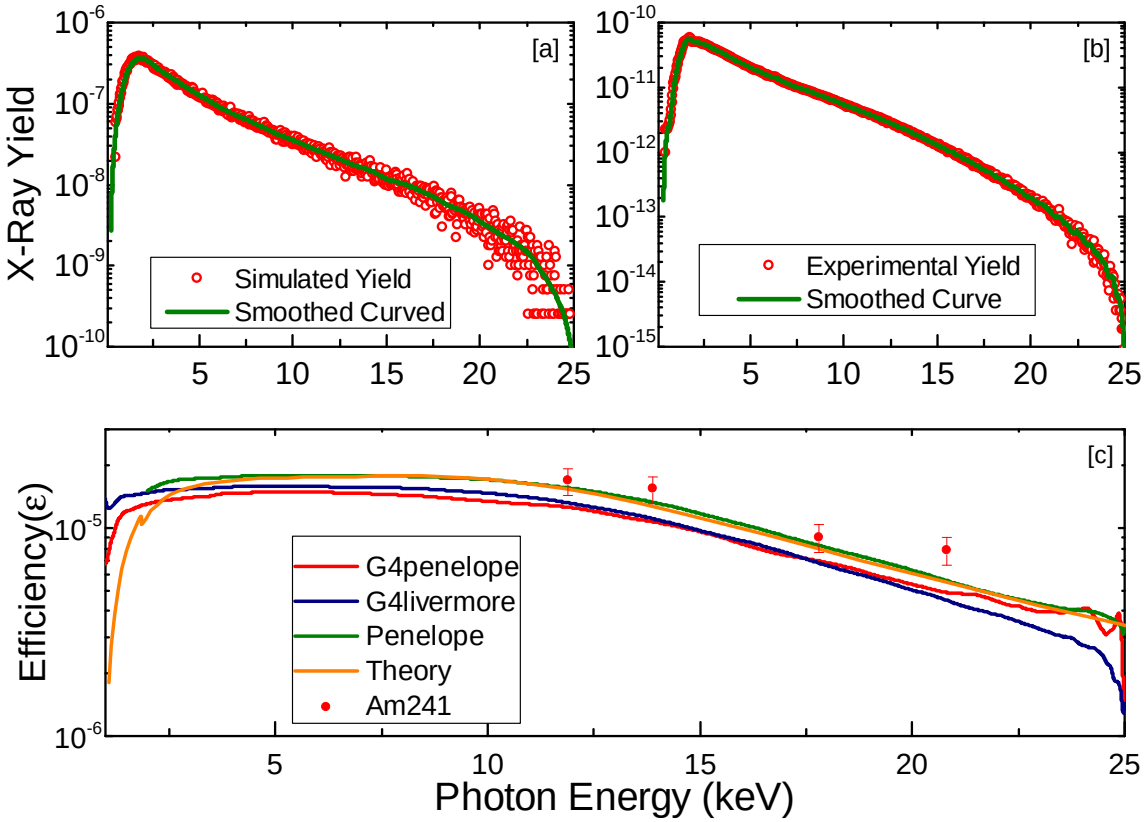

Figure 4.6: Efficiency of the SDD detector obtained with PENELOPE and GEANT4 Simulation

was done by bombarding 10^8 projectile electrons of 25 keV energy on a 10 mm $\times$ 10 mm $\times$ 1 mm thick carbon sheet. The obtained simulated spectra were convoluted with the resolution curve of the detector as shown in Figure 3.8. The final convoluted spectrum obtained from PENELOPE is shown in Figure 4.6[a]. The simulated spectra were then compared with the experimentally obtained bremsstrahlung spectra. The experimentally obtained bremsstrahlung spectra in carbon block is shown in Figure 4.6[b]. The efficiency is then obtained as,

$$eff(E) = \frac{X - ray\ ray\ yield\ obtained\ from\ Experiment}{X - ray\ yield\ obtained\ from\ simuation \times (4\pi/\Omega_s)} \tag{4.8}$$

where, Ω_s is the solid angle subtended by the detector at the point of intersection

of the beam passing through the carbon block. The efficiency curves obtained using all the three simulation models are plotted in Figure 4.6[c]. It can be seen that the efficiency obtained from all the models are in fair agreement with each other. Figure 4.6[c] also displays the scaled efficiency obtained from the theoretical curve (see Section 3.5.3). Efficiency obtained using two different methods i.e, using attenuation data for x-rays (theoretical curve) and the bremsstrahlung data are in good agreement, which establishes accuracy of the efficiency obtained with bremsstrahlung simulation. Efficiency data obtained at a few discrete energies using Neptunium L X-rays from a ^{241}Am radioactive source is also plotted in Figure 4.6[c] for comparison. It can be seen that the total efficiency obtained using both the techniques are in reasonable agreement. In particular, the efficiency curve obtained from the PENELOPE based simulation is in better agreement with the source-based efficiency data and the theoretical curve. In comparison, the efficiency values over the energy range under consideration, obtained from GEANT4 based simulation, are found to be lower by $\sim 10 - 20$ %.

CHAPTER 5

Results

The electron impact production cross sections and ionization cross sections, obtained from the experimental work performed in the thesis, are presented in this chapter. The experimental results are compared with the theoretical estimates in order to understand their merits and demerits in predicting the L X-ray cross sections for the studied elements and electron energy regime. Before presenting the results, we would like to impress upon the work done by other groups so that the results obtained in this work can be established in view of the earlier published results. Although extensively available for K shell, the electron impact ionization studies are scarce for the L shell and other outer shells, due to various inherent complexity in obtaining those cross sections as outlined in the introduction chapter. We have compared our data with the recent results and have ignored the results which were reported earlier than 1980, as it should be noted that, earlier studies ignored Coster-Kronig transitions while obtaining ionization cross sections from the x-ray yields (for example see Ref. [34, 73]).

In the case of Gold, our data is compared with the recent measurement of Wu et al. [17] and Campos et al. [59] and earlier measurements of Shima et al. [69]

and Schneider et al. [75]. Wu et al. have measured the L_α and L_β production cross sections for Gold. In the paper by Shima et al. they have presented the L_α, L_β and L_γ production cross sections in the energy range $12-25$ keV, but they have obtained the $L3$ ionization cross section in the range of $12.26-13.6$ keV only, which is out of our energy range of study. In fact for all the three elements, for which ionization cross sections are obtained in this work *viz,* Au, Pb, and Th, no other measurements of ionization cross sections are available in the energy range of interest, except for L_2 and L_3 subshell of Gold. The L_3 subshell ionization cross sections of Gold are reported by Schneider et al. along with a few other researchers. Schneider et al. have reported ionization cross sections in the energy range of 12.3 to 75 keV. Production cross sections for Lead are compared with the measurements of Moy et al. [19] and Wu et al. [18]. Both the groups have measured the production cross sections for L_α and L_β lines. The measurements of Wu et al. are reported for the energy range of $16-40$ keV while Moy et al. have reported their results for the energy range of $13-38$ keV. In the case of Bismuth, the studies done by Wu et al. [72] are available for L_α and L_β lines in the range of $17-40$ keV. No measurement of production cross sections in Thorium and Uranium are reported so far in the published form. Therefore, our evaluation of production/ionization cross sections in Thorium and Uranium are reported for the first time in this thesis. Thorium results are already published from our group/collaboration [20].

Our experimental results are compared with two different theoretical estimates based on two different formalisms: (1) MRBEB theory and (2) DWBA formalism. The DWBA theory based analytical formulas for calculating the ionization cross sections for electron or positron impact is given by Bote et al. [4] and are incorporated in the PENELOPE code. The DWBA estimates presented here are obtained from the PENELOPE code, while the MRBEB results are provided by the research group of Prof. Santos (FCT, Portugal). Details of the MRBEB theory along with DWBA

formalism is provided in detail in chapter 2. Theoretical L shell ionization cross sections, calculated this way, are compared with the L-shell ionization cross sections obtained from the production cross sections as detailed in Section 3.9. Precise and accurate knowledge of the relevant relaxation parameters are important in extracting the relevant ionization cross sections.

It is important to note that both the theories described above predict ionization cross sections, whereas we have obtained production cross sections from the experiments. For the comparison of experimental findings with the theoretical estimates, experimental production cross sections needs to be converted into ionization cross sections or vice-versa. This conversion process involves relaxation parameters, which themselves can have uncertainties up to $\lesssim 50\%$. To make the comparison meaningful, it is important to eliminate or separate the effect arising due to the errors in the relaxation parameters. In the next section of the thesis, relaxation parameter dependence of the ionization cross sections, extracted from the production cross sections, is explored.

5.1 Production Cross Section

All the experimentally obtained L x-ray production cross sections values are shown in the Figures 5.1, 5.2 and 5.3. Along with our experimental data, results from other researcher's are also shown in the same graphs wherever available. Corresponding theoretical estimates, based on the DWBA and the MRBEB theories are also plotted on the same graphs. The shaded regions around the DWBA estimates in the graphs indicate the predicted uncertainty bands arising from the uncertainties in the relaxation parameters. The uncertainty, recommended by Campbell [129] for the various relaxation parameters which we have adapted in this work, is listed in Table 5.1. Uncertainty band for MRBEB is not shown to keep the data visualization

Parameters	ω_1	ω_2	ω_3	f_{12}	f_{13}	f_{23}	Γ,s
% Error	20	5	5	50	15	10	10

Table 5.1: Adopted errors in relaxation parameters.

clearer. The production cross sections values obtained in this work are tabulated in Appendix B. The overall uncertainties in the measured L X-rays production cross sections are $\sim 11-12\%$. Major contributions to the uncertainties come from the detector efficiency (10%), beam current measurement ($\sim 3\%$) and the target thickness measurement ($\sim 5\%$). Detailed discussions on measurements for each of the elements studied in this thesis are given below.

Lead

The L X-ray production cross sections of Lead are plotted in the Figure 5.1a. The L_α and L_β X-ray production cross sections, based on measurements done by Wu et al.[18] and Moy et al.[19], are shown in the same graph. Out of these two sets of measurements, results of Wu et al. are in good agreement with our corresponding results except at the two lowest energies i.e. 16 and 18 keV, where our experimental production cross sections drop very quickly when compared with other data and theoretical trend. The production cross sections quoted by Moy et al. for L_α transitions are higher than our results by about $10-15\%$, and also those are higher than the results predicted by DWBA theory. However the results remain within the uncertainty band. The DWBA estimations for the L_α production cross sections are in good agreement with ours and those obtained by Wu et al., while the estimates from MRBEB are in better agreement with the data of Moy et al. The DWBA estimates for L_β transitions of Lead overpredict the production cross sections across the energy range of interest, but the estimates agree with the experimental results within the predicted uncertainty band. Considering the systematic trend in

the experimental data over the energy range, the results of Wu et al.[18] are in better agreement within the uncertainty band. Our results for L_β are systematically on the lower end of the predicted band. The MRBEB theory predicts larger production cross sections for all the lines, with values grazing the upper end of the predicted uncertainty band of DWBA estimates. For L_γ transitions, both the theories predict higher cross sections compared to experimental data by more than 30%.

Bismuth

For Bismuth, the experimental results are shown in Figure 5.1b, along with the available results of Wu et. al [72] for L_α and L_β lines. Measurements of Wu et al. are in good agreement with our L_α and L_β x-ray production cross sections. The agreement between two data set is true even at the lower energies, unlike in the case of Lead. The DWBA estimations for the L_α and L_β production cross sections are in good agreement with both the experimental data sets. Although the L_β production cross sections from our experiment are slightly lower than the DWBA predictions and the experimental data of Wu et al., they are well within the uncertainty band and the overall agreement between theory and experiment is better than in the case of Pb. However, the situation is similar to that of Lead for the experimental L_γ cross sections, viz. those are lower than the theoretical estimates by about $30-50\%$. It should be noted that in the case of Bismuth, the MRBEB predicts much higher production cross sections as compared to those in case of Lead. For Bismuth, the MRBEB predictions are almost 2 times of DWBA cross sections, while the same factor is about 1.3 to 1.5 in case of Lead.

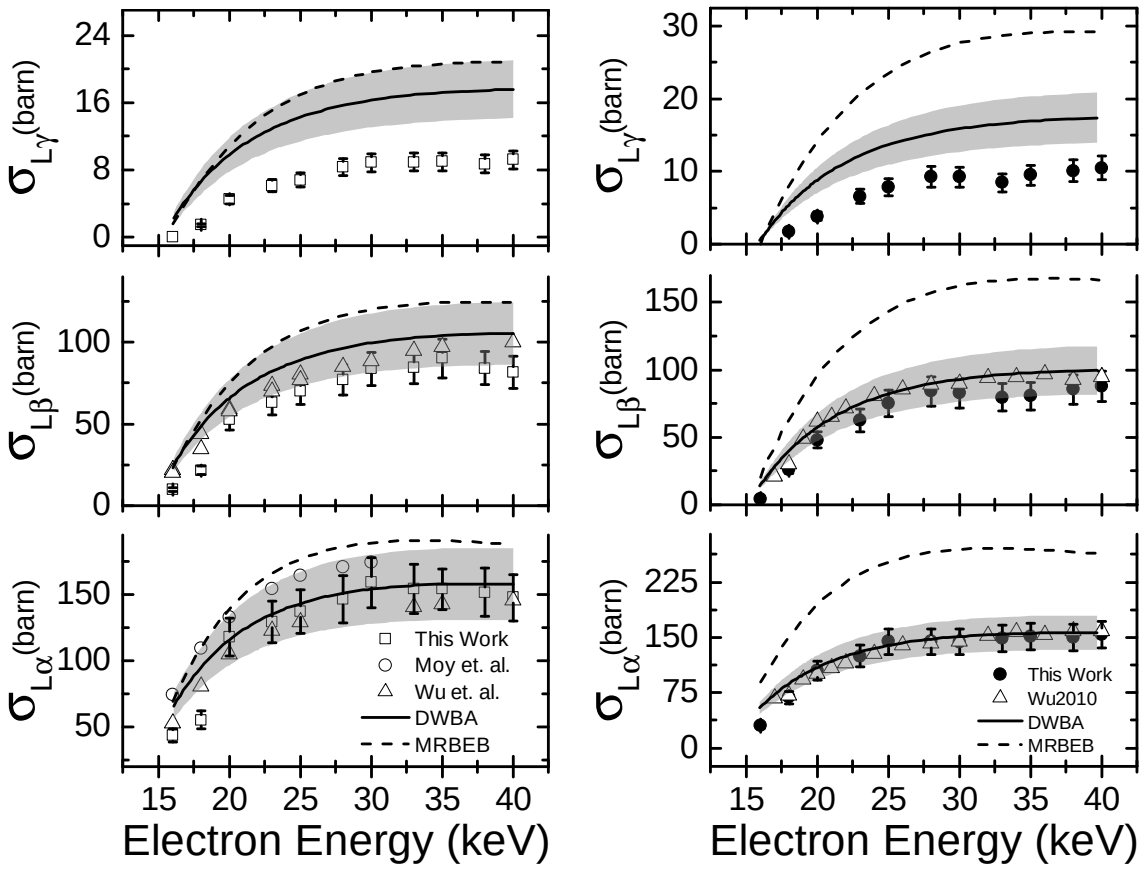

(a) Lead (b) Bismuth

Figure 5.1: X-ray production cross section for L_α, L_β and L_γ lines of (a) Pb and (b) Bi. Theoretical curves for DWBA [16] and MRBEB [120] are obtained using relaxation parameters from [129] and [130]. The shaded area is due to the uncertainty(see Table 5.1) in the adopted relaxation parameters.

Throium and Uranium

Experimental L x-ray production cross sections for Thorium and Uranium are not reported by any other research group. Therefore, in the Figures 5.2b and 5.2a only theoretical results are plotted along with our experimental data. Also in the case of Uranium, only L_α and L_β data could be obtained for a few electron projectile energy values due to our experimental limitations. It should be noted that the data presented here incorporates the X-ray yield corrections occurring due to the presence of Aluminum backing in these two targets. L_α production cross sections are in good

agreement with the DWBA theory for both the elements, especially above 30 keV projectile energy. Unlike the case of other three elements studied, L_β production cross sections in the case of Thorium and Uranium, are lower than the cross sections as predicted by DWBA theory. The discrepancy between DWBA theory and experiment is much higher for the Uranium L_β transitions than for the corresponding ones in Thorium. The experimental L_γ production cross sections obtained in the case of Thorium is lower than the production cross sections obtained using DWBA and MRBEB theories by about $50 - 70\%$.

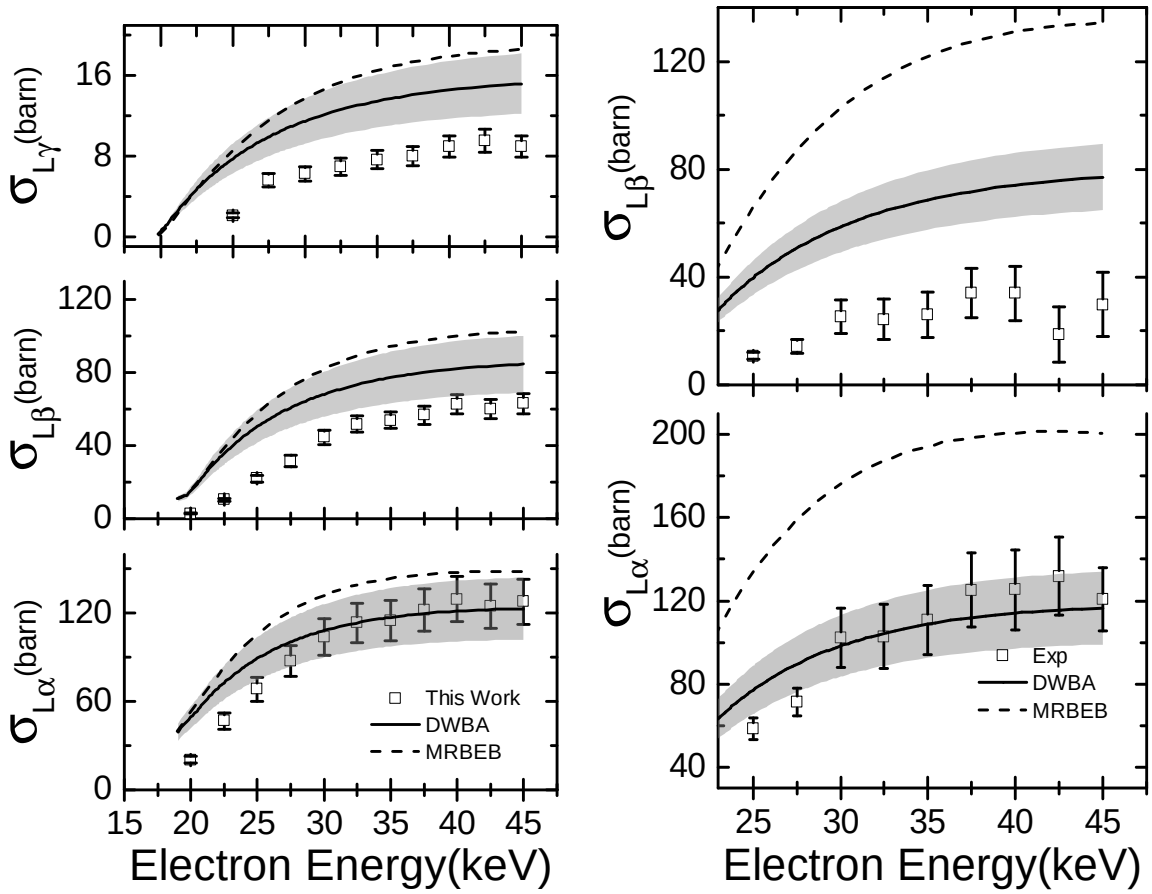

(a) Thorium (b) Uranium

Figure 5.2: Production cross section of (a) Th (L_α, L_β and L_γ) and (b) U (L_α and L_β). Theoretical curves for DWBA [16] and MRBEB [120] are obtained using relaxation parameters from [129] and [130]. The shaded area is due to the uncertainty(see Table 5.1) in the adopted relaxation parameters.

Gold

The L X-ray production cross sections, obtained in this experiment and also those measured by Wu et al. [17], Campos et al. [59] and Shima et al. [69], are plotted in the Figure. 5.3a, along with the theoretical cross sections. It can be seen that the MRBEB and DWBA predictions agree with experimental results for L_α and L_β up to $E \sim 15$ keV. For $E > 15$ keV, DWBA results are in good agreement with all four experiments for L_α, but the MRBEB theory overpredicts the L_α cross sections in this energy domain. For the L_β transitions, the DWBA results are in reasonable agreement with the experimental results for $15 < E < 25$ keV, but overpredicts by $\sim 30\%$ at higher energies. Unfortunately, our results are the only one in this energy domain. MRBEB overpredicts the L_β cross sections for $E > 15$ keV. Both the theories overpredict the L_γ cross sections over the entire electron kinetic energy range, though the experimental results of Shima et al. match with DWBA within the error bars of their data, which are relatively larger than the error bars in the present experiment.

For all the elements studied it can be seen that, although the experimental L_α production cross sections are explained very well by the DWBA theory, the experimental production cross sections for lower projectile energies are well below the theoretical estimates. The differences are higher in the case of Thorium and Uranium and are minimum in case of Gold. From the simulation, it can be seen (see Figure 4.4), that the projectile electron losses more energy, in Gold and Bismuth target films than in the other elements over the lower energy range. Considering the highest energy loss of projectile in Gold and Bismuth for the used experimental target at the lowest impact energies, one should expect that the discrepancy between experiment and theory should be higher for Gold and Bismuth at lower energies. But the obtained results are opposite to the expectations and are certainly baffling. The reason for differences between theory and experiment in the case of L_β and L_γ lines

can be quite different and an explanation is attempted in the next section.

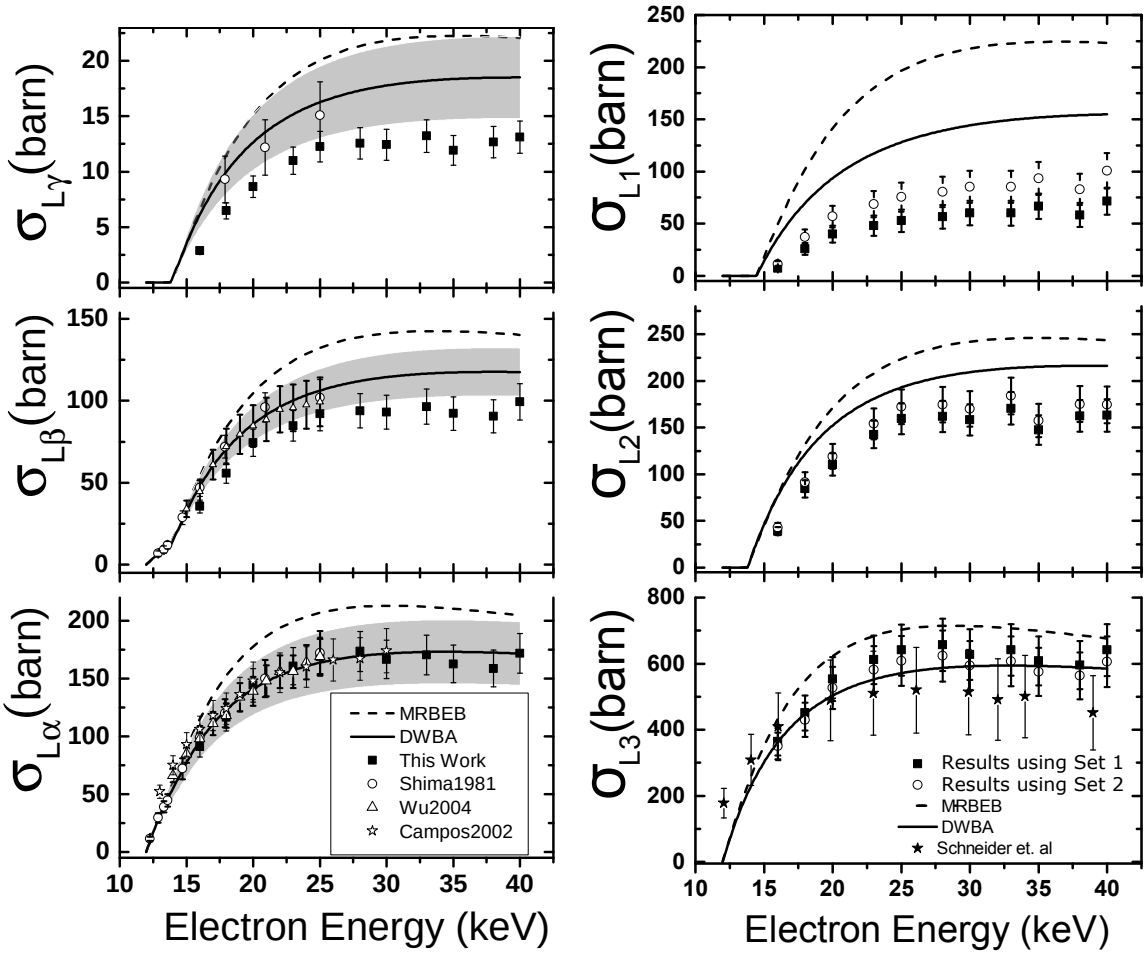

(a) Production cross sections of Gold (b) Ionization cross sections of Gold.

Figure 5.3: (a) X-ray production cross section for L_α, L_β and L_γ lines of Au. Theoretical curves for DWBA [16] and MRBEB [120] are obtained using relaxation parameters from [129] and [130]. The shaded area is due to the uncertainty(see Table 5.1) in the adopted relaxation parameters.(b) L_1, L_2 and L_3 subshell Ionization cross- sections for Au. Experimental Ionization cross sections are obtained using two sets of relaxation parameters: set 1 consists of relaxation parameters from [129] and [130] and set 2 consists of relaxation parameters from [141] and [137]

5.2 Ionization Cross Sections

The discrepancy between theory and experiment can be further understood by looking at the L_1, L_2, and L_3 ionization cross sections extracted from our experimental

data. The process of extracting ionization cross sections from the experimentally obtained production cross sections is described in detail in the data analysis section of chapter 2. The results, along with those from the MRBEB and DWBA calculations, are plotted in the Figures. 5.3 and 5.4, while the cross section values are tabulated in Appendix B along with the accounted errors. Due to propagation of errors as per the equations used to obtain the ionization cross sections from experimental production cross sections, the uncertainties in the corresponding ionization cross sections are $\sim 20\%$, and when the uncertainties in the relaxation parameters within their quoted ranges are included, the errors in the ionization cross sections become larger than $\sim 30\%$.

In this section, the results obtained for all the three elements are presented. The only other result shown along with our results is that of Schneider et al. [75] for L_3 subshell of Gold. As no other experimental result is available in the energy range of interest for Lead and Thorium, our results are only shown in the graph and are compared with the available theory. The ionization cross sections are obtained using relaxation parameters from Campbell [129] and Campbell and Wong [130] for Lead and Thorium. The procedure followed to obtain the ionization cross sections from production cross sections is outlined in detail in the data analysis section of chapter 2. To explore the effect of variation in relaxation parameters, the ionization cross sections for Gold are obtained with two different sets of relaxation parameter.

Lead

The ionization cross sections of Lead obtained from our experiment, are plotted in Figure 5.1a along with the theoretical results obtained from MRBEB and DWBA theory. It can be seen that, L_3 ionization cross sections agree very well with the DWBA theory, specifically for the energies $E > 1.35U$, where U is the ionization

threshold for the L_3 subshell. In the case of L_2 and L_1 subshells, the agreement between theory and experiment is not at all satisfactory. In both the elements studied in our experiment, the L_2 and L_1 subshell ionization cross sections at near-threshold energies are smaller than the DWBA estimates by $\sim 30-50\%$. The MRBEB theory predicts $\sim 20-30\%$ higher ionization cross sections than the DWBA theory for L_2 and L_3 subshells and up to 80% higher for L_1 subshell.

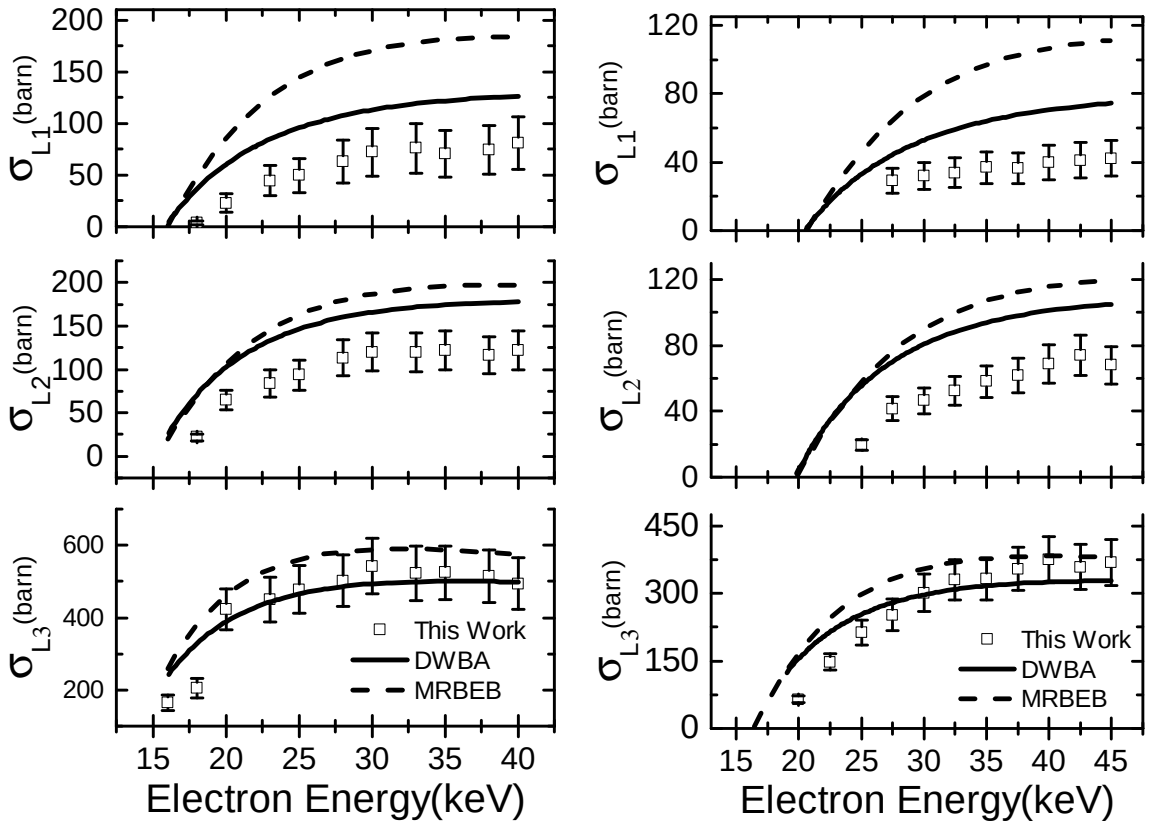

(a) Lead (b) Thorium

Figure 5.4: L_1, L_2 and L_3 subshell ionization cross sections of (a) Lead and (b) Thorium. Experimental values are obtained using relaxation parameters from [129] and [130]. Theoretical values for DWBA [16] is shown by solid curved while for and MRBEB [120] is shown by dashed curved.

Thorium

Similar to the case of Lead, L_3 subshell ionization cross sections are explained well by the DWBA theory as shown in the Figure 5.4b. The agreement between theory

and experiment is better for the higher energies especially above $1.35U$. While the L_2 and L_1 subshell experimental ionization cross sections are not at all in agreement with the theoretical estimations. The disagreement between MRBEB calculations and experiment is higher than between DWBA estimates and the experimental results.

For Thorium, the L_β line was resolved into L_{β_1} and L_{β_2} peaks in the obtained spectra (see Figure 3.12). This fact, is used to our advantage, to cross-check and verify the obtained ionization cross sections. Attempts were made to extract the L_1 and L_2 ionization cross sections from the L_{β_1} and L_{β_2} production cross sections using the equations 5.1a and 5.1b [69].

$$\begin{aligned}\sigma_{(L_{\beta_1}+L_{\beta_5}+L_{\beta_3})} &= S_{\beta_5,3}\omega_3\sigma_{L_3} + [S_{\beta_1,2}\omega_2 + S_{\beta_5,3}\omega_3 f_{23}]\,\sigma_{L_2} \\ &\quad + [S_{\beta_1,2}f_{12}\omega_2 + S_{\beta_5,3}\omega_3(f_{13}+f_{12}f_{23}) + S_{\beta_3,1}\omega_1]\,\sigma_{L_1}, \quad (5.1a)\\ \sigma_{(L_{\beta_2}+L_{\beta_6}+L_{\beta_4})} &= S_{\beta_{2+6},3}\omega_3\sigma_{L_3} + S_{\beta_{2+6},3}\omega_3 f_{23}\sigma_{L_2} \\ &\quad + \left[S_{\beta_{2+6},3}\omega_3(f_{13}+f_{12}f_{23}) + S_{\beta_4,1}\omega_1\right]\sigma_{L_1} \quad (5.1b)\end{aligned}$$

where the symbols used have the usual meaning, as explained for equations (3.8a to 3.8d). The same set of atomic relaxation parameters was used to get the ionization cross sections. Ionization cross sections for L_3 subshell, needed as input, were obtained from the DWBA estimates. A good reason for using the theoretical estimates for L_3 subshell is that the experimental results are found to be in reasonable agreement with theory (see Fig. 5.4b).

Ionization cross sections for L_1 and L_2 subshells were obtained for Thorium using two different set of equations; the first set as in case of Gold and Lead, L_α and L_γ production cross sections were used, while the second set uses L_β production cross sections and L_3 subshell ionization cross section. The comparison of results obtained is shown in Figure 5.5 along with DWBA results. It can be seen that the L_2 subshell ionization cross sections, obtained using different methods, are found to be

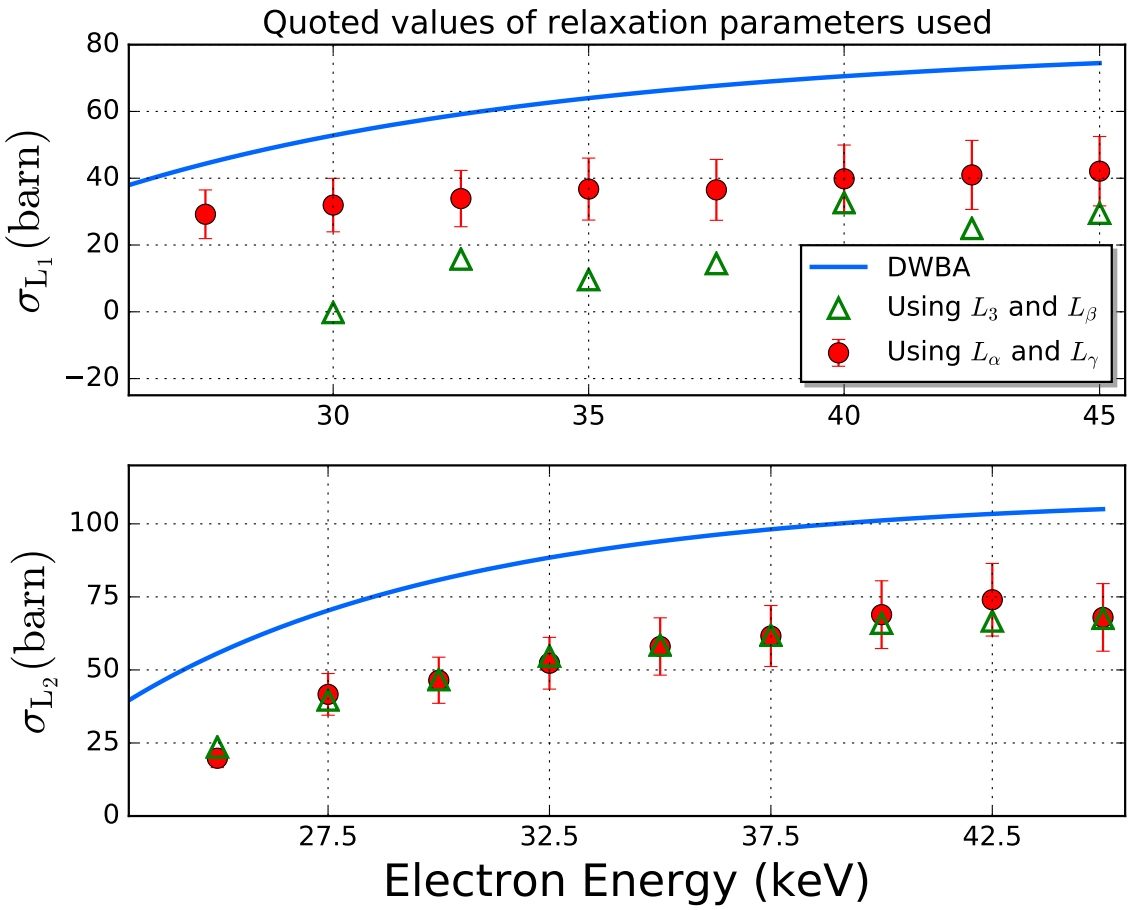

Figure 5.5: L_1 and L_2 subshell ionization cross section for Thorium. Circles are the ionization cross-sections obtained using σ_α and σ_γ, while triangles are the values obtained using L_{β_1} and L_{β_2}. These values are obtained using recommended values of relaxation parameters in [129] and [130]

in good agreement with each other. However, the calculated σ_{L_1} values were not at all consistent with each other. Especially at the low energies, the obtained ionization cross sections tends to shift towards the negative values due to smaller L_β production cross sections. Minor changes in the relaxation parameters within the allowed range of variation (see Ref. [129]) restores σ_{L_1} values to come closer to the previously obtained results (see Fig. 5.4b), without causing much deviation in σ_{L_2} values. For example, values shown in Figure 5.6 correspond to the ionization cross sections obtained using 10% reduction in radiation yield corresponding to $L_3 - M_5$ transition. This indicates the need for possible modification of the atomic relaxation parameters.

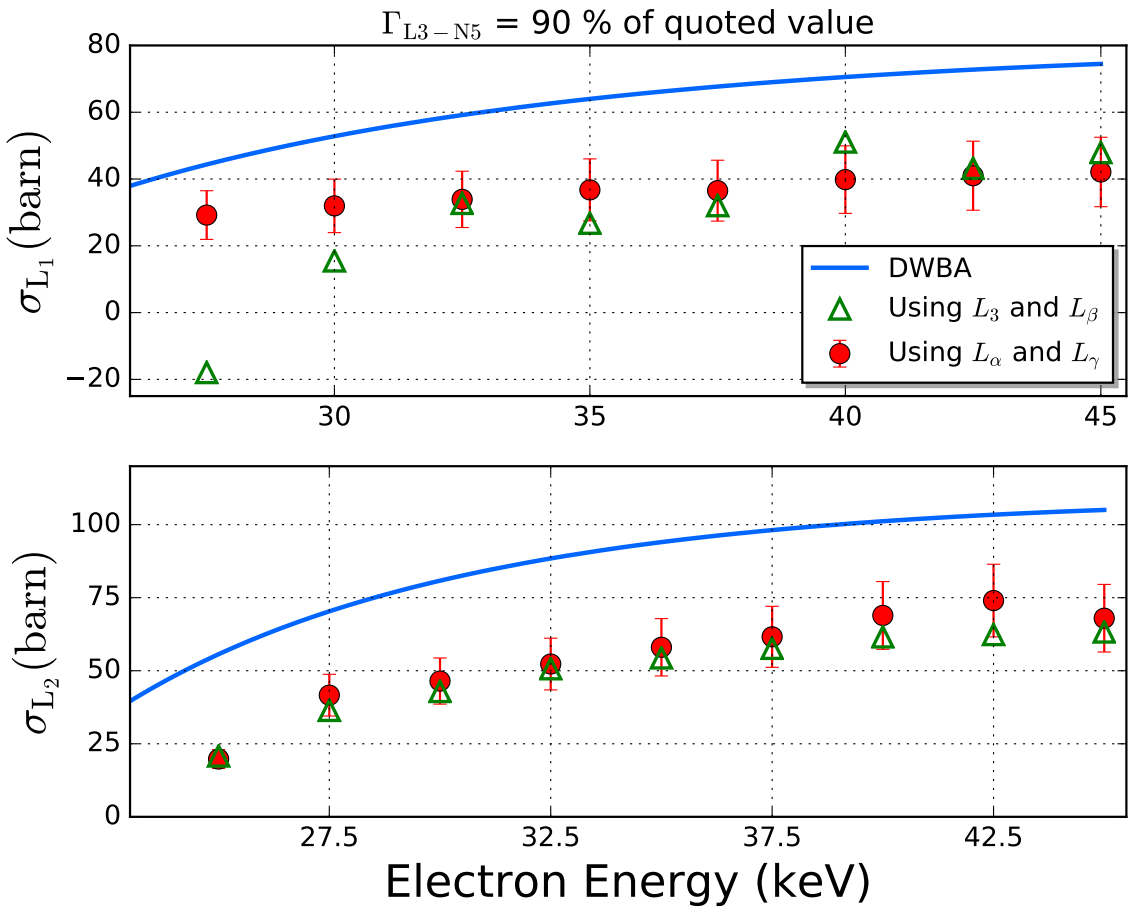

Figure 5.6: L_1 and L_2 subshell ionization cross section for Thorium. Circles are the ionization cross-sections obtained using σ_α and σ_γ, while triangles are the values obtained using L_{β_1} and L_{β_2}. These values are obtained using 10 % reduction in the recommended value of $\Gamma_{L_3-M_5}$ as compared with the Fig. 5.5

Gold

For a consistent comparison of the experimental results, including parameter dependence of ionization cross sections, the production cross sections of Gold are converted to ionization cross sections using two different sets of relaxation parameters. Out of these two sets of relaxation parameters, first set includes fluorescence yield and Coster-Kronig parameters from Campbell [129] and radiation yield from Campbell and Wong [130] while the second set is based on classical calculations of Scofield [137] (Radiation yields) and Krause [141] (fluorescence yield and Coster-

Kronig parameters). The results obtained are shown in Figure 5.3b, along with the DWBA and MRBEB estimates. For L_3 subshell, the available results of Schneider et al. are also plotted in the same graph. Schneider et al. have obtained the ionization cross sections from production cross sections using relaxation parameters of Scofield and Krause. From the graph, we can see that the ionization cross sections obtained by Schneider et al. are lower than that of our experimental results and also the DWBA theory. The results of Schneider et al. has larger error bars than our data. There is a reasonable agreement between both the theories and our experimental results for L_3 subshell, within the uncertainty limits. While the parameter dependent variation is $\sim$30% for σ_{L1}, it is relatively less ($\sim$10%) for σ_{L2} and σ_{L3} subshells. The 10% variation of ionization cross sections for two different sets of relaxation parameters is actually well within the error bar of experimental data itself. On the other hand, the discrepancy between experiment and both the theories appears to be the largest for L_1, and significant but smaller discrepancy for the DWBA than for the MRBEB formalism.

The large difference between L_1 subshell cross sections, for experimental results obtained with two different sets of parameters occur mainly due to large difference between ω_1 available from these two sets and not from the radiative yields. The difference between the values of ω_1 from these two sets is $\sim$ 17%. Although the error in ω_1 from the Cambell [129] is $\sim$ 20%, this difference makes the results obtained with fluorescence yield from Krause [141] agree better with the theory.

5.3 Discussion about Discrepancy Between Theory and Experiment

From our studies it is seen that for production cross sections of all the elements studied, excellent agreement is found between DWBA theory and experiment for L_α. While for L_β transitions, the results are mixed, i.e, good agreement for DWBA and experiment is observed for Pb, Au, and Bi but a poorer agreement is found for Th and U. While for L_γ, there is no agreement between theory and experiment for all the elements. Similarly, when the ionization cross sections are considered, it is found that the theory is able to explain the L_3 ionization cross sections very well for all elements but experimental results and theoretical estimates differ quite a bit for L_1 and L_2 subshells.

As the results differ for L_1 and L_2 subshells and not for the L_3 subshell ionization cross sections, we can conclude that the difference in theory and experiment for L_1 and L_2 sub-shell results may arise due to the relaxation parameters used in the estimation of this ionization cross sections. A direct indication of the results of relaxation parameter variation is given in Sec. 5.2 in connection with our attempt in extracting σ_{L_1} and σ_{L_2} for Thorium using two different combinations of production cross sections.

In order to obtain the L_1 subshell ionization cross sections for all the elements, following the procedure as described in the data analysis Section 3.9, we have used $\sigma_{L_{\gamma 236}}$. While calculating the σ_{L_1} from the corresponding $\sigma_{L_{\gamma 236}}$, the radiative yields $\Gamma_{\gamma_1}, \Gamma_{\gamma_6}, \Gamma_{\gamma_2}, \Gamma_{\gamma_3}$ and the fluorescence yield (ω_1) are used. Out of these five relaxation parameters, $\Gamma_{\gamma_2}, \Gamma_{\gamma_3}$ and ω_1 are associated with the relaxation of the vacancy created in the L_1 subshell, and the remaining parameters are associated with the vacancy in the L_2 subshell. Thus, our experimental findings i.e. discrepancies between theory and

experiment for L_γ and L_1 subshell indicate that the differences could be due to the poorly known relaxation parameters, specifically the relaxation parameters related to the L_1 subshell. It is worth mentioning here that in a review on theories of inner shell ionization by proton impact[140], the author has concluded that the radiative yield related to the L_1 subshell and the Coster- Kronig factors need to be re-evaluated and experimentally measured.

The L_2 subshell results are inconclusive due to the fact that the σ_{L_2}, obtained from $\sigma_{L_{\gamma_{1+5}}}$ is lower than the theoretical estimates by $30-50\%$, but the σ_{L_β} values, which have almost equal contribution from σ_{L_2} and σ_{L_3}, are explained reasonably well by the DWBA theory, not only for Pb, Au, and Bi but also for few other elements as observed by Varea et al. [102]. The problem becomes complicated with the observation of production cross sections of Th. The L_β results of Th, which are again lower than the estimated production cross sections, suggest that the problem with relaxation parameters might be playing a role in the discrepancy between theory and experiment.

The σ_{L_3} and σ_{L_α} results are explained very well by theory, not only for the Pb and Th but also for the other high Z elements[21, 102], indicating that the relaxation parameters related to L_3 subshell are consistent with the underlying theory and related experiments. Also it is important to note that the L_3 subshell ionization cross sections for handful of elements in the range from Phosphorus ($Z = 15$) to Uranium ($Z = 92$), measured either directly from electron energy loss spectroscopy (EELS) or indirectly by electron impact spanning energy range from near the ionization threshold to ~ 1 MeV, are found to agree reasonably well with the DWBA calculations following Bote et al.[16], as described in detail in Ref. [2]. The agreement is very limited especially at energies near the ionization threshold.

CHAPTER 6

Conclusion

The main results of this thesis have already been presented and discussed in the Chapters 4 and 5. In this chapter we shall give a brief summary of the outcome of the thesis, conclusions drawn from the results and the future scope of the work.

In course of this thesis work, an experimental set up involving an energy dispersive spectrometer was developed. The set up was successfully utilized to explore and characterize the inner shell ionization phenomena, specifically the L-shell ionization, resulting from electron impact at energies ranging from ionization threshold to $\sim 40-50$ keV. The exploration was targeted for heavy elements of interest involving Gold, Lead, Bismuth, Thorium and Uranium. Motivation for choosing the heavy elements for our studies are as follows. Firstly, the L-shell ionization phenomena in Thorium and Uranium were not studied at all prior to this thesis and results in Gold, Bismuth and Lead over this range of energies were either incomplete or in disagreement with existing theoretical predictions. Secondly, these results are valuable addition to the database which is used for the detection of heavy elements and quantify their contents by energy dispersive spectroscopy. Thirdly, it is important to investigate the agreement and discrepancy between the experimentally obtained

production cross sections and those estimated on the basis of established theories and models. It is important to point out that in carrying out the experiments, several stringent conditions were to be monitored and systematic effects were to be taken into account to extract the meaningful results. In this thesis work, detailed simulations of the electron impact and transport were done to achieve various ends, such as (a) estimation of the effect of finite thickness of the thin film media for electron traverse; (b) electron backscattering contribution caused by the presence of backing materials in the targeted media; and (c) establish a relatively new method of determination of X-ray detection efficiency of SDD detectors using bremsstrahlung radiation caused by electron impact. The simulation was done using the general purpose Monte Carlo codes PENELOPE and GEANT4. Using the same simulation packages, the bremsstrahlung spectra in thick Carbon films were obtained which were used to obtain the efficiency of the X-ray detectors. Using this procedure, the efficiency of the detector could be obtained to very low energies down to 1 keV.

Using this experimental setup, we have measured the L-shell X-ray production cross sections for Gold, Lead, Bismuth, Thorium and Uranium over the range of electron impact energies of $16 - 45$ keV. In case of Gold, Lead and Thorium, we have also obtained the ionization cross sections from the experimentally obtained production cross sections. In case of Thorium and Uranium, the experiment was performed with the targets backed by thick Aluminum films. For these two elements, the effect due to the presence of backing was corrected by the Monte Carlo simulation. It was also verified from simulation, that no significant loss of projectile energy has occurred inside the targets and also no multiple collision events have taken place inside the target elements (See Figures 4.3)

The X-ray production cross sections obtained in this work are in accordance with the experimental results for L_α and L_β X-ray transitions published prior to this

thesis work for some of the elements (See Figures 5.1 , 5.2and 5.3). For L_γ transitions no result is available in the energy range of interest, except for Gold. For L_γ transition of Gold, the production cross sections obtained by other experimental group are in agreement with our results within the uncertainty limits (See Figure 5.3).

We have compared our experimental results with two different theoretical models *viz.* MRBEB and DWBA. As described in Section 2.5.1, although MRBEB is able to reproduce reliable K shell production cross sections, it is seen that in general MRBEB predicts higher cross sections for all the X-ray lines in all the elements studied so far. In comparison with MRBEB, DWBA is more successful in predicting the production cross sections for all the elements for L_α and L_β transitions. However, DWBA predicts systematically larger cross sections for the L_γ transitions.

The ionization cross sections predicted by MRBEB theory are also found to be larger than the experimental results for all the three subshells *viz.* L_1, L_2, L_3 for the elements studied in the thesis. The ionization cross sections of L_3 subshell predicted by DWBA theory explains the experimental results very well but over-predicts the ionization cross sections for L_2 and L_1 subshells. The difference between cross sections obtained from theory and experiment is larger for L_1 subshell than for the L_2 subshell.

In the Section 3.7, the procedure for obtaining the ionization cross sections from the production cross sections and vice versa is outlined, and it can be seen that the experimentally obtained ionization cross sections or theoretically obtained production cross sections highly depend on the relaxation parameters used in the process. Therefore, the observed discrepancy between theory and experiment for L_γ production cross sections and L_1 and L_2 ionization cross sections cannot solely be attributed to inadequacy of theory.

Dependence of cross sections on the relaxation parameters was investigated by

extracting the ionization cross sections of Gold with two sets of relaxation parameters (See Figure 5.3). It was found that although ionization cross sections, obtained with the relaxation parameters of Scofield and Krause [136, 141] are in better agreement with the theory, the difference between ionization cross sections obtained usings these two sets of relaxation parameters is within 10%. The discrepancy between theory and experiment is further investigated using the L_β transition in Thorium. In case of Thorium, the L_β line is resolved into its two major constituents i.e, L_{β_1} and L_{β_2} lines. Using the resolved L_β peak of Thorium, the ionization cross sections in case of Thorium is obtained using two different sets of production cross sections. From our study of relaxation parameter dependence it is evident that the discrepancy between theory and experiment may arise due to errors in fixing some of the relaxation parameters (See Section 5.2). Specifically it can be said that the relaxation parameters related to the L_1 sub-shell needs to be carefully re-evaluated and re-measured.

From our study we would like to conclude that, the discrepancy between theory and experiment may arise due to errors in fixing some of the relaxation parameters. It is, therefore, important to perform measurements, which require a minimum number of relaxation parameters for extracting ionization cross sections from the experimental data. Clearly, more measurements with wavelength dispersive spectrometer should be done where even subshell specific transitions can be resolved, thereby reducing the dependence on the relaxation parameters. Also, very few measurements exist for the L_γ X-ray production cross sections of high Z elements. As L_γ transitions relate to the L_1 and L_2 subshells, it is important to perform these measurements, specifically in view of the new calculations performed by Pindzola [155, 156] by the inclusion of the retarded electromagnetic potential, which significantly changes the ionization cross sections of the L_1 and L_2 subshells. In addition, the scope of research can be extended further by wavelength dispersive spectroscopy to obtain the M X-ray production cross sections, which is largely an unexplored area with practical applications.

APPENDIX A

Relaxation Parameters

The list of all the used atomic relaxation parameters is given here. These relaxation parameters are mainly taken from the compilations of Campbell [129], Campbell and Wong [130], Krause [141] and Scofield [136].

Fluorescence Yields and Coster-Kronig Parameters

Parameter	ω_1	ω_2	ω_3	f_{12}	f_{13}	f_{23}
Element						
Pb	0.1	0.397	0.343	0.064	0.61	0.119
Bi	0.11	0.411	0.353	0.064	0.62	0.117
Th	0.17	0.503	0.424	0.06	0.66	0.103
U	0.19	0.506	0.444	0.035	0.67	0.14
Au (Campbell)	0.13	0.358	0.313	0.07	0.58	0.125
Au(Krause.)	0.107	0.334	0.32	0.14	0.53	0.122

Table A.1: Fluorescence yield and Coster-Kronig parameters

Radiative Yields

Radiative yields are given in the unit of $eV/\hbar$ with $1\ eV/\hbar = 1/27.21 a.u.$ The probability of decay of a vacancy through a particular transition is given as the ratio of radiative yield of that particular transition to the total radiative yield of the shell. For example the decay of vacancy in L_3 subshell by l_{α_1} transition is given as $\Gamma_{M_5 \to L_3}/\Gamma_{L_3}$

			Radiative yield ($\Gamma_{i,j}s$)			
Vacant Shell	Transition		Lead	Bismuth	Thorium	Uranium
L3	l_l	$\Gamma_{M_1 \to L_3}$	0.0851	0.0911	0.1467	0.1672
	l_{α_2}	$\Gamma_{M_4 \to L_3}$	0.1646	0.174	0.2502	0.2758
	l_{α_1}	$\Gamma_{M_5 \to L_3}$	1.447	1.527	2.195	2.418
	l_{β_6}	$\Gamma_{N_1 \to L_3}$	0.0213	0.0229	0.0377	0.0431
	$l_{\beta_{15}}$	$\Gamma_{N_4 \to L_3}$	0.0324	0.0345	0.0519	0.058
	l_{β_2}	$\Gamma_{N_5 \to L_3}$	0.2933	0.3122	0.474	0.5313
	l_{β_7}	$\Gamma_{O_1 \to L_3}$	0.0045	0.005	0.0093	0.0108
	l_{β_5}	$\Gamma_{O_{45} \to L_3}$	0.0427	0.0049	0.0998	0.115
	Total	Γ_3	2.0909	2.1716	3.2646	3.6192
L2	l_η	$\Gamma_{M_1 \to L_2}$	0.0521	0.0555	0.0837	0.0938
	l_{β_1}	$\Gamma_{M_4 \to L_2}$	1.884	1.999	2.951	3.28
	l_{γ_5}	$\Gamma_{N_1 \to L_2}$	0.0136	0.0146	0.0228	0.0258
	l_{γ_1}	$\Gamma_{N_4 \to L_2}$	0.4048	0.4336	0.6856	0.7763
	l_{γ_8}	$\Gamma_{O_1 \to L_2}$	0.0029	0.0032	0.0056	0.0065
	l_{γ_6}	$\Gamma_{O_4 \to L_2}$	0.0548	0.0626	0.1335	0.1559
	Total	Γ_2	2.4122	2.5685	3.8822	4.3383
L1	l_{β_4}	$\Gamma_{M_2 \to L_1}$	0.4568	0.4875	0.7568	0.8559
	l_{β_3}	$\Gamma_{M_3 \to L_1}$	0.5015	0.5242	0.6968	0.7482
	l_{γ_2}	$\Gamma_{N_2 \to L_1}$	0.1201	0.129	0.2075	0.2363
	l_{γ_3}	$\Gamma_{N_3 \to L_1}$	0.1458	0.154	0.2187	0.2393
	$l_{\gamma_{44'}}$	$\Gamma_{O_{23} \to L_1}$	0.0524	0.0572	0.101	0.1156
	Total	Γ_1	1.2766	1.3519	1.9808	2.1953

Table A.2: Radiative Yields from Campbell and Wong [130]

Vacant Shell	Transition		Radiative yield ($\Gamma_{i,j}s$)	
			Cambell et. al[130]	Scofield[136]
L3	l_l	$\Gamma_{M_1 \to L_3}$	0.0686	0.068
	l_{α_2}	$\Gamma_{M_4 \to L_3}$	0.1389	0.1377
	l_{α_1}	$\Gamma_{M_5 \to L_3}$	1.221	1.214
	l_{β_6}	$\Gamma_{N_1 \to L_3}$	0.017	0.0166
	$l_{\beta_{15}}$	$\Gamma_{N_4 \to L_3}$	0.0268	0.0252
	l_{β_2}	$\Gamma_{N_5 \to L_3}$	0.2412	0.2267
	l_{β_7}	$\Gamma_{O_1 \to L_3}$	0.0034	0.0033
	l_{β_5}	$\Gamma_{O_{45} \to L_3}$	0.0271	0.0225
	Total		1.744	1.714
L2	l_η	$\Gamma_{M_1 \to L_2}$	0.0432	0.0423
	l_{β_1}	$\Gamma_{M_4 \to L_2}$	1.574	1.565
	l_{γ_5}	$\Gamma_{N_1 \to L_2}$	0.0111	0.0108
	l_{γ_1}	$\Gamma_{N_4 \to L_2}$	0.3288	0.309
	l_{γ_8}	$\Gamma_{O_1 \to L_2}$	0.0022	0.0022
	l_{γ_6}	$\Gamma_{O_4 \to L_2}$	0.0347	0.0291
	Total		1.994	1.9584
L1	l_{β_4}	$\Gamma_{M_2 \to L_1}$	0.3745	0.373
	l_{β_3}	$\Gamma_{M_3 \to L_1}$	0.4339	0.43
	l_{γ_2}	$\Gamma_{N_2 \to L_1}$	0.097	0.0943
	l_{γ_3}	$\Gamma_{N_3 \to L_1}$	0.1226	0.1173
	$l_{\gamma_{44'}}$	$\Gamma_{O_{23} \to L_1}$	0.0391	0.0169
	Total		1.0671	1.0315

Table A.3: Radiative Yields for Gold

APPENDIX B

Tables of Cross-Sections

	Production Cross section			Ionization cross section		
Energy (KeV)	L_α (barn)	L_β (barn)	L_γ (barn)	L_1 (barn)	L_2 (barn)	L_3 (barn)
16	91.1(9.1)	35.5(4.0)	2.9(0.3)	7.3(2.2)	39.0(4.4)	364.2(41.6)
18	116.3(11.6)	55.8(6.2)	6.5(0.7)	25.7(5.7)	84.5(9.3)	450.6(53.1)
20	144.2(14.4)	74.4(8.3)	8.6(1.0)	39.9(8.0)	110.5(11.9)	553.5(65.9)
23	160.6(16.1)	84.7(9.4)	11.0(1.2)	48.1(9.7)	142.6(14.6)	611.9(73.5)
25	168.9(16.9)	91.9(10.2)	12.3(1.4)	52.9(10.7)	159.5(16.4)	641.1(77.3)
28	173.4(17.3)	93.9(10.5)	12.6(1.4)	56.5(11.3)	161.9(16.8)	657.1(79.4)
30	166.6(16.7)	93.0(10.4)	12.4(1.4)	60.1(11.6)	158.2(16.7)	627.3(76.3)
33	170.3(17.0)	96.4(10.7)	13.2(1.5)	60.1(11.8)	170.5(17.4)	641.1(78.0)
35	162.6(16.3)	92.2(10.3)	11.9(1.3)	66.6(12.0)	147.6(15.8)	608.4(74.5)
38	158.6(15.9)	90.5(10.1)	12.7(1.4)	58.3(11.5)	162.5(17.0)	595.4(72.7)
40	171.7(17.2)	99.3(11.1)	13.1(1.5)	71.6(13.0)	163.1(17.4)	641.1(78.7)

Table B.1: Experimental Production and Ionization cross sections of Gold. Ionization cross sections are obtained using relaxation parameter [129, 130]

	Production cross section			Ionization cross section		
Energy (KeV)	L_α (barn)	L_β (barn)	L_γ (barn)	L_1 (barn)	L_2 (barn)	L_3 (barn)
16	43.5(5.2)	9.9(1.2)	..	..	..	164.5(20.6)
18	55.3(6.7)	21.7(2.6)	1.4(0.2)	3.9(2.2)	21.9(4.0)	204.4(26.3)
20	117.7(14.2)	52.6(6.4)	4.5(0.5)	22.8(8.7)	64.6(11.6)	423.7(56.1)
23	129.1(15.6)	63.2(7.6)	6.1(0.7)	44.6(14.7)	84.0(15.4)	451.0(62.0)
25	137.3(16.6)	70.1(8.5)	6.8(0.8)	49.7(16.4)	93.7(17.2)	477.6(66.0)
28	146.6(17.7)	76.8(9.3)	8.3(1.0)	63.4(20.6)	113.4(20.7)	502.0(70.8)
30	159.0(19.2)	83.8(10.1)	8.9(1.1)	72.3(23.1)	119.9(22.1)	542.6(76.8)
33	154.3(18.6)	84.8(10.2)	9.0(1.1)	76.1(23.9)	119.8(22.1)	522.6(74.7)
35	154.0(18.1)	90.2(10.9)	9.0(1.1)	70.4(22.6)	121.7(22.2)	524.6(74.4)
38	151.6(18.3)	84.0(10.1)	8.7(1.1)	74.6(23.4)	116.4(21.6)	513.8(73.4)
40	147.5(17.8)	81.6(9.8)	9.2(1.1)	80.9(25.0)	121.9(22.1)	493.8(71.8)

Table B.2: Experimental Production and Ionization cross sections of Lead.

	Production cross section			Ionization cross section		
Energy (KeV)	L_α (barn)	L_β (barn)	L_γ (barn)	L_1 (barn)	L_2 (barn)	L_3 (barn)
20	20.5(2.0)	02.8(0.3)	..	..	..	064.6(8.0)
22.5	46.8(5.6)	10.3(1.0)	..	..	..	147.5(18.4)
25	68.2(8.1)	21.9(2.0)	2.1(0.3)	..	19.8(3.2)	213.0(26.8)
27.5	87.6(10.5)	31.5(3.1)	5.6(0.7)	29.2(7.3)	41.6(7.1)	252.2(34.7)
30	103.8(12.5)	44.6(3.9)	6.2(0.8)	32.0(8.0)	46.5(7.9)	301.1(41.1)
32.5	113.4(13.6)	51.7(4.5)	6.9(0.8)	33.9(8.4)	52.3(8.9)	329.2(44.8)
35	114.9(13.8)	53.9(4.7)	7.7(0.9)	36.8(9.3)	58.0(9.8)	331.7(45.5)
37.5	122.1(14.6)	56.7(5.0)	8.0(1.0)	36.5(9.1)	61.6(10.4)	354.0(48.3)
40	129.5(15.5)	62.6(5.4)	8.9(1.1)	39.8(10.1)	68.9(11.6)	374.5(51.3)
42.5	124.9(15.0)	59.8(5.3)	9.5(1.2)	41.0(10.3)	74.0(12.4)	358.5(49.5)
45	127.9(15.3)	62.9(5.5)	8.9(1.1)	42.1(10.4)	68.0(11.6)	368.0(50.6)

Table B.3: Experimental Production and Ionization cross sections of Thorium.

	Bismuth				Uranium	
Energy (KeV)	L_α (barn)	L_β (barn)	L_γ (barn)	*Energy* (KeV)	L_α (barn)	L_β (barn)
16	030.0(03.6)	04.4(0.6)	–	25	058.5(05.2)	10.8(01.2)
18	068.2(08.2)	26.3(03.4)	1.7(0.3)	27.5	071.3(06.7)	14.2(02.6)
20	104.6(12.6)	48.1(06.3)	3.8(0.6)	30	102.2(14.2)	25.3(06.4)
23	124.5(14.9)	62.5(08.1)	6.6(01.0)	32.5	102.8(15.6)	24.3(07.6)
25	144.5(17.3)	75.0(09.8)	7.8(01.2)	35	110.9(16.6)	26.1(08.5)
28	144.7(17.4)	84.0(010.9)	9.3(1.4)	37.5	125.2(17.7)	34.1(09.3)
30	143.8(17.3)	82.6(10.7)	9.2(1.4)	40	125.3(19.2)	34.0(10.1)
33	149.0(17.9)	79.6(10.3)	8.4(1.3)	42.5	131.8(18.6)	18.8(10.2)
35	150.7(18.1)	80.5(10.5)	9.5(1.4)	45	120.7(15.1)	29.7(11.9)
38	149.3(17.9)	85.5(11.1)	10.1(1.5)			
40	153.6(18.4)	87.8(011.4)	10.5(1.6)			

Table B.4: Production Cross section of Bismuth and Uranium

Bibliography

[1] C. J. Powell, *Rev. Mod. Phys.* **1976**, *48*, 33–47.

[2] X. Llovet et al., *J. Phys. Chem. Ref. Data* **2014**, *43*, 013102.

[3] M. Guerra et al., *International J. Mass Spectrom.* **2012**, *313*, 1 –7.

[4] D. Bote et al., *At. Data Nucl. Data Tables* **2009**, *95*, 871 –909.

[5] `www.srim.org/`.

[6] W. Williamson et al., *J. Appl. Phys.* **1987**, *61*, 4880–4884.

[7] `http://henke.lbl.gov/optical_constants/filter2.html`.

[8] S. Agostinelli et al., *Nucl. Instrum. Methods Phys. Res. Sect. A* **2003**, *506*, 250 –303.

[9] J. Baro et al., *Nucl. Instrum. Methods Phys. Res. Sect. B* **1995**, *100*, 31 –46.

[10] S. Perkins et al., Tables and graphs of electron-interaction cross sections from 10 eV to 100 GeV derived from the LLNL Evaluated Electron Data Library (EEDL), Z= 1–100, tech. rep., Lawrence Livermore National Lab., CA (United States), **1991**.

[11] A. Bielajew et al., *Monte Carlo Transport of electrons and photons*, Plenum Press, New York, **1988**.

[12] C. Møller, *Ann. Phys.* **1932**, *406*, 531–585.

[13] F Salvat et al. in Workshop Proceedings Issy-les-Moulineaux, France, AEN-NEA, **2001**.

[14] R Mayol et al., *J. Phys. B: At. Mol. Opt. Phys.* **1990**, *23*, 2117.

[15] J. M. Fernández-Varea et al., PENELOPE 2011: a code system for Monte Carlo electron and photon transport, NEA Data Bank, NEA/NSC/DOC(2011)5.

[16] D. Bote et al., *Phys. Rev. A* **2008**, *77*, 042701.

[17] Y Wu et al., *J. Phys. B: At. Mol. Opt. Phys.* **2004**, *37*, 4527.

[18] Y Wu et al., *J. Phys. B: At. Mol. Opt. Phys.* **2007**, *40*, 735.

[19] A Moy et al., *J. Phys. B: At. Mol. Opt. Phys.* **2013**, *46*, 115202.

[20] H. Rahangdale et al., *J. Quant. Spectrosc. Radiat. Transfer* **2016**, *174*, 79 –87.

[21] H. V. Rahangdale et al., *Phys. Rev. A* **2014**, *89*, 052708.

[22] M. R. Ay et al., *Med. Phys.* **2005**, *32*, 1660–1675.

[23] T. R. Kallman et al., *Rev. Mod. Phys.* **2007**, *79*, 79–133.

[24] A Lahmam-Bennani, *J. Phys. B: At. Mol. Opt. Phys.* **1991**, *24*, 2401.

[25] A Chaudhry et al., *Analysis of Excitation and Ionization of Atoms and Molecules by Electron Impact*, Academic Press, **2011**.

[26] P Nagy et al., *Journal of Physics B: Atomic and Mol. Phys.* **1980**, *13*, 1249.

[27] L. J. Kieffer et al., *Rev. Mod. Phys.* **1966**, *38*, 1–35.

[28] H. Ehrhardt et al. in *Case Studies in Atomic Collision Physics*, (Ed.: E. M. McDowell), Elsevier, **1972**, pp. 159 –208.

[29] E. J. McGuire, *Phys. Rev. A* **1974**, *9*, 1840.

[30] W. Bambynek et al., *Rev. Mod. Phys.* **1972**, *44*, 716–813.

[31] D. L. Webster et al., *Phys. Rev.* **1933**, *43*, 839–858.

[32] J. C. Clark, *Phys. Rev.* **1935**, *48*, 30–42.

[33] A. E. Smick et al., *Phys. Rev.* **1945**, *67*, 153–161.

[34] M Green, *Proceedings of the Physical Society* **1964**, *83*, 435.

[35] M Green et al., *J. Phys. D: Appl. Phys.* **1968**, *1*, 425.

[36] D. C. Joy, *Scanning* **1995**, *17*, 270–275.

[37] M. Sarkar, *Pramana* **2011**, *76*, 293–312.

[38] J. L. Campbell, *Nuclear Inst. and Methods in Physics Research B* **1988**, *31*, 518–524.

[39] A. Kumar et al., *Phys. Rev. A - At. Mol. and Opt. Phys.* **2010**, *81*, 1–10.

[40] A. Kumar et al., *Pramana* **2007**, *68*, 983–994.

[41] S. F. Barros et al., *J. Phys. B: At. Mol. Opt. Phys.* **2015**, *48*, 175201.

[42] a. Moy et al., *Chem. Phys.* **2014**, *440*, 18–24.

[43] W. Mehlhorn, *Phys. Lett. A* **1968**, *26*, 166 –167.

[44] J. Campbell et al., *Nucl. Instrum. Methods* **1974**, *117*, 519 –532.

[45] F. Scholze et al., *X-Ray Spectrom.* **2001**, *30*, 69–76.

[46] D. Weathers et al., *Nucl. Instrum. Methods Phys. Res. Sect. B* **1991**, *56*, 964 –967.

[47] J. Zhu et al., *Phys. Rev. A* **2009**, *79*, 052710.

[48] Z. An et al., *Nucl. Instrum. Methods Phys. Res. Sect. B* **2006**, *246*, 281 –287.

[49] P. Xiu-Feng et al., *Chin. Phys. Lett.* **2001**, *18*, 39.

[50] L. Zhengming et al., *Phys. Rev. A* **2001**, *63*, 034702.

[51] C. Tang et al., *J. Appl. Phys.* **2002**, *91*.

[52] L. Zheng-Ming et al., *Chin. Phys. Lett.* **2002**, *19*, 1610.

[53] S. P. Limandri et al., *Phys. Rev. A* **2012**, *86*, 042701.

[54] Z. Luo et al., *J. Phys. B: At. Mol. Opt. Phys.* **1996**, *29*, 4001.

[55] W. R. Nelson et al., The EGS4 code system, tech. rep. Report SLAC-265, Stanford Linear Accelerator Center, Menlo Park, CA (USA), **1985**.

[56] D. H. H. Hoffmann et al., *Zeitschrift für Physik A* **1979**, *293*, 187–201.

[57] R. Hippler et al., *Phys. Rev. A* **1981**, *23*, 1730–1736.

[58] R. K. Singh et al., *J. Phys. B: At. Mol. Opt. Phys.* **2003**, *36*, 3031.

[59] C. S. Campos et al., *Phys. Rev. A* **2002**, *66*, 012719.

[60] L. Kissel et al., *At. Data Nucl. Data Tables* **1983**, *28*, 381 –460.

[61] G. Glupe et al., *Phys. Lett. A* **1967**, *25*, 274 –275.

[62] J. J. Vrakking et al., *Phys. Rev. A* **1974**, *9*, 1932–1937.

[63] D. M. Smith et al., *J. Phys. D: Appl. Phys.* **1974**, *7*, 151.

[64] T. E. Gallon, *J. Phys. D: Appl. Phys.* **1972**, *5*, 822.

[65] W Hink et al., *J. Phys. E: Sci. Instrum.* **1980**, *13*, 882.

[66] L. M. Middleman et al., *Phys. Rev. A* **1970**, *2*, 1429.

[67] B. Schlenk et al., *Acta Phys. Hung.* **1976**, *41*, 159–163.

[68] J. Pàlinkàs et al., *Z. Angew. Phys. A Atoms and Nuclei* **1980**, *297*, 29–33.

[69] K. Shima et al., *Phys. Rev. A* **1981**, *24*, 72–78.

[70] Y. K. Park et al., *Phys. Rev. A* **1975**, *12*, 1358–1364.

[71] S. Ricz et al., *Acta Phys. Hung.* **1977**, *42*, 269–271.

[72] Y. Wu et al., *Nucl. Instrum. Methods Phys. Res. Sect. B* **2010**, *268*, 2473 –2476.

[73] S. Salem et al., *Phys. Lett. A* **1971**, *37*, 161 –162.

[74] D. Davis et al., *Phys. Lett. A* **1972**, *38*, 169 –170.

[75] H. Schneider et al., *Phys. Rev. Lett.* **1993**, *71*, 2707–2709.

[76] H. Genz et al., *Zeit. für Phys. A* **1982**, *305*, 9–19.

[77] K. Ishii et al., *Phys. Rev. A* **1977**, *15*, 906.

[78] D. H. H. Hoffmann et al., *Zeit. für Phys. A* **1979**, *293*, 187.

[79] J. J. Thomson, *Philos. Mag. Series* **1912**, *23*, 449–457.

[80] H. Bethe, *Ann. Phys.* **1930**, *397*, 325–400.

[81] A Burgess et al. in *Advances in Atomic and Mol. Phys. Vol. 4*, (Eds.: D. R. Bates et al.), Academic, New York, **1968**, p. 109.

[82] L. Vriens in, *Vol. 1*, (Eds.: E. W. M. McDowell et al.), North-Holland,Amsterdam, **1969**, p. 335.

[83] R. H. G. Reid in *Photon and Electron Collisions with Atoms and Molecules*, (Eds.: P. G. Burke et al.), Plenum Press, New York, **1997**, p. 37.

[84] S. Segui et al., *Phys. Rev. A* **2003**, *67*, 062710.

[85] C. J. Joachain, *Quantum collision Theory*, North-Holland Publishing, Amsterdam, **1983**.

[86] J Griffiths, D, *Introduction to Quantum Mechanics*, 4th ed., Dorling Kindersley, New Delhi, **2008**.

[87] *Quantum Mechanics*, 2nd ed., PEARSON Education, **2000**.

[88] R. Hippler, *Phys. Lett. A* **1990**, *144*, 81–85.

[89] D. H. Madison et al. in *Atomic Inner-Shell Ionization and Transition Probabilities*, *Vol. 1*, (Ed.: B Crasemann), Academic, New York, **1975**, pp. 1–70.

[90] H. L. Zhang et al., *Phys. Rev. A* **1989**, *40*, 616–632.

[91] D. H. Sampson, *Phys. Rev. A* **1986**, *34*, 986.

[92] J. Colgan et al., *Phys. Rev. A* **2006**, *73*, 062711.

[93] I Bray et al., *Phys. Rev. Lett.* **1996**, *76*, 2674.

[94] I. Bray et al. in *Adv. At., Mol., Opt. Phys. Vol. Volume 35*, doi: DOI: 10.1016/S1049-250X(08)60164-0, Academic Press, **1995**, pp. 209–254.

[95] M. S. Pindzola et al., *Phys. Rev. A* **2009**, *80*, 052706.

[96] Y Itikawa, *Phys. Rep.* **1986**, *148*, 69.

[97] I. P. Grant, *Relativistic Quantum Theory of Atoms and Molecules*, Springer, **2006**.

[98] M. E. Rose, *Relativistic Electron Theory*, Wiley, New York, **1961**.

[99] R Latter, *Phys. Rev.* **1955**, *99*, 510–519.

[100] D Liberman et al., *Comput. Phys. Commun.* **1971**, *2*, 107–113.

[101] A. R. Edmonds, *Angular Monentum in Quantum Mechanics*, Princeton University Press, Princeton, NJ, **1957**.

[102] J. M. Fernández-Varea et al., *Phys. Rev. A* **2011**, *83*, 022702.

[103] N. F. Mott, *Proc. R. Soc. London Ser. A* **1930**, *126*, 259–267.

[104] M Gryzinski, *Phys. Rev.* **1965**, *138*, A305–A321.

[105] M Gryzinski, *Phys. Rev.* **1965**, *138*, A322–A335.

[106] M Gryzinski, *Phys. Rev.* **1965**, *138*, A336–A358.

[107] M Gryzinski, *Phys. Rev.* **1959**, *115*, 374.

[108] Y. K. Kim et al., *Phys. Rev. A* **1994**, *50*, 3954–3967.

[109] J. C. Fuggle et al., *J. Electron Spectrosc. Relat. Phenom.* **1980**, *21*, 275.

[110] J. P. Desclaux, *Comput. Phys. Commun.* **1975**, *9*, 31–45.

[111] P. Indelicato et al., *Phys. Rev. A* **1990**, *42*, 5139.

[112] Y.-K. Kim et al., *Phys. Rev. A* **2000**, *62*, 052710.

[113] Y. K. Kim et al., *J. Res. Natl. Inst. Stand. Technol.* **2000**, *105*, 285–291.

[114] Y.-K. Kim et al., *Phys. Rev. A* **2001**, *64*, 052707.

[115] Y.-K. Kim et al., *Phys. Rev. A* **2002**, *66*, 012708.

[116] P. J. Santos et al., *Eur. Phys. J. D* **2008**, *47*, 339–350.

[117] Y.-K. Kim, *Phys. Rev. A* **2001**, *64*, 032713.

[118] E. Casnati et al., *J. Phys. B* **1982**, *15*, 155.

[119] R. D. Deslattes et al., *Rev. Mod. Phys.* **2003**, *75*, 35–99.

[120] M. Guerra et al., *International J. Mass Spectrom.* **2013**, *348*, 1 –8.

[121] C. Kuyatt et al. in *Atomic and Electron PhysicsAtomic Interactions*, (Eds.: B. Bederson et al.), Methods in Experimental Physics, Academic Press, **1968**, pp. 1 –115.

[122] M. Basunia, *Nucl. Data Sheets* **2006**, *107*, 3323.

[123] E. Browne, *Nucl. Data Sheets* **2003**, *98*, 665 –800.

[124] B. Singh et al., *Nucl. Data Sheets* **2008**, *109*, 2439 –2499.

[125] http://physics.nist.gov/PhysRefData/FFast/html/form.html.

[126] E. G. Berezhko et al., *Journal of Physics B: Atomic and Mol. Phys.* **1977**, *10*, 2467–2477.

[127] M. Lépy et al., *Appl. Radiat. Isot.* **2008**, *66*, Proceedings of the 16th International Conference on Radionuclide Metrology and its Applications, 715 –721.

[128] `www.nist.gov/pml/data/xcom/index.cfm`.

[129] J. Campbell, *At. Data Nucl. Data Tables* **2003**, *85*, 291 –315.

[130] J. Campbell et al., *At. Data Nucl. Data Tables* **1989**, *43*, 281 –291.

[131] W Jitschin et al., *Journal of Physics B: Atomic and Mol. Phys.* **1983**, *16*, 1417.

[132] D. D. Cohen, *Journal of Physics B: Atomic and Mol. Phys.* **1984**, *17*, 3913.

[133] Y. P. Singh et al., *Phys. Rev. A* **2000**, *63*, 012713.

[134] G. Lapicki et al., *Phys. Rev. A* **2005**, *72*, 022729.

[135] S. Datz et al., *Phys. Rev. A* **1974**, *9*, 192–196.

[136] J. H. Scofield, *At. Data Nucl. Data Tables* **1974**, *14*, 121 –137.

[137] J. H. Scofield, *Phys. Rev. A* **1974**, *10*, 1507–1510.

[138] J. H. Scofield, *Phys. Rev. A* **1975**, *12*, 345–345.

[139] M. H. Chen et al., *Phys. Rev. A* **1981**, *24*, 177–182.

[140] J. Miranda et al., *Nucl. Instrum. Methods Phys. Res. Section B: Beam Interactions with Materials and Atoms* **2002**, *189*, 21–26.

[141] M. O. Krause, *J. Phys. Chem. Ref. Data* **1979**, *8*, 307–327.

[142] `http://geant4.web.cern.ch/geant4/support/source_archive.shtml`.

[143] `https://geant4.web.cern.ch/geant4/`.

[144] E Cullen, D et al., EPDL97: the Evaluated Photon Data Library, в Г Є97 version, UCRL-50400,Vol.6, Rev.5, tech. rep., Lawrence Livermore National Lab., CA (United States).

[145] S. Perkins et al., Tables and graphs of electron-interaction cross sections from 10 eV to 100 GeV derived from the LLNL Evaluated Electron Data Library (EEDL), Z= 1–100, UCRL-50400,Vol. 31, tech. rep., Lawrence Livermore National Lab., CA (United States), **1991**.

[146] S. T. Perkins et al., Tables and Graphs of Atomic Subshell and Relaxation Data De- rived from the LLNL Evaluated Atomic Data Library (EADL), Z=1-100, UCRL-50400, Vol-30, tech. rep., Lawrence Livermore National Lab., CA (United States).

[147] J. D. Jackson, *Classical Electrodynamics*, 2nd ed., Wiley Press, **1975**.

[148] S. M. Seltzer et al., *Nucl. Instrum. Methods Phys. Res. Sect. B* **1985**, *12*, 95 –134.

[149] S. M. Seltzer et al., *At. Data Nucl. Data Tables* **1986**, *35*, 345 –418.

[150] E Haug, *Zeitschrift für Naturforschung A* **1975**, *30*, 1099–1113.

[151] R. Pratt et al., *At. Data Nucl. Data Tables* **1977**, *20*, 175 –209.

[152] `http://geant4.web.cern.ch/geant4/UserDocumentation/UsersGuides/ForToolkitDeveloper/BackupVersions/V9.6/fo/BookForToolDev.pdf`.

[153] G. Wentzel, *Zeitschrift für Physik* **1927**, *40*, 590–593.

[154] H. A. Bethe, *Phys. Rev.* **1953**, *89*, 1256–1266.

[155] M. S. Pindzola, *Phys. Rev. A* **2014**, *90*, 13–17.

[156] M. S. Pindzola, *J. Phys. B: At. Mol. Opt. Phys.* **2015**, *48*, 015201.